Development of *In Vitro* Microfluidic Models for Studying Inflammation and Stem Cell Biology

By

Patrick H. McMinn

A dissertation submitted in partial fulfillment of the requirements for the degree of

DOCTOR OF PHILOSOPHY

(BIOMEDICAL ENGINEERING)

at the

UNIVERSITY OF WISCONSIN – MADISON

2020

Date of final oral examination: 5/29/2020

The dissertation is approved by the following members of the Final Oral Committee:

David J. Beebe, Professor, Pathology and Laboratory Medicine

Anna Huttenlocher, Professor, Pediatrics

Miriam Shelef, Assistant Professor, Medicine

Suzanne Ponik, Senior Scientist, Cell and Regenerative Biology

Jacques Galipeau, Professor, Medicine

Acknowledgements

I want to start off by expressing how extremely fortunate I feel to have had the opportunity to be a member of Dr. David Beebe's laboratory, and have him as my advisor. Dave, your guidance and advice throughout my graduate school career has made me the scientist and engineer I am today. You've put together an amazing team of researchers and given them the tools and leadership to do impactful work, and I consider myself extremely lucky to have been a part of that. I am extremely thankful for the freedom you gave me to explore and create throughout graduate school, I discovered I have a passion for engineering and for that I can't thank you enough.

I would also like to thank my committee, Dr. Anna Huttenlocher, Dr. Suzanne Ponik, Dr. Miriam Shelef, and Dr. Jacques Galipeau for your recommendations, discussions and your time. The advice and suggestions given to me, especially during my preliminary exam, significantly helped me focus my research for the better. Anna, thank you for your guidance on the neutrophil project and for putting together such an awesome team of researchers. I have greatly enjoyed collaborating with your team. Suzanne, while my work on breast cancer extravasation was short, I want to thank you for the time and advice you gave me on it.

I want to thank Dr. Sheena Kerr, Dr. Jose Maria Ayuso Dominguez, and Dr. Patrick Ingram for the scientific and life-related conversations; I consider you my mentors and friends. I am especially thankful to Sheena; I have learned so much from you these past few years, both scientifically and culturally, and I am a better person for having worked with you. Thank you to everyone in the MMB Lab, both present and past, that has made graduate school amazing and fulfilling. Thanks

to Pete, and Alice, this lab would not run without you, Karina, Maria, Jake, Molly, Brian, Tony, Bridgette, Chao, Mouhita, Jay, Loren, Ross, Yasmin, Teddy, John, Hannah, KYP, Megan, Duane, Terry, Layla, Mary. To my undergraduate research assistants, Matt, Jack, Thor, and Luke, thank you for all your help. I would also like to thank my collaborators Dr. Laurel Hind, It has been fun working with you and talking neutrophils, Morgan, thanks for all of the blood draws, Ashley, Lucas, and Dave.

A huge thank you to my family. My parents, Bonnie and Russ McMinn, have always supported in any way they can and I would not be here, the person that I am today, without them. I have always looked up to my brother, Russ, and he has always been there for me when I needed help. Rachel, Jack, and Ellie, thank you for making Madison such a great place to live. I can't put in to words how much I love my family and how thankful for them I am.

Finally, I would like to give a huge thank you to my wife, Mary Ellen, for her support, understanding, and confidence in me. Your support has helped me scientifically and emotionally throughout my entire Ph.D. journey.

Abstract

Chronic inflammatory diseases are the leading cause of death in the world. One of the critical steps of inflammation is the recruitment and activation of neutrophils. This process results in a highly focused mobilization of neutrophils at the site of infection or injury. Dysregulation of this process can lead to disproportionate levels of inflammation resulting in tissue damage, chronic inflammation, or the spread of infection. By improving our understanding of neutrophil trafficking, we can hope to develop better therapeutics and drugs for treating chronic inflammatory diseases. Our current understanding of neutrophil trafficking is predominately derived from animal models, such as mouse, and zebrafish, and simple *in vitro* models such as transwells and 2D devices. These approaches each possess inherent limitations on the types of experiments we can conduct and in correlating the significance of these results to our understanding of human biology. As the development and increased use of microscale organotypic models in research continue, our ability to model neutrophil trafficking using human cells in biologically relevant models could improve our understanding of these events. The goal of this Ph.D. thesis is to investigate the development of microscale organotypic models of three understudied processes related to neutrophil recruitment; neutrophil priming, neutrophil reverse migration, and neutrophil-lymphatic trafficking. We also present the development and characterization of a microscale technology for culturing and differentiating human induced pluripotent stem cells (iPSCs). The following thesis is divided into five chapters and an appendix, each part can be independently read, but all of them should be considered within the overarching goal.

Chapter 1 provides an introduction to neutrophils' role in inflammation, neutrophil-endothelial-macrophage interactions, microscale stem cell culture, and the benefits of microscale organotypic models. In Chapter 2, the development and characterization of a device for studying neutrophil priming and TEM are introduced, and an initial investigation into these topics is conducted. At the end of Chapter 2, preliminary work on modeling neutrophil reverse migration (RM) is presented and shows how neutrophil-macrophage interactions can induce a RM phenotype in neutrophils. In Chapter 3, an organotypic tissue model, consisting of blood and lymphatic endothelial lumens is used to identify secreted components involved in regulating neutrophil-lymphatic trafficking. In Chapter 4, a microscale technology for culturing and differentiating iPSCs is described, characterized, and shown to differentiate iPSCs into neuroepithelial cells, definitive endodermal cells, and cardiomyocytes. Finally, the main conclusions of this Ph.D. thesis and future directions are described in chapter 5.

Table of Contents

List of Figures

Abbreviations

2D	Two-dimensional
3D	Three-dimensional
HUVEC	Human umbilical vein endothelial cell
HLEC	Human lymphatic endothelial cell
DAMP	Damage-associated molecular pattern
PAMP	Pathogen-associated molecular pattern
LPS	Lipopolysaccharides
fMLP	N-formyl-met-leu-phe
TEM	Transendothelial migration
rTEM	Reverse transendothelial migration
RM	Reverse migration
TLM	Trans-lymphatic migration
BMEC	Breast microvascular endothelial cell
BTEC	Breast tumor-associated endothelial cell
KOALA	Kit-On-A-Lid-Assay
LENS	LumeNext-Stacks
iPSC	Induced-pluripotent stem cell
HTL	High-throughput lumen
ECM	Extracellular matrix

Chapter 1:

Introduction

1.1 Inflammation and Disease

Inflammation is a set of complex biological processes that form a critical response to potential danger signals including tissue damage and pathogens. Inflammation is a protective response whose purpose is to eliminate pathogens or damaged tissue, and then facilitate tissue repair. This process involves immune cells, endothelial cells, and a host of secreted factors. Inflammation can be categorized as either acute or chronic depending on its duration, the types of cells involved, and types of secreted factors [1]. Acute inflammation is the immediate response to injury, stress, or infection which occurs within minutes or hours after insult. It involves the systemic and local coordinated mobilization of various cellular and humoral components to enact a focused response. In a healthy acute inflammatory response, pathogens and damaged tissue are removed and the repair mechanisms are initiated [2]. If there is dysregulation of the immune response or the infection or injury persists, chronic inflammation can follow. Chronic inflammation can last anywhere from a few days to even years and while it involves many of the same immune components seen in an acute inflammatory response, it is characteristically different than acute inflammation. Chronic inflammation is a common outcome of infectious disease, and studies continue to find links between non-infectious diseases such as cancer, and even depression with inflammation [3][4]. *It has been hypothesized that all disease is a result of inflammation* [5]. *Regardless of the validity of this theory, inflammation plays a major role in*

disease progression and morbidity and could offer new targets for improved therapeutics and drugs for treating a wide variety of diseases.

According to the World Health Organization (WHO), chronic inflammatory diseases, including cardiovascular disease, diabetes, respiratory diseases, autoimmune diseases, infectious disease, and cancer, are the most significant cause of death in the world accounting for around 75% of all deaths worldwide [6][7]. While it is hard to estimate the economic burden of chronic inflammation, people living with chronic inflammatory diseases spend significantly more on healthcare than those who don't. For example, people in the U.S. living with rheumatoid arthritis spent an average of $1,193 extra out of pocket on treatment for their condition [8][9]. *By better understanding the underlying disease biology and how inflammation contributes to it, we can expect to identify and discover new and innovative medicines.*

1.2 Innate Immunity

The immune system can be separated into two different, but interconnected types of immunity: adaptive, and innate immunity [10]. The adaptive immune system is a type of immune strategy that is highly specific, exhibits immunological memory, but requires significant lead time to take action. On the contrary, innate immunity is non-specific, possesses no immunological memory, and can act much more rapidly. Because of the high specificity and timeframe with which the adaptive immune system acts, it is less involved during acute inflammation than the innate immune system.

The innate immune system uses several different strategies to deal with infection or injury [11]. The first mechanism is the constitutively active immune components. These consist of physical barriers that prevent pathogens from entering the body; skin, mucus, sweat, defensins, gastric acid, and lysozymes for example. Besides physical and chemical barriers, the innate immune system also uses a set of biological barriers to prevent pathogen from accessing the body. These include humoral components such as complement, and the clotting system which either kill or opsonize the pathogen/foreign particle, or isolate it in place. The last strategy the innate immune system employs is the activation and recruitment of white blood cells, or leukocytes, to sites of infection or injury [12]. The list of leukocytes of the innate immune system include mast cells, eosinophils, basophils, natural killer cells, macrophages, dendritic cells, and neutrophils. *The most numerous leukocyte in the body by far, however, is the neutrophil; comprising as much as 80% of all circulating leukocytes* [13].

1.3 Neutrophils

Neutrophils are a type of leukocyte, that circulate throughout the body and act as first responders to infection and cell damage. They are characterized by their polymorphonuclear shape and high number of granules in their cytoplasm. While neutrophils have been classically thought to be a homogenous population of short lived, transcriptionally inactive cells, recent work suggests the opposite [14]. Experiments in mice and humans, involving fluorescent activated cell sorting (FACS) to isolate and sort primary neutrophils, have shown the presence of distinct neutrophil populations with fluctuating levels of cell surface receptors as well as different functional phenotypes in circulation. Continued research into this phenomenon has associated some of

these neutrophil subsets like CD11b^{+} CD15^{hi} CD66b^{+} MPO^{hi} Arg1^{+} CD16^{int} IL-5Ra^{-} neutrophils, or low density granulocytes which damage endothelial cells in conditions such as cancer, and lupus respectively [15][16][17][18]. In terms of lifespan, *in vivo* labeling experiments of human neutrophils have found that under homeostatic conditions, the average neutrophil will live for 5.4 days, much longer than the <7 hour lifespan previous reports found [19][20]. Further studies into this effect have directly linked endothelial secreted IL-6 in extended neutrophil longevity [21]. Lastly, RNA sequencing of human neutrophil mRNA found that they are quite transcriptionally active and have distinct mRNA expression patterns after activation and priming [22][23]. *Clearly, neutrophils are more biologically complex than what was originally assumed and warrant more rigorous and in-depth studies.*

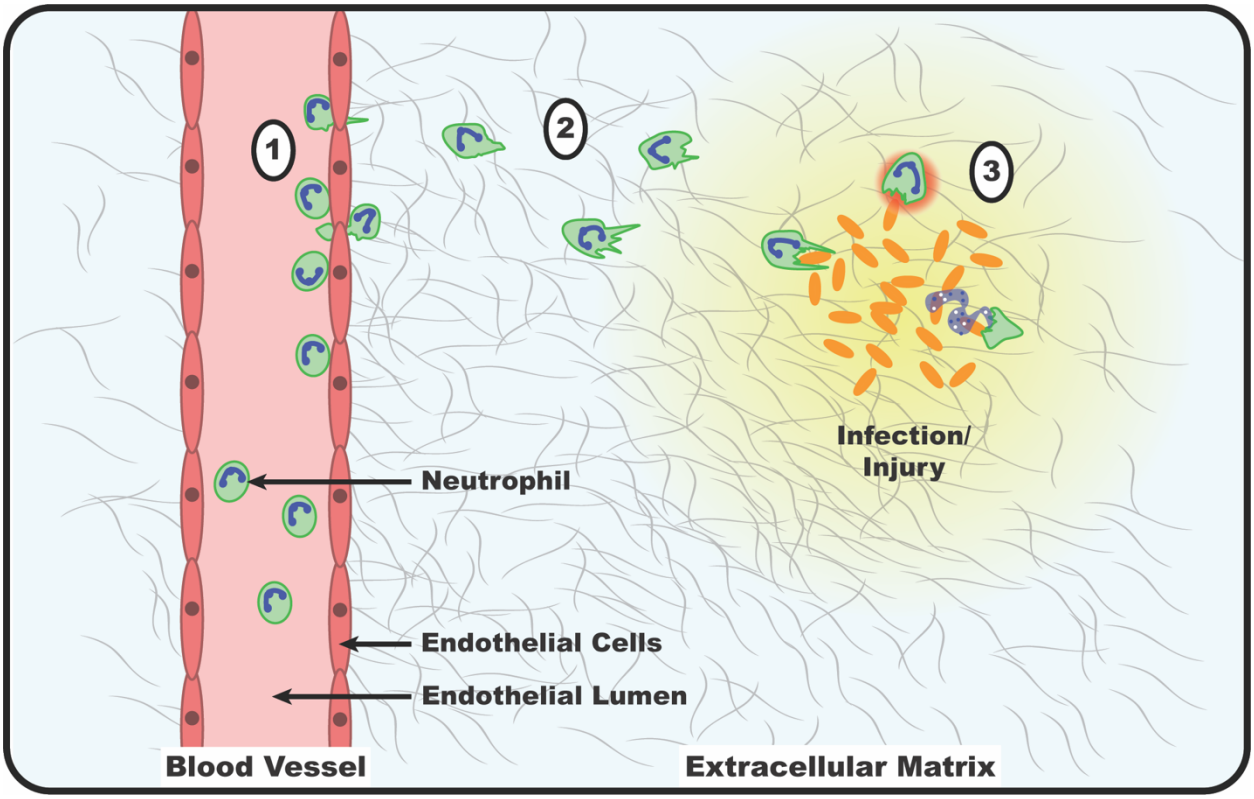

Figure 1.1: Neutrophil Trafficking Diagram. 1) Circulating neutrophils encounter inflammatory signals which cause them to interact with and arrest on the wall of the blood vessel, adhere to endothelial cells, and undergo TEM. 2) Neutrophils migrate down gradients of chemokines in a process called chemotaxis. 3) Once at the site of infection/injury, neutrophils phagocytose pathogens or cell debris, release toxic granules, produce ROS, or undergo NETosis.

1.4 Neutrophil Trafficking

Trafficking of neutrophils to sites of infection and injury is essential for optimal functioning of the immune system. This trafficking from the circulatory system to interstitial spaces involves a multistep process beginning with cytokine-mediated signaling events, hemodynamic shear forces, adhesion, transendothelial migration, and chemotaxis. Once at the site of infection or injury, neutrophils can fulfill their effector functions (Figure 1.1).

1.4.1 Neutrophil-Endothelial Interactions

Endothelial vessels help traffic neutrophils to sites of inflammation and facilitate their activation and entry into the interstitium [24]. This neutrophil extravasation cascade is a multi-step process that begins with the blood vessel endothelium sensing signals from damaged tissue, or pathogen-derived products [25]. These signals include the acute phase proteins, IL-1α, IL-6, and TNFα, PAMPs such as fMLP and LPS, DAMPs, and other signals derived from tissue resident immune cells which act to increase vessel permeability, increase luminal surface presentation of selectins and integrins, and present chemokines from the basal side to the apical side [26][27]. Circulating neutrophils sense these changes and begin to roll along the surface of the endothelium. This

interaction is mediated by selectins and is weak and transient. Subsequent stimulation of neutrophils by chemokines that are presented by the endothelium, triggers the activation of neutrophil integrins, which allow the neutrophils to firmly adhere on the endothelial surface. Once strongly adhered, neutrophils crawl along the endothelium until they find a permissive site to enter the interstitial space. Neutrophils pass across the endothelium in a process termed transendothelial migration (TEM) which can either occur by passing through a gap in the now-leaky vessel, pericellular TEM, or by passing straight through endothelial cells, transcellular TEM. Lastly, the neutrophils must also cross the pericyte layer and breach the basal membrane before reaching the site of infection or injury.

This neutrophil-endothelial interaction serves to not only aid neutrophil entry into the interstitium, but also induces phenotypic changes that cause the neutrophil to enter an enhanced state of responsiveness and increased lifespan, termed priming [28]. Priming is known to occur after exposure to pro-inflammatory cytokines, pathogen-based products, and adhesion, and this process alters a neutrophils ability to phagocytose, release granules, form NETs, generate ROS, and significantly increases their lifespan [21]. Neutrophil TEM, and priming have been extensively studied in 2D cell culture and animal models such as zebrafish and mice [29][30]. *While these studies have provided valuable insights into neutrophil biology, it remains unclear to what extent these findings translate to human biology* [31].

Until recently, neutrophils were thought to only interact with blood vessel endothelial cells and refrain from entering the lymphatics. However, with the improvement of intravital imaging

techniques and availability of transgenic organisms, researchers have been able to demonstrate that neutrophils will traffic from peripheral tissue, through lymphatic vasculature, to peripheral lymph nodes during infection with microorganisms such as *Staphylococcus aureus*, *Pseudomonas aeruginosa*, *Listeria monocytogenes*, *Yersinia pestis*, *Toxoplasma gondii*, and *Leishmania major* [32][33]. Furthermore, these studies have also shown that neutrophils interact with resident lymphocytes inside the lymph node via antigen presentation [34]. *While researchers have identified CCL21/CCL19, TNFα, and various cell surface receptors including CD45, and CD11b as being involved in neutrophil-lymphatic trafficking, our understanding of this process is incomplete.* This is in part due to a lack of *in vitro* models for studying this process.

1.4.2 Neutrophil Chemotaxis

Neutrophils are highly motile cells that are able to reach sites of injury or infection in a matter of minutes to hours. After neutrophil TEM, neutrophils chemotax down a hierarchy of gradients until they reach the source of chemokines. Neutrophil chemokines generally fall into one of three types, damage-associated molecular patterns (DAMPs), pathogen-associated molecular patterns (PAMPs), or host-derived cytokines. DAMPs are released when cells or tissue are disrupted and usually consist of intracellular particles such as ATP or DNA [35]. PAMPs are released or secreted by pathogens and consist of shed "coating" material like lipopolysaccharide (LPS), or metabolic byproducts like N-Formylmethionyl-leucyl-phenylalanine (fMLP) [36][37]. The last category of neutrophil chemokines, the host-derived cytokines, are complex and poorly understood [38][39][40][41]. While non-immune stromal cells can release inflammatory cytokines, the cells most responsible for coordinating neutrophil chemotaxis are tissue resident macrophages

[42][43]. During infection, macrophages recruit neutrophils by secreting a multitude of cytokines including CXCL8 (IL-8), CXCL1/2/3 (GRO-α/β), CCL2 (MCP-1), and CCL3/4 (MIP-1α/β) [44]. While these cytokines are potent neutrophil chemokines, their efficacy in recruiting neutrophils *in vivo* is highly dependent on the inflammatory context with which they are secreted. *How the inflammation microenvironment and neutrophil activation status impacts chemotaxis in humans is poorly understood.*

1.4.3 Neutrophil Function

The main function of neutrophils is to act quickly to infection and injury, and overwhelm pathogens with numbers and an arsenal of biochemical and physical mechanisms including phagocytosis, release of toxic granules, production of reactive oxygen species (ROS), and the formation of neutrophil extracellular traps (NETs). These mechanisms are non-specific and toxic to both pathogens and host tissue. Dysregulation of neutrophil activation can induce an overactive state in neutrophils which can cause unnecessary tissue damage. On the contrary, failure to activate neutrophils can lead to poor wound healing or the spread of infection. *Using neutrophil effector functions as readouts for their activation status and the condition of the inflammatory microenvironment is a useful tool for studying neutrophils.*

1.5 Inflammation Resolution and Neutrophils

To prevent further tissue damage, at the conclusion of inflammation neutrophils will undergo apoptosis, programmed cell death, and subsequent efferocytosis by resident macrophages. However, *in vitro* and *in vivo* experiments suggest that an alternative pathway exists for

neutrophils, termed neutrophil reverse migration (RM). As the name suggests, neutrophil RM is the process whereby neutrophils migrate away from sites of inflammation and sometimes re-enter the endothelium, called neutrophil reverse transendothelial migration (rTEM). It is speculated to be a significant means of inflammation resolution but has yet to be proven in humans. Using *in vivo* microscopy techniques, neutrophils were observed migrating away from sites of inflammation in zebrafish and mice instead of undergoing apoptosis [45][46]. Furthermore, a population of $CD54^{high}$, $CXCR1^{low}$ cells, identified as reverse-migrated neutrophils in *in vitro* models, was found in circulating in humans [47][48]. Macrophages are well known to be key mediators in determining the outcome of the inflammatory response and were shown, in zebrafish, to be necessary for neutrophil RM. *While there is evidence suggest that both juxtracrine and paracrine signalling between neutrophils and macrophages is what coordinates neutrophil RM, we still do not completely understand the fate of neutrophils during inflammation resolution* [49][50].

1.6 Stem Cell Culture

Cell-based assays are a ubiquitous tool in biotechnology and play a major role in drug development, disease research, and diagnostics [51]. *Current cell-based assays, however, typically require specialized equipment, long assay times, and skilled personnel to perform the tasks associated with cell culture and monitoring* [52]. Moreover, differences that arise because of the aforementioned variables make it difficult to standardize protocols and create a logistical barrier for collaborating laboratories and medical facilities. Furthermore, schools and education professionals are continually adjusting what they teach to meet the everchanging science

landscape. While cell culture is starting to be taught in some college and high school level classrooms, the costs and difficulty of doing so are prohibitive to most [53][54]. In order to make cell-based assays more accessible and to ensure primary and secondary schools are teaching the most relevant and up-to-date material to students, the costs and complexity of performing mammalian cell culture need to be reduced. *One approach researchers have turned to, to accomplish this is by using microfluidics.*

One area of mammalian cell culture where variability has the biggest impact on cell viability and phenotype is with stem cells. Induced Pluripotent Stem Cells (iPSCs) are reprogrammed adult cells that are capable of differentiating into any adult cell type and represent an unprecedented opportunity for improved disease modeling and personalized medicine [55]. Despite the progress in developing iPSC-based assays for drug screening and clinical use, variability and cost continue to hinder further progress [56]. *As the use of iPSCs in research and education continues to increase, these problems will become even more important to solve.*

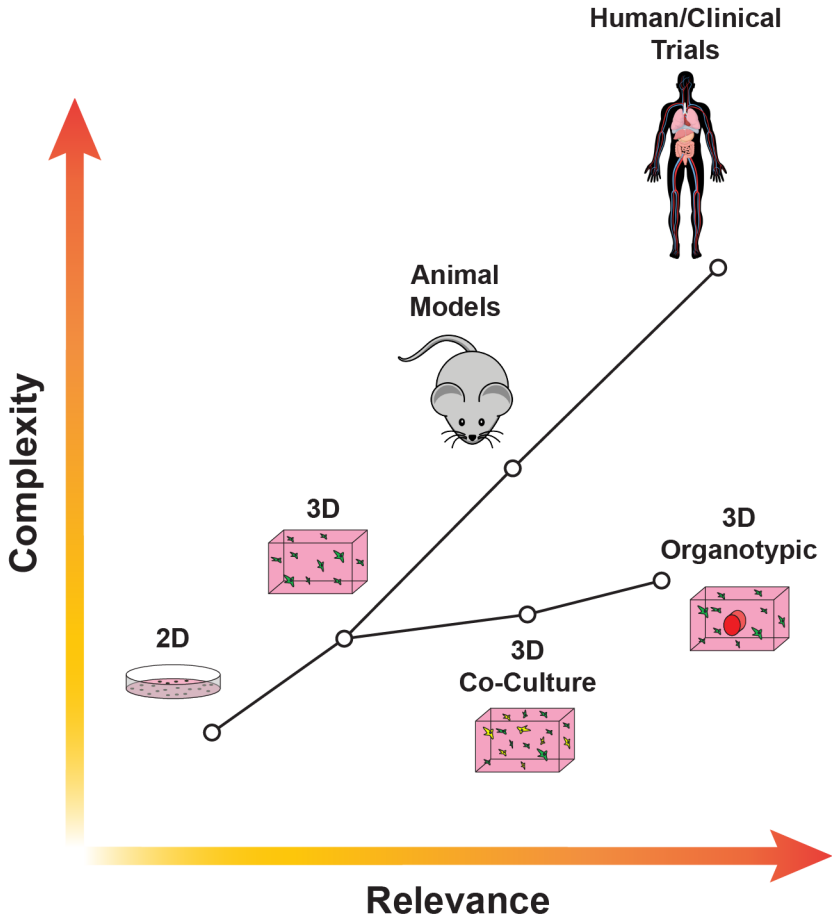

Figure 1.2: Complexity and Relevance of different types of biological research models

1.7 The Microscale and Organotypic Models

Cellular life exists at the microscale which encompasses a complex set of interactions between cellular components, secreted factors, ECM components, and physical factors. Although two-dimensional (2D) models have made significant contributions to biological research, their failure to take into account important microenvironmental parameters have prompted the development of microscale three-dimensional (3D) models. It has been shown that cells cultured in microscale 3D models behave differently to cells in 2D models [57][58][59]. Furthermore, though the use of 3D models are becoming more widely used, researchers continue to improve

upon them, incorporating structure-function relationships, improved cell sources, and overall higher levels of relevance (Figure 1.2). These organotypic models have been shown to alter cellular phenotype and function such as migration, polarization, proliferation, and signaling [60][61][62][63][64]. *Using microscale organotypic models to study biology presents a low cost and highly relevant method for studying human biology in a physiologically relevant way.*

1.8 Summary and Thesis Aims

Inflammation underlies every major human disease and represents a significant target for future therapeutics and drugs. Inflammation is largely coordinated by the innate immune system whose most abundant cellular mediator is the neutrophil. Neutrophils are highly motile and toxic cells whose trafficking throughout the body is tightly regulated. Aspects of neutrophil trafficking that are still not completely include neutrophil-endothelial-macrophage interactions and how they coordinate neutrophil reverse migration, and neutrophil-lymphatic trafficking.

iPSCs are an exciting source of highly relevant cell types that are amenable to genetic manipulations. Their culture and differentiation are highly sensitive and susceptible to inconsistent handling and non-optimal protocols. Microscale/microfluidic technologies could help ameliorate these issue, providing consistent, user-friendly options for researchers and educators.

This thesis is aimed at developing microscale organotypic models of neutrophil trafficking and using them to study neutrophil-endothelial and neutrophil-macrophage interactions during inflammation, and neutrophil-lymphatic trafficking during infections. Part of this thesis work is

also dedicated to developing a microscale iPSC culture and differentiation platform. The specific aims of this thesis were to:

1. **Develop and characterize a microscale organotypic model of neutrophil TEM and infection to facilitate the study of neutrophil-endothelial and neutrophil-macrophage interactions (Chapter 2).**
2. **Investigate the secreted factors responsible for inducing neutrophil-lymphatic trafficking during infection (Chapter 3).**
3. **Engineer a microscale/microfluidic platform for human iPSC culture and differentiation (Chapter 4).**

Chapter 2:

Neutrophil trafficking on-a-chip: an *in vitro* organotypic model for investigating neutrophil priming, extravasation, and migration with spatiotemporal control

This chapter has been adapted from the manuscript published in Lab on a Chip in 2020 "Neutrophil trafficking on-a-chip: an in vitro, organotypic model for investigating neutrophil priming, extravasation, and migration with spatiotemporal control." **Patrick H. McMinn**, Laurel E. Hind, Anna Huttenlocher, and David J. Beebe.

Abstract

Neutrophil trafficking is essential for a strong and productive immune response to infection and injury. During acute inflammation, signals from resident immune cells, fibroblasts, and the endothelium help to prime, attract, and activate circulating neutrophils at sites of inflammation. Due to current limitations with in vitro and animal models, our understanding of these events is incomplete. In this paper, we describe a microfluidic technology and incorporates a lumen-based vascular component with a high degree of spatiotemporal control to facilitate the study of neutrophil trafficking using primary human cells. The improved spatiotemporal control allows functional selection of neutrophils based on their migratory capacity. We use this technology to investigate neutrophil-endothelial interactions and find that these interactions are necessary for robust neutrophil chemotaxis to interleukin-8 (IL-8) and priming of the neutrophils. In agreement with previous studies, we observed that transendothelial migration (TEM) is required for neutrophils to enter a primed phenotypic state. TEM neutrophils not only produce a significantly higher amount of reactive oxygen species (ROS) when treated with PMA, but also upregulate genes involved in ROS production (CYBB, NCF1, NFKB1, NFKBIA), cell adhesion (CEACAM-8,

ITGAM), and chemokine receptors (CXCR2, TNFRSF1A). These results suggest that neutrophil-endothelial interactions are crucial to neutrophil chemotaxis and ROS generation.

2.1 Introduction

Transwells and 2D cell culture plates are the predominant tool used for assessing neutrophil TEM, chemotaxis, and priming *in vitro*. While transwells and culture plates allow for the incorporation of blood-vessel components including endothelial cells, and extracellular matrices (ECM), their spatial configuration, and working volumes lack relevance to *in vivo* biology. Additionally, using these approaches makes it difficult to separate and functionally characterize different populations of neutrophils. There is need for a better *in vitro* system that can provide this spatiotemporal configuration.

Recent advances in 3D *in vitro* microscale models of human neutrophil-vasculature interactions have resulted in models with increased physiological relevance when compared to classical approaches such as 2D microfluidic devices. While 2D models of human neutrophil trafficking have been useful for characterizing responses to chemokines, and measuring NETosis and ROS generation in a heterogeneous population, their usefulness for answering questions involving how co-cultures, or 3D ECM components affect neutrophil biology is limited [48][65]. Current efforts to model blood vessel-leukocyte interactions *in vitro* include strategies such as using self-organized capillaries in a 3D extracellular matrix,[66] 3D bio-printed blood vessels,[67] and micro-molded channels seeded with endothelial cells [68]. While these methods incorporate improved spatial configurations of cells and ECMs, they ultimately lack manipulability which, again, limits their usefulness. Here we add the capability to isolate different neutrophil populations based on their chemotactic capabilities to a 3D organotypic endothelial model and use it to investigate how neutrophil-endothelial interactions affect neutrophil TEM, chemotaxis, and priming. Further

use of this technology could provide future insight into understanding neutrophil heterogeneity, and inflammation resolution [15].

In this paper, we combine two existing microfluidic platforms (LumeNext and Stacks) to create an improved platform for studying neutrophil trafficking. LumeNext is a recently established microfluidic technology by which luminal structures can be created from multiple cell types in a user-defined ECM [69][70]. To create organotypic blood vessels, lumens are mold-casted in a hydrogel that is polymerized within a microfluidic device, and the resulting lumen is seeded with endothelial cells to form an endothelial microvessel. Stacks is a modular, open-microfluidic technology consisting of segmented polystyrene (PS) tube sections which can be filled with different ECM and cellular components, and then stacked on top of one another in the desired configuration [71]. This platform enables the study and isolation of cells in a 3D ECM and is amenable to most molecular biology assays. LENS (LumENext-Stacks) was designed to facilitate the study of neutrophil-endothelial interactions using human primary cells. It is suggested that human neutrophil heterogeneity contributes to their differential priming by the endothelium and inflammatory microenvironment [15][72][73]. Using LENS, we show that neutrophil-endothelial interactions are essential for robust neutrophil TEM/chemotaxis, and priming, in agreement with previous findings [21]. We then isolate neutrophils by their migratory capacity and further quantify their ability to generate ROS, and transcriptional changes that occur during neutrophil extravasation in migratory and non-migratory phenotypes. These findings reveal new biological insights into human immunology. We find that human neutrophil-endothelial interactions stimulate the upregulation of genes involved with cellular adhesion, chemokine reception, and

ROS production in migratory neutrophils, priming them to possess increased migratory and ROS producing capabilities. Additionally, we find that these interactions have little to no effect on neutrophil phenotype for a subset of non-migratory neutrophils, likely indicating that pre-existing neutrophil heterogeneity results in varying neutrophil primed states.

2.2 Materials and Methods

2.2.1 Cell Culture

HUVECs (Lonza, #C2519A) were maintained in endothelial basal media-2 (EBM-2)(Lonza, #CC-3121) supplemented with the EGM-2 Bullet Kit (human EGF (hEGF), hydrocortisone, gentamicin, amphotericin-B, VEGF, hFGF-B, insulin-like growth factor-1 (R3-IGF-1, ascorbic acid, heparin, and 2% fetal bovine serum)(Lonza, #CC-3162). HUVECs were passaged with 0.25% trypsin-EDTA (Thermo Fisher, #25200056) prior to confluency and used from passage 3-10.

2.2.2 Human Primary Neutrophil Purification

Neutrophils were purified from whole blood using the Miltenyi Biotec MACSxpress Neutrophil Isolation Kit per the manufacturer's instructions (Miltenyi Biotec, #130-104-434) and residual red blood cells were lysed using MACSxpress Erythrocyte Depletion Kit (Miltenyi Biotec, #130-098-196). All donors were healthy and informed consent was obtained at the time of the blood draw according to the requirements of the institutional review board (IRB) per the declaration of Helsinki. Prior to loading, the purified neutrophils were stained with calcein AM at 10nM (Thermo Fisher, #C3100MP) according to the manufacturer's instructions.

2.2.3 LENS Device Fabrication

The LENS PDMS base was fabricated as previously described by Jiménez-Torres et al. Briefly, LumeNext devices consist of two components: an open chamber fabricated in PDMS (Dow Corning, Sylgard 184, 10:1 curing agent ratio) from an SU-8 (MicroChem, SU8-100) master via traditional soft lithography[74], and a PDMS rod that is form-casted from 25 gauge hypodermic needles. The rod is inserted into the central open chamber and the device is oxygen plasma bonded to a glass coverslip using a Diener Electronic Femto Plasma Surface System.

The LENS Stacks layers are fabricated using plastic micromilling methods [75]. Briefly, the Stacks layers are machined out of 1.2 mm thick polystyrene sheets (Good Fellow, # 640-597-67) on a CNC mill (Tormach, PCNC 770 mill). The layers are then deburred and soaked in DI water for 24 hours to remove leftover coolant from the machining process. The Stacks layers have alignment posts that fit into both the PDMS base and adjoining Stacks layers. Stacks layers are placed on top of the LumeNext base where the alignment posts act to keep both components aligned during ECM polymerization and experimentation.

2.2.4 Device and ECM preparation

Prior to loading ECM solution and cells, devices were UV sterilized for 20 minutes. All subsequent steps were performed under sterile conditions in a biosafety hood. To enable ECM attachment, the PDMS chamber was functionalized with 1% polyethylenimine (Sigma-Aldrich, #408727) in DI water followed by 0.1% Glutaraldehyde (Sigma-Aldrich, #G6257) in DI water. Devices were then washed three times with DI water to titrate out residual glutaraldehyde. A collagen-I/fibronectin

solution was prepared on ice by neutralizing high concentration rat tail collagen I (Corning, #354249) and fibronectin (Sigma-Aldrich, #F1141) to a pH of 7.2. The final collagen-I and fibronectin concentrations were 4 mg/mL and 10 µg/mL, respectively. The unpolymerized ECM was pipetted into the side ports of the device and allowed to crosslink at room temperature for 30 minutes before the devices were moved to a 37C cell incubator for an additional 30 minutes.

2.2.5 Cell Loading

Drops of cell culture media were added to the outlet ports (larger port) of each device and tweezers were used to remove the PDMS rods from the inlet ports (smaller port), resulting in a lumen filled with media. HUVECs were added to each lumen at 15,000 cells/µL. The devices were placed in an incubator and flipped upside-down every 20 minutes for a total time of 1 hour and 20 minutes to allow the HUVECs to adhere to all sides of the lumen. The lumens were then rinsed 3 times with media to wash out nonadherent cells, and the devices were placed in the incubator overnight to allow the cells to more firmly adhere and spread out.

2.2.6 Image Acquisition

Bright-field and fluorescent images were obtained using a Nikon TI Eclipse inverted microscope. Images were processed using Nikon Elements.

2.2.7 Image Analysis

Image analysis was done using the open-source software ImageJ. Neutrophils in the stacks layers were quantified by first z-projecting the z-stack taken of the device into a single plane. The number of cells in each stacks layer were then counted.

2.2.8 ROS Analysis

Neutrophil ROS production was measured using 10µM dihydrorhodamine 123 (Thermo Fisher, D23806) after stimulation with or without 1µM Phorbol 12-myristate 13-acetate (Sigma-Aldrich, P8139). Mean fluorescence intensity per cell was measured using ImageJ.

2.2.9 RT-qPCR Analysis

Neutrophils were recovered from disassembled LENS devices by using a manual pipetman to collect non-migratory neutrophils from the lumen and Accutase (STEMCELL Technologies #07920), a cell detachment solution of proteolytic and collagenolytic enzymes, to collect migratory neutrophils from the Stacks layers. Their mRNA was then isolated in 15µL 10mM Tris buffer using Dynabeads mRNA DIRECT Purification Kit (Invitrogen, #61011) per the manufacturer's instructions. Immediately preceding mRNA isolation, a reverse transcription reaction was run using iScript cDNA Synthesis kit (Bio-Rad, #170-8891) and the resultant cDNA was pre-amplified with SsoAdvanced PreAmp Supermix (Bio-Rad, #172-5160) and primers from Integrated DNA Technologies (Coralville, IA)(Supplementary Figure 3). Finally, qPCR reactions were run using iTaq Universal SYBR Green Supermix (Bio-Rad, #172-5121) in Roche's Lightcycler 480 II (Roche Molecular Systems, Indianapolis, IN), and a ΔΔCt analysis was run.

2.2.10 Statistical Analysis

Data were analyzed (Prism 7.0; GraphPad Software) using one-way ANOVA. Tukey's multiple comparison test with a 95% confidence interval was used when comparing different conditions.

2.3 Results

2.3.1 LENS Design

In order to create an organotypic model system to study neutrophil-endothelial interactions in real-time, with spatial control, we designed the LENS platform. The LENS technology consists of two basic components: a PDMS chamber that houses the endothelial lumen (LumeNext), and a stackable series of polystyrene (PS) tube sections (Stacks)(Figure 2.1). The PDMS chamber consists of two micromolded PDMS halves that fit together to form a space across which a PDMS rod can be threaded (Figure 2.1A). The rod is supported by struts on each end of the chamber to keep the rod from contacting surfaces within the chamber. Cut into the top of the chamber are five access ports; two gel-loading ports on either side of the rod, one access port directly above the middle of the rod which the stackable polystyrene tubes fit over, and two cell/media loading ports on either end of the rod (Figure 2.1B). The device is assembled by first aligning the two PDMS halves together, then threading the rod through the middle of the two halves, and lastly, the stackable tubes are placed on top of the access port (Figure 2.1C). Unpolymerized ECM is pipetted into the chamber and connected stacks layers through one of the gel loading ports and is allowed to set. This process creates a continuous ECM throughout the PDMS chamber and up into the Stacks layers (Figure 2.1D). The lumen structure is formed by pulling the PDMS rod from the device through the cell/media loading ports (Figure 2.1E). Cells and media can then be added

to the lumen through one of the cell/media loading ports and allowed to adhere to the lumen-wall. Once assembled, soluble and/or cellular components can be added to the system using additional Stacks layers placed on top of the existing stacks layers (Figure 2.1F).

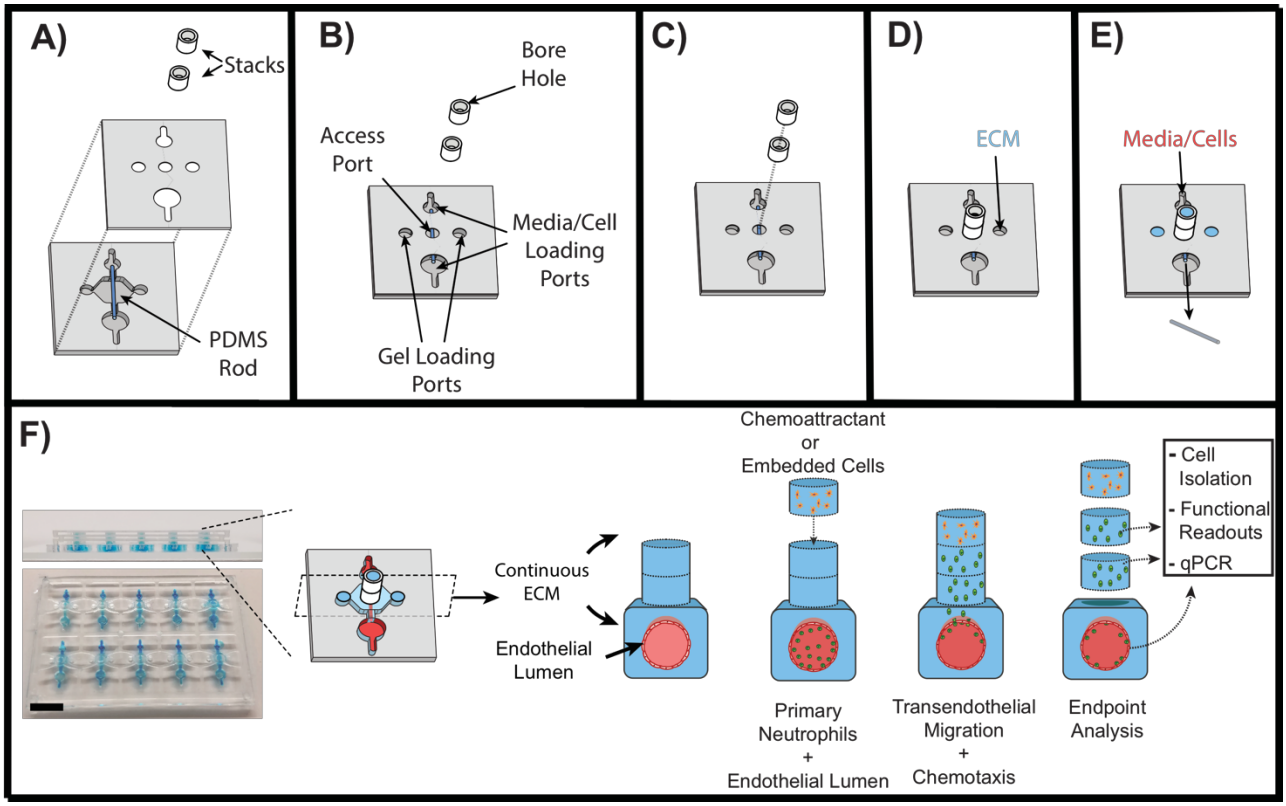

Figure 2.1: Schematic of LENS technology. A) Exploded view diagram of all the components of LENS. The LumeNext base is composed of two PDMS halves with a PDMS rod inserted in the middle. The Stacks components consist of polystyrene tube sections. B) Once assembled, the LumeNext base creates a chamber with five ports. C) The Stacks layers stack on top of each other directly over the central access port. D) Unpolymerized ECM can be added to one of two gel loading ports. This creates a continuous ECM throughout the entire device. E) Once the ECM polymerizes, the PDMS rod can be pulled out of the device and media and/or cells can be added

to the loading ports. F) Image of the LENS platform (Scale bar = 5mm) along with a schematic of a neutrophil migration assay. Primary neutrophils are loaded into an endothelial vessel and a chemoattractant (IL-8) is added to the top of the device. Neutrophils are allowed to migrate, after which the device is disassembled and the captured neutrophils can be further analyzed.

We aimed to create a device that had a continuous ECM in the Stacks layers that could be easily disassembled and reassembled, thus requiring robust ECM retention within each layer. The Stacks layers needed to have both inner-bore dimensions that maximized intra-layer ECM retention during disassembly, and spatial dimensions small enough as to remain relevant to neutrophil migratory distances *in vivo*. Additionally, since the Stacks layers needed to be made of a stiff material, such as polystyrene, fabrication methods also played a role in limiting the device's dimensions. To determine the optimum bore size for the Stacks layers, LENS devices consisting of a collagen I ECM and two stackable PS (Stacks) layers with a range of diameters (0.5mm, 0.75mm, 1mm) and heights (0.25mm, 0.5mm, 0.75mm), were assayed for collagen adherence to the side walls within each Stacks layer upon disassembly (Figure 2.2). Stacks layers with the largest bore diameter and smallest height had the lowest collagen retention rate (16.67% +/- 15.2) whereas the Stacks layers with the smallest bore diameter and largest height had the best collagen retention rate (83.33% +/- 5.8). Due to micromachining fabrication considerations, the final bore diameter for the Stacks layers was kept at 0.5mm. Although 0.75mm is a relatively large distance *in vivo*, the high collagen retention rate warranted the use of this height for these validation experiments. In the future, the platform could be modified to recapitulate smaller *in vitro* distances.

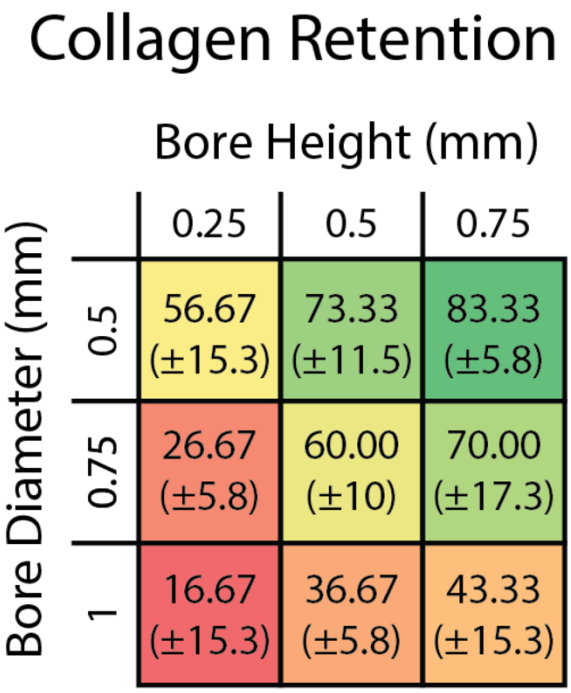

Figure 2.2: Table showing collagen retention rate in Stacks layers with various bore diameters and heights.

2.3.2 Characterization of LENS Capabilities

The LENS technology was designed to facilitate the introduction and isolation of cells from the microdevice without significantly perturbing the microenvironment (Figure 2.1F). In order to validate these capabilities for the capture of neutrophils, neutrophil migration experiments were conducted in LENS devices to assay for the cell capture capabilities of the devices (Figure 2.1F). Leukocyte trafficking occurs in response to a chemokine gradient. We characterized the gradient within the device using a diffusion model in COMSOL to estimate gradient characteristics in LENS (Figure 2.3). Using a porosity and density similar to a 4mg/mL collagen-I hydrogel and a diffusion coefficient of 8.974×10^{-7} cm^2 s^{-1}, consistent with 10kDa FITC-dextran (similar in size with known

neutrophil chemokines), we computed diffusion profiles over time between 0 min to 90 min (Figure 2.3A) [76][77]. Based on the COMSOL model, the gradient would begin to form at around 30 min and would persist for greater than 90 min (Figure 2.3B).

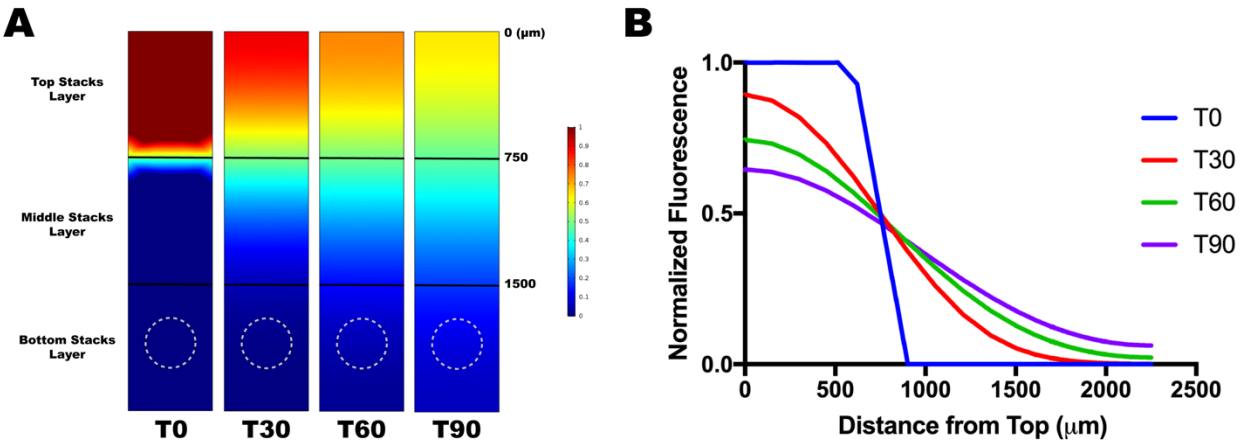

Figure 2.3: COMSOL model of 10 kDa FITC-dextran diffusion through a hydrogel similar in porosity and density to 4mg/mL Collagen-I in a LENS device. - A) Computed diffusion profiles at T = 0 min through T = 90 min. B) Quantified normalized fluorescence vs. distance from top of stacks layer at different time points.

Next, we investigated 10 kDa FITC-dextran diffusion in our 4 mg/mL collagen-I + 10 μg/mL fibronectin matrix, conditions shown to facilitate endothelial lumen formation and neutrophil migration [21]. A single Stacks layer, containing collagen-I/fibronectin and 10 kDa FITC-dextran was placed on top of two other Stacks layers containing only collagen-I/fibronectin, which permitted the dextran to diffuse (Figure 2.4A). Multiple devices were assembled and diffusion was allowed to take place for 30, 60, and 90 minutes, after which the devices were disassembled and the fluorescence was quantified for each layer (Figure 2.4B). From time 0 min to 30 min

there is a steep decline in the dextran gradient, however, from time 30 min to 90 min the deterioration of the gradient decreases and remains stable. Using the diffusion data in figure 3B we extrapolated a diffusion coefficient of 9.698 x 10^{-7} cm^2 s^{-1} for the 10 kDa FITC-dextran which consistent with our COMSOL model and demonstrates that a chemokine gradient can be formed in the LENS platform.

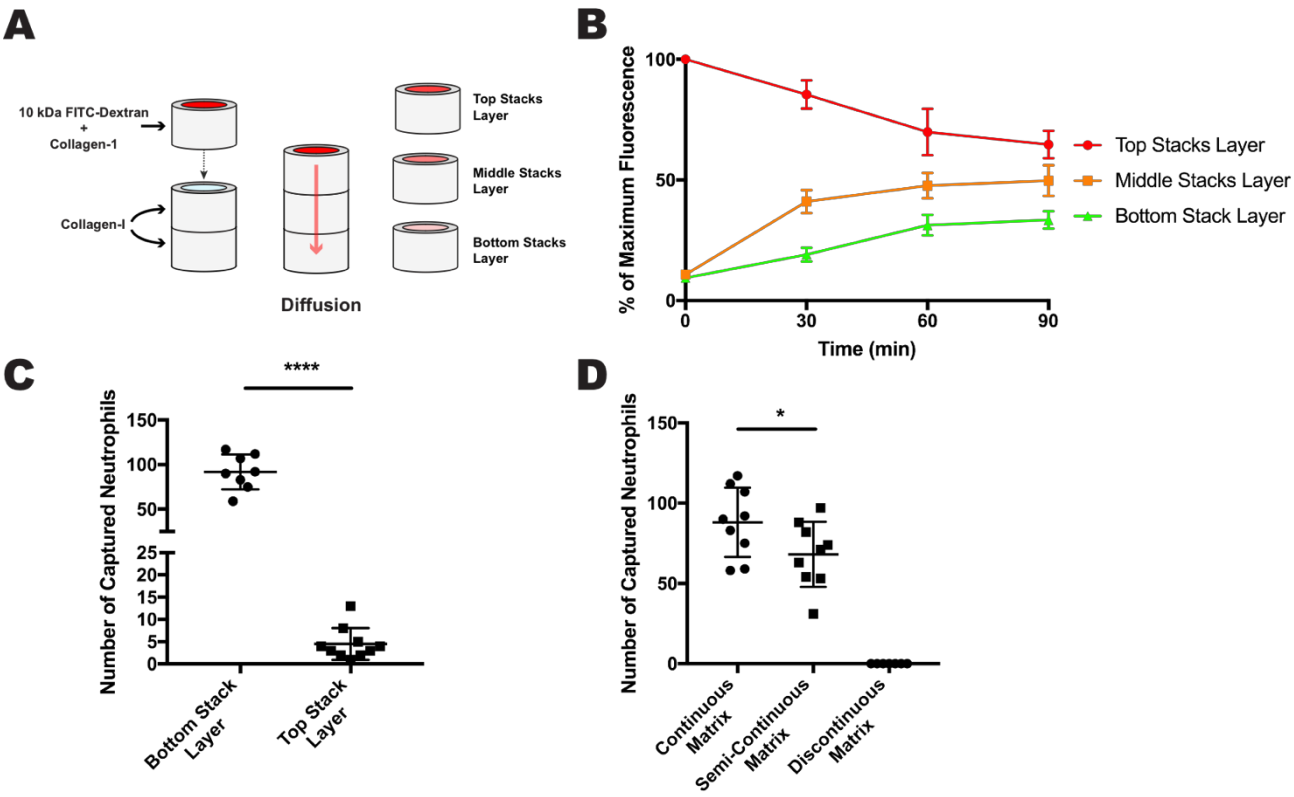

Figure 2.4: Diffusion and neutrophil migration in the stacks layers. A) A single stacks layer containing collagen-1 and 10kDa FITC-Dextran was placed on top of two other stacks layers, both containing collagen-I only. The FITC-dextran was allowed to diffuse into the bottom two layers for a certain amount of time. B) Results of the diffusion experiment showing average maximum fluorescence for each stacks layer over 90 minutes. C) Results of the double Stacks layer migration experiment showing number of captured neutrophils per layer. D) Results for the ECM continuity

experiments showing number of captured neutrophils per ECM condition. All data were quantified from neutrophils collected from 9 stacks layers across 3 independent experiments. Results are consistent across multiple donors. All bars represent mean plus SD. Asterisks represent significance between conditions. * = $p < 0.05$, **** = $p < 0.0001$

Being able to isolate migratory and non-migratory neutrophil phenotypes from LENS would allow for a range of cellular and molecular analyses and could offer valuable insight into human neutrophil biology. To test the cell isolation capabilities of LENS we ran a series of neutrophil migration experiments. A 4 mg/mL collagen-I and 10 μg/mL fibronectin continuous ECM was established inside two-Stacks layered devices along with a HUVEC vessel, like the setup in Figure 2F. Primary human, calcein-stained neutrophils were added to the endothelial lumen, and an IL-8 gradient, a known neutrophil chemoattractant which is secreted during inflammation, was established across the device. The neutrophils were allowed to migrate for 4 hours at 37C after which the device was disassembled, and the neutrophils in each Stacks layer were quantified (Figure 2.4C). While most migratory neutrophils reached the first stacks layer, ~10% of neutrophils migrated > 0.75 mm and were found within the second Stacks layer. These results confirm that neutrophil migration assays are compatible with LENS and that it has the resolution to differentiate between “fast” and “slow” migrating cells.

Cell migration is sensitive to many ECM properties including composition, porosity, stiffness, and especially continuity [78]. A method for adding cells to the ECM in LENS would be useful for studying cell-sourced chemoattractants and juxtacrine signalling, though the current method of

placing a Stacks layer containing embedded cells on top of a LENS device would result in a discontinuous matrix and possibly exclude neutrophils from trafficking properly. To overcome this ECM continuity issue, we used unpolymerized collagen-I to connect the additional Stacks layer to the LENS device, bridging the two ECMS, and assayed for neutrophil migration into the added layer (Figure 2.4D). In these experiments, there was a significant difference between the number of neutrophils captured in the continuous matrix condition and the semi-continuous condition with the latter capturing 23% fewer neutrophils, there were no neutrophils captured in the discontinuous matrix. This result indicates that while neutrophils prefer a continuous matrix, the semi-continuous collagen-I matrix is a viable alternative to a completely discontinuous matrix, and proves that cells can be added to the LENS matrix with minimal effects on neutrophil trafficking.

2.3.3 LENS as a tool to Study Neutrophil Trafficking

During the characterization of LENS, we have shown that this technology can facilitate the addition and retrieval of cells to a microscale device without disturbing the microenvironment significantly. To demonstrate the utility of these innovations, we used LENS to study the effect that endothelial cells have on neutrophil TEM/chemotaxis, and priming.

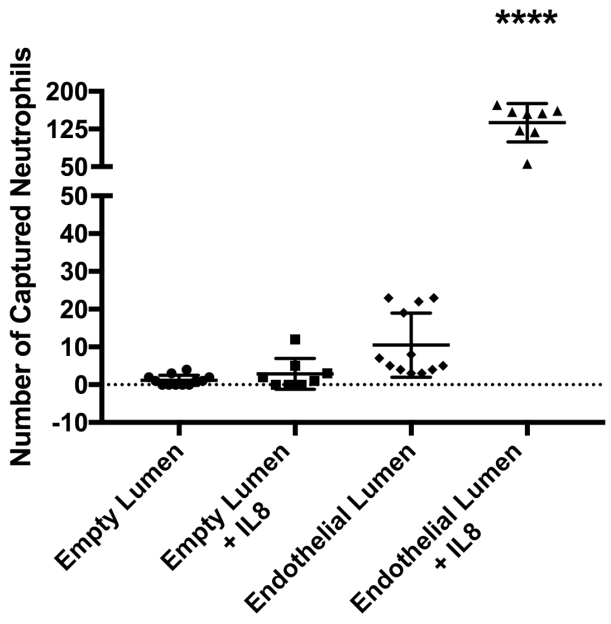

Figure 2.5: Neutrophil migration to IL-8 with and without and endothelial lumen. Results showing neutrophil migration in different microenvironmental conditions. All bars represent mean plus SD. All data were quantified from neutrophils collected from 12 stacks layers for no IL-8 conditions, and 8 stacks layers for +IL-8 conditions across 3 independent experiments. Results are consistent across multiple donors. Asterisks represent significance between conditions. **** = $p < 0.0001$

Neutrophil-endothelial interactions are critical for effective immune system function, however, quantifying this behavior and isolating cells for downstream analysis is difficult to do in current organotypic models.27 We first investigated the downstream effects of endothelial contact on neutrophil TEM/chemotaxis (Figure 2.5). Neutrophils were added to the lumen of LENS devices which was either an empty lumen with no endothelial cells or a HUVEC microvessel, and an IL-8

gradient was established vertically through the stacks layers. Neutrophils were allowed to migrate for four hours, after which the devices were disassembled, and the number of captured neutrophils were quantified. In empty (no endothelium) lumen conditions, an average of 1.17 neutrophils were captured in the stacks layer in the absence of a chemokine gradient, and 2.88 neutrophils were captured when exposed to an IL-8 gradient. Alternatively, in the endothelial lumen conditions, an average of 10.5 neutrophils were captured in the absence of a chemokine gradient, and 137.63 neutrophils were captured in the IL-8 condition. These results demonstrate LENS's ability to isolate populations of migratory neutrophils and suggests that it can be used to facilitate analysis of these cells further. Additionally, these results confirm that the endothelium significantly enhances a neutrophil's ability to sense and respond to chemokine gradients. While outside the scope of this, IL-8/glycosaminoglycan (GAG) dimerization and presentation on the luminal surface of the endothelium,[79] activation of neutrophil Integrin receptors,[80] and secretion of cytokines[21] could potentially contribute to these observations. While these factors contribute to enhancing neutrophil TEM and chemotaxis, the effect neutrophil-endothelial interactions have on neutrophil behavioral phenotype and downstream signaling is less clear.

It has previously been shown in mice that extravasation of neutrophils across the endothelium into the interstitium alters their phenotype and induces changes in transcription [81][82]. To test if the same is true for human cells, we first looked at how TEM affects a neutrophil's ability to produce ROS. Using single stacks-layer LENS devices containing HUVEC lumens, we ran a series of IL-8 migration experiments. After four hours of migration, devices were disassembled, both the lumen and stacks components were treated with either dihydrorhodamine 123 (DHR), or DHR

and Phorbol 12-myristate 13-acetate (PMA), and then the mean fluorescence intensity per cell (MFIPC) was measured over four additional hours (Figure 2.6). In the no-PMA control, neutrophil ROS production remained relatively low, peaking at 240 after three hours. There was a significant increase in ROS production during hours one and two for the migratory/HUVEC condition compared to the other PMA conditions. There were no significant differences within the other PMA treated samples. Differences in ROS generation between migratory and nonmigratory neutrophils in the same condition suggests an existing heterogeneity within the isolated neutrophil population. Furthermore, these results show that neutrophils that have undergone TEM, and not just chemotaxis, are primed to elicit a more robust ROS response. Whether this difference in functional phenotypes is pre-existing or acquired within the system remains unresolved.

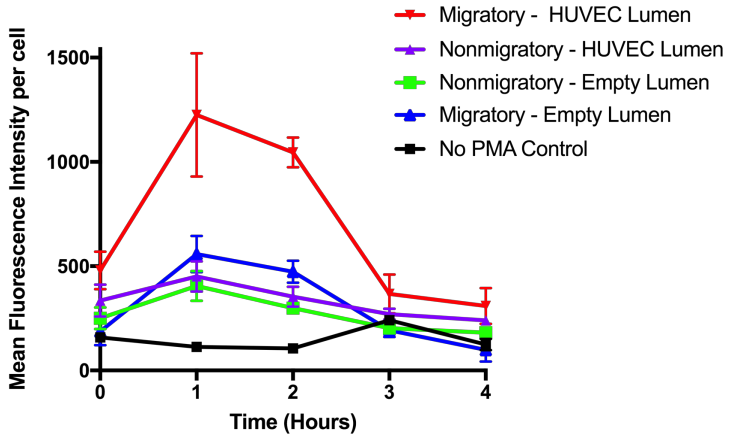

Figure 2.6: Neutrophil ROS – Average fluorescence measurements over four hours from migratory and nonmigratory neutrophils stained with DHR 123 and treated or not treated with PMA. Measurements were consistent across multiple donors.

Next we looked at how TEM altered gene transcription. To test this, migratory neutrophils (i.e. neutrophils that were captured in a stack layer), and non-migratory neutrophils (i.e. neutrophils that remained inside the lumen), were isolated from LENS devices containing endothelial and empty lumens, and an RT-qPCR analysis was conducted (Figure 2.7). Our genes of interest focused on both ROS production, and those previously shown to be altered during neutrophil priming, such as genes involved with chemotaxis, cell adhesion, and receptor signalling [28][83][84][85].

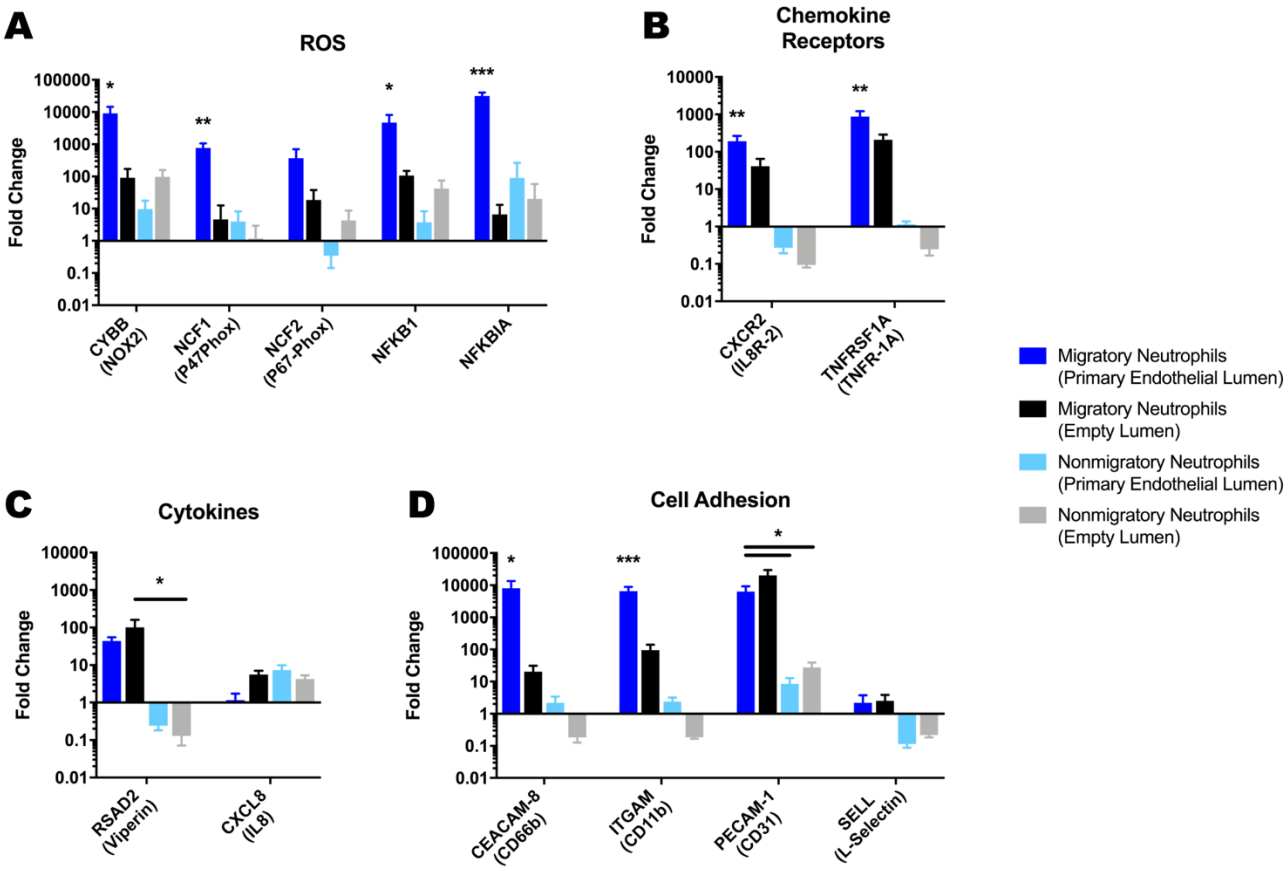

Figure 2.7: Gene expression is different in motile and non-motile neutrophils - qPCR results comparing gene expression of migratory and non-migratory neutrophils in LENS devices containing an empty collagen-I lumen or a HUVEC lumen investigating genes involved with A) production of ROS in neutrophils. B) neutrophil chemokine pathways. C) secreted cytokines. D) neutrophil adhesion. All bars represent mean plus SD. All data were quantified from neutrophils collected from 9 stacks layers for migratory neutrophils in endothelial lumen conditions, 30 stacks layers for migratory neutrophils in empty lumen conditions, and 9 lumens for both non-migratory neutrophil conditions across 3 independent experiments. Results are consistent across multiple donors. Asterisks represent significance between conditions. * = $p < 0.05$, ** = $p < 0.01$, *** = $p < 0.001$

For the genes associated with ROS generation, we found that the expression for all but NCF2 were significantly more upregulated for the migratory neutrophils in the endothelial lumen condition (>1000-fold) compared to the other conditions (<100-fold), though the trend in expression was similar for NCF2(Figure 2.7A). Amongst the other conditions, i.e. migratory/empty lumen, non-migratory/empty lumen, and non-migratory/endothelial lumen, there was no significant differences in gene expression for these genes. These results correlate with our ROS measurements and strongly suggest that the migratory neutrophils are acquiring a primed phenotype during TEM.

Both genes associated with chemokine receptors, CXCR2, and TNFRSF-1A, were significantly more upregulated in migratory neutrophils in endothelial lumen conditions compared to the

other conditions with fold increases of 190, and 882 respectively (Figure 2.7B). Migratory neutrophils in empty lumen conditions also displayed a significant increase in expression compared to both non-migratory conditions, although at a lower level with fold changes for CXCR2 and TNFRSF-1A were 40, and 209 respectively.

We also investigated chemokine genes involved in neutrophil migration (Figure 2.7C). RSAD2 was upregulated for both conditions involving migratory neutrophils, though only the neutrophils in the empty lumen condition displayed significance. Alternatively, both nonmigratory neutrophil conditions had decreased expression for RSAD2. CXCL8 was unchanged in migratory neutrophils in the endothelial condition, while it was slightly upregulated, between 4- and 7-fold, in the other conditions. While the endothelium has been associated with enhanced neutrophil priming, we did not expect all of our genes of interest would be altered [86][87].

CEACAM-8, ITGAM, PECAM1, and SELL all encode for genes associated with cellular adhesion and have been shown to be upregulated during priming, TEM and chemotaxis [88][89][90]. For all of these genes except SELL, migratory neutrophils in endothelial lumen conditions had >1000-fold increase in gene expression (Figure 2.7D). Expression of CEACAM-8 and ITGAM were significantly higher than all other conditions for the migratory neutrophils in an endothelial lumen. The difference in upregulation of CEACAM-8 and ITGAM between the two migratory neutrophil conditions, like the genes for ROS and chemokine reception, further illustrates the effect the endothelium has on neutrophil priming.

LENS allowed us to isolate phenotypically pure neutrophil populations. Due to this capability, we were able to directly correlate transcriptional changes in neutrophils to changes in functional phenotypes. We found that while there exists heterogeneity within isolated neutrophil populations, endothelial-neutrophil interactions are necessary for robust neutrophil chemotaxis and ROS generation. These changes correspond to the upregulation in transcription of genes associated with, but not limited to ROS production, chemokine reception, and cell adhesion.

2.4 Discussion

In this study, we developed an *in vitro* microscale technology able to produce organotypic endothelial-lumens with a simple way to add or capture cells from a device without disturbing the microenvironment. This added spatiotemporal control allowed us to model neutrophil priming, TEM, and chemotaxis with a focus on studying endothelial-neutrophil interactions.

In this study, we were able to directly correlate transcriptional changes in neutrophils to changes in functional phenotypes. This correlation was made possible by the design of LENS, and would've been difficult to do using other conventional methods such as 2D microfluidic devices or transwells. We found that while there exists heterogeneity within isolated neutrophil populations, endothelial-neutrophil interactions enhance neutrophil chemotaxis and ROS generation. These changes are at least partly due to the upregulation in transcription of genes associated with, but not limited to ROS production, chemokine reception, and cell adhesion.

In summary, the LENS platform is a new microfluidic technology that enables the study and isolation of migratory cells in a highly relevant and highly controllable manner. We used LENS to

look at neutrophil-endothelial interactions using human cells generating results consistent with those found in non-organotypic, 2D models of human neutrophil migration, implying LENS could be a valuable tool for further studies involving human neutrophil trafficking.

2.5 Acknowledgements

This work was supported in part by the NIH: National Institutes of Allergy and Infectious Diseases through R01 AI134749, and the University of Wisconsin Carbone Cancer Center Support Grant P30 CA014520.

2.6 Continued Work – Neutrophil Reverse Migration

One area of interest that could adapt well to the LENS technology is neutrophil reverse migration and inflammation resolution pathways [46]. Neutrophils, during inflammation resolution, were assumed to all undergo apoptosis followed by macrophage clearance of the apoptotic bodies. However, recent evidence in mouse and zebrafish models, as well as in human studies suggest that some neutrophils can migrate away from sites of inflammation and re-enter circulation in a process termed “neutrophil reverse migration.” While modelling this process using 2D microfluidics is useful, incorporating ECM and cellular components could give us a more physiologically relevant picture of this event. Additionally, modelling reverse migration in a system with a high degree of spatiotemporal control like LENS could allow us to analyse phenotypically enriched populations of neutrophils and provide insight into why only certain neutrophils reverse migrate.

Before using LENS to study neutrophil migration, we characterized neutrophil-macrophage-endothelial cell interactions in triple lumen, LumeNext devices due to the need for better optical clarity. As mentioned in the introduction, while there are several hypotheses as to what controls neutrophil RM, macrophages are well known to be key mediators in determining the outcome of the inflammatory response and there is evidence to suggest they play a major role in directing neutrophil RM. As inflammation progresses, macrophages are able to dramatically change their form and function in response to local environmental signals, switching from an M1, pro-inflammatory polarized state, to an M2, pro-wound healing state [91][92]. M1 macrophages secrete a milieu of pro-inflammatory cytokines including TNF-α, CCL2, IL-6, IL-1, IL-12, type I IFNs, CXCL1–3, CXCL5, and CXCL8, CXCL9, and CXCL10 [93]. Conversely, M2 macrophages are known to secrete cytokines involved in wound healing and tissue repair such as IL10, IL4, IL13, YM1, Arg-1, and MgI1. To test whether macrophages were involved in neutrophil RM we first tested their ability to attract and repel neutrophils.

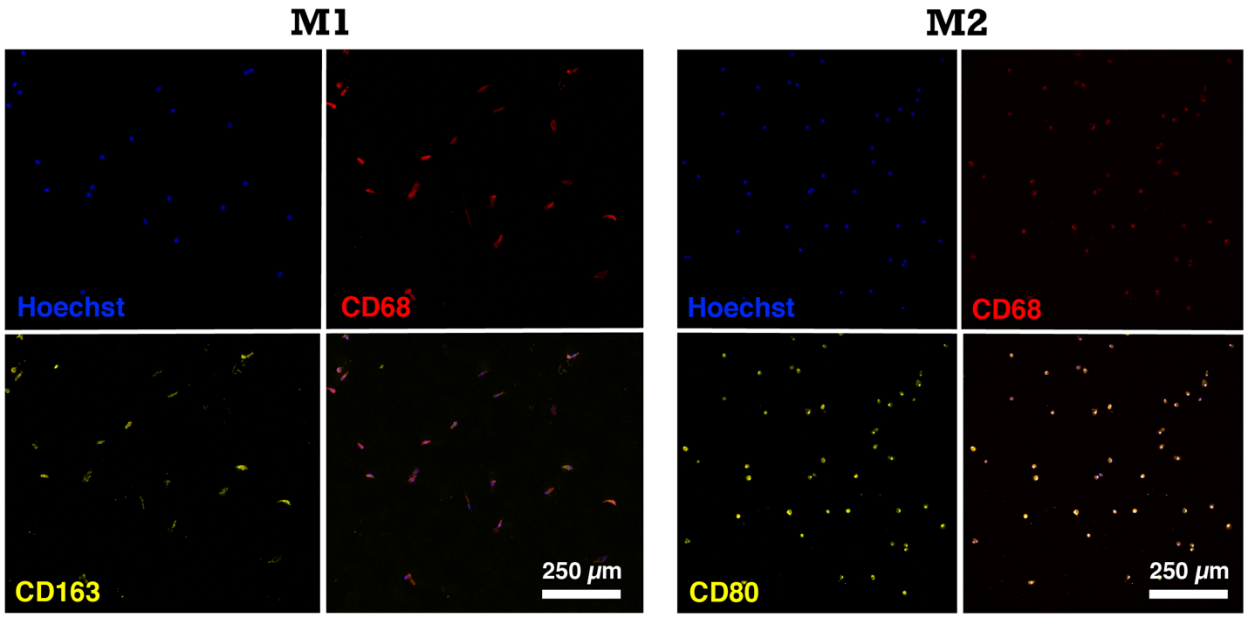

Figure 2.6.1: Immunofluorescent staining of primary monocyte-derived M1 and M2 macrophages – (Left) M1 polarized macrophages stained with Hoechst (blue), anti-CD68 (red), and anti-CD163 (yellow). (Right) M2 polarized macrophages stained with Hoechst (blue), anti-CD68 (red), and anti-CD80 (yellow).

We first established a protocol for isolating primary monocytes, differentiating them in macrophages, and polarizing them into M1 or M2 states (Figure 2.6.1). We confirmed their polarization based on immunofluorescent results and overall phenotype.

Next, to test their neutrophil chemoattractant capabilities, we seeded the middle lumen of a triple LumeNext device with either M1 or M2 macrophages, added neutrophils to one of the adjacent lumens at a 1:100 macrophage to neutrophil ratio, and allowed the neutrophils to migrate for 16 hours (Figure 2.6.2A). After 16 hours we quantified the number of neutrophils that transmigrated from the empty lumen into the hydrogel (Figure 2.6.2B). As expected, the number of transmigratory neutrophils was significantly higher when co-cultured with M1 macrophages compared to the M2 macrophages. This result suggests that our M1 macrophages' secretory profile is more pro-inflammatory compared to M2 macrophages'. Next, to test if macrophages possess the ability to induce neutrophil RM and if it is specific to a certain polarized state we seeded the central lumen of a triple lumen, LumeNext device with both neutrophils and M1 or M2 macrophages at a 1:100 macrophage to neutrophil ratio and allowed the neutrophils to migrate for 16 hours (Figure 2.6.2C). After 16 hours we quantified the number of neutrophils that had been repelled, "reverse migrated" and transmigrated from the empty lumen into the

hydrogel (Figure 2.6.2D). There was no significant difference in the number of neutrophils that RM between the no macrophage control, and the M1 macrophage condition however, the number of RM neutrophils in the M2 condition was significantly higher. Comparing the results from the recruitment experiment, with the results from this experiment show us that significantly fewer neutrophils undergo RM compared to those that are recruited. This indicates that M2 macrophages can induce neutrophil RM, though it occurs at low numbers in our model.

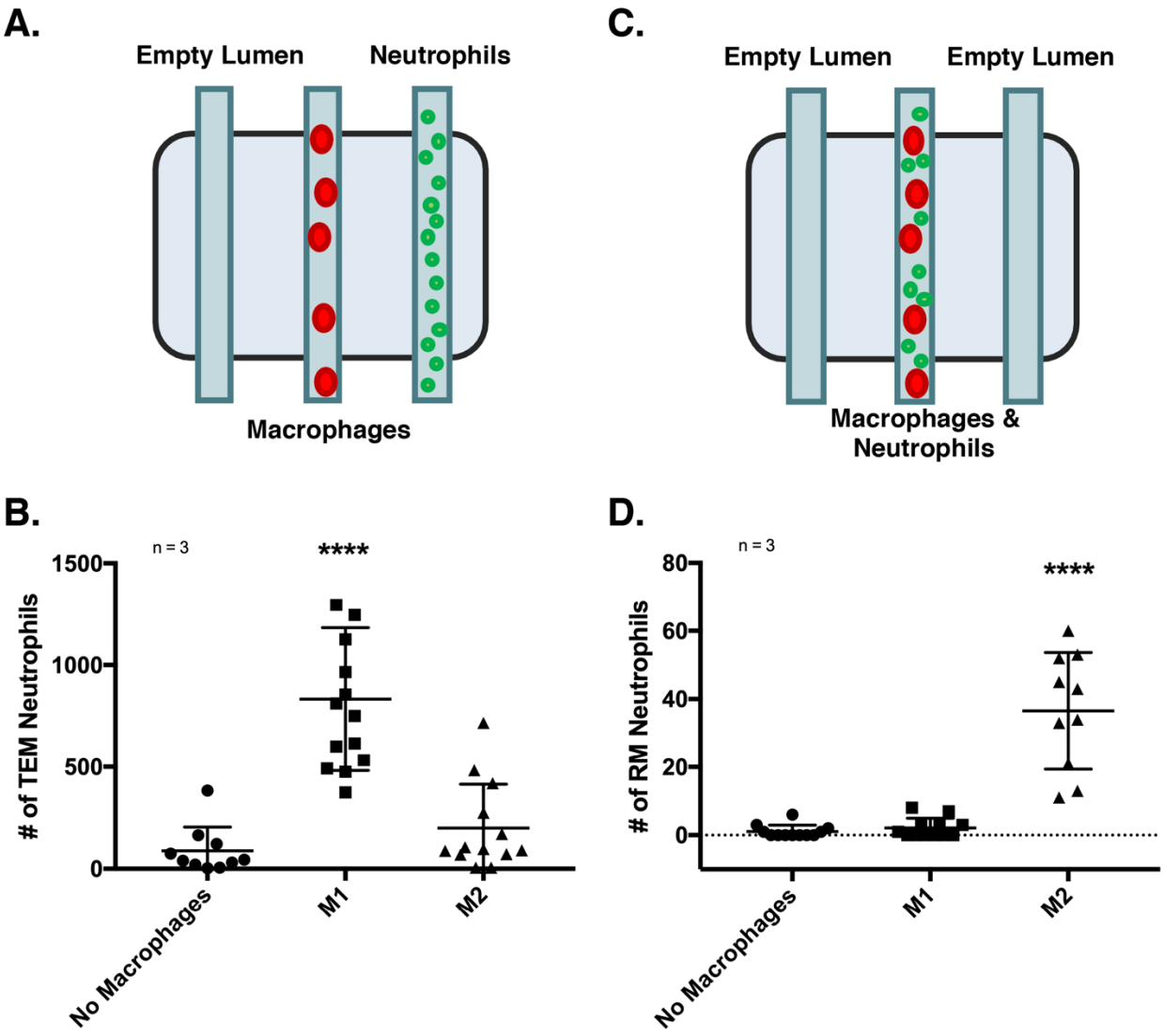

Figure 2.6.2: Neutrophil chemoattraction and chemorepellency to M1 and M2 macrophages – A) Experimental setup for assaying neutrophil recruiting capabilities of polarized macrophages. B) Results from recruitment experiment quantifying the number of neutrophils which transmigrated into the hydrogel. C) Experimental setup for assaying neutrophil repelling capabilities of polarized macrophages. D) Results from repelling experiment quantifying the number of neutrophils which transmigrated into the hydrogel. Results were consistent across donors. **** = $p < 0.0001$.

Next, we sought to determine if the RM phenotype we observed in our previous experiments was directional. Endothelial cells produce cytokines during inflammation. To see if neutrophils would reverse migrate away from macrophages directionally, we fabricated a primary endothelial lumen (HUVECs) in one of the side lumens of a triple lumen, LumeNext device, then seeded the central lumen with both neutrophils and M1 or M2 macrophages at a 1:100 macrophage to neutrophil ratio and allowed the neutrophils to migrate for 16 hours (Figure 2.6.3A). After 16 hours we quantified the number of neutrophils that reverse migrated and transmigrated from the empty lumen into the hydrogel (Figure 2.6.3B). Unsurprisingly, there was no difference in the number of neutrophils that reverse migrated between the M1 and no macrophage conditions, though the overall numbers of neutrophils increased from the previous experiment. In the M2 condition, the average number of RM neutrophils was greater compared to the other three conditions. Furthermore, when looking at the directionality of the neutrophil RM, we found that there was no significant directionality in the no endothelium/no macrophage, no macrophage, and M1 conditions (Figure 2.6.3C-E). However, in the M2 condition, significantly more neutrophils migrated towards the endothelial lumen compared to the opposite direction

(Figure 2.6.3F). These results suggest that the endothelium is involved in enhancing neutrophil RM and that M2-mediated neutrophil RM is directional to an endothelium.

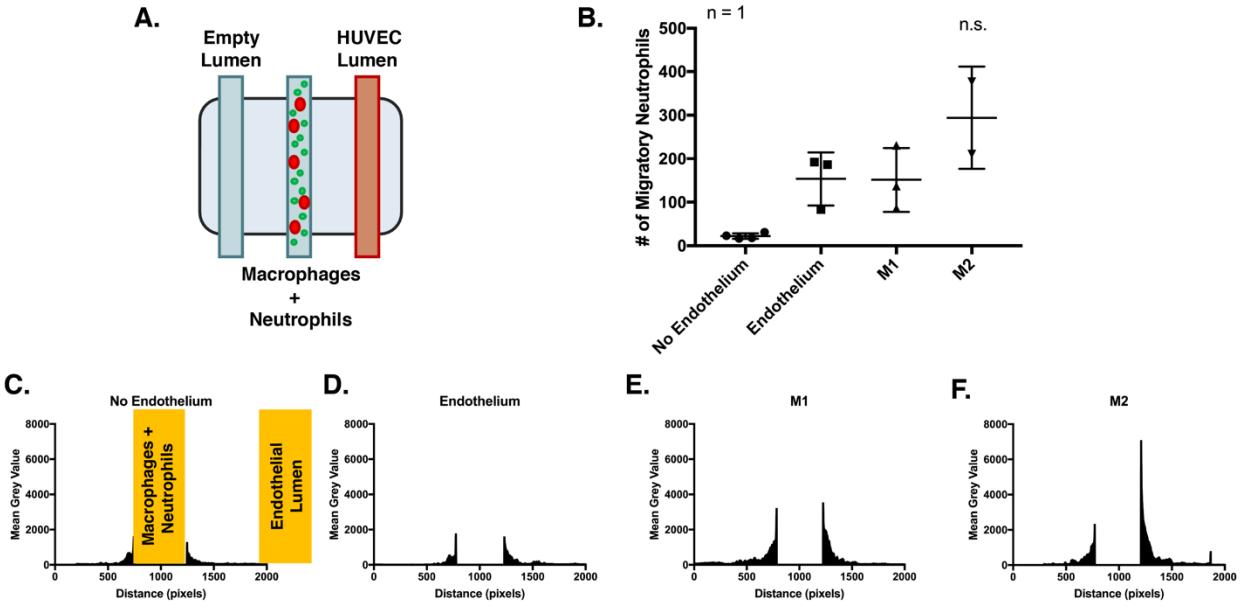

Figure 2.6.3: Neutrophil-macrophage-endothelial interactions and reverse migration – A) Experimental setup for assaying neutrophil RM capabilities of polarized macrophages in the presence of an endothelium. B) Results from neutrophil RM experiment quantifying the number of neutrophils which transmigrated into the hydrogel. C-F) Analysis of neutrophil migration directionality from the neutrophil RM experiment in "B". Results are displayed as the mean gray value, which is indicative of the number of neutrophils, versus distance on the x-axis of the image. Results were consistent across donors. **** = $p < 0.0001$.

While this work is not complete, we have presented here a microscale organotypic tissue model of neutrophil reverse migration composed entirely of primary human cells. We first used this model to test the chemoattractant and chemorepellent capabilities of M1 and M2 polarized macrophages and found that M2 macrophages possess the ability to induce neutrophil RM. Next

we used the model to test the directionality of M2 macrophage-induced neutrophil RM in response to the presence of an endothelium and found that the endothelium not only enhances neutrophil RM but it produces gradients of chemokines which the reverse migratory neutrophils follow. Our working model of neutrophil RM is summarized in Figure 2.6.4. While a more detailed discussion of future work can be found in Chapter 5.1, translating this work into the LENS technology will allow us to isolate reverse migratory neutrophils and interrogate them further.

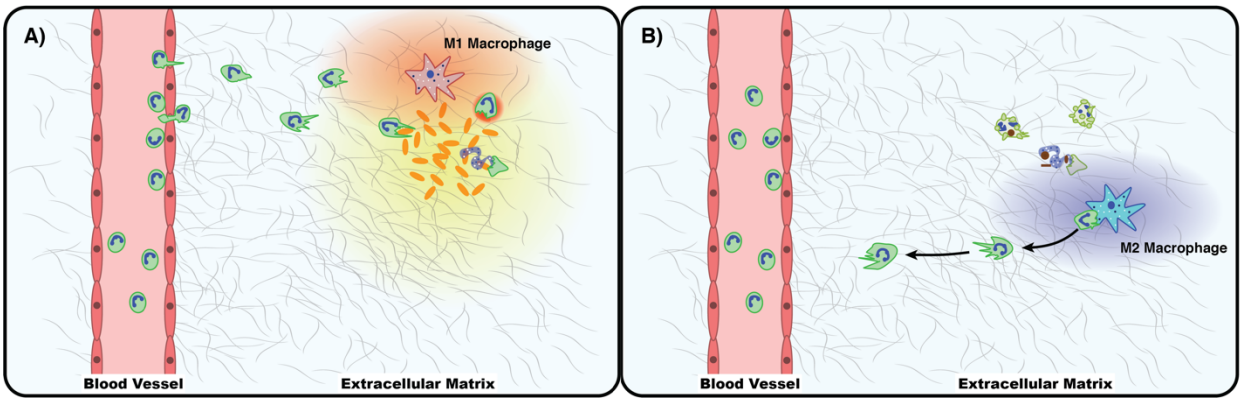

Figure 2.6.4 Diagram of our working model of neutrophil RM – A) Inflammation onset – neutrophils are recruited from blood vessels to sites of infection or injury, in part, by M1 polarized Macrophages. B) Inflammation Resolution – after the infection/injury is cleared away, M2 macrophages induce neutrophil RM.

Chapter 3:

Follistatin:Activin A axis regulates neutrophil motility in response to *P. aeruginosa*

This chapter has been adapted from the manuscript soon to be submitted to Blood in 2020 "Follistatin:Activin A axis regulates neutrophil motility in response to *P. aeruginosa*." **Patrick H. McMinn**, Sheena C. Kerr, and David J. Beebe.

Abstract

During infection with certain pathogens, including *Pseudomonas aeruginosa, Staphylococcus aureus*, *Listeria monocytogenes*, *Yersinia pestis*, *Toxoplasma gondii*, and *Leishmania major* neutrophils can traffic from sites of infection through the lymphatic vasculature, to draining lymph nodes to interact with resident lymphocytes. This process is poorly understood, in part, due to the lack of *in vitro* models of the lymphatic system. Recent work reporting a novel organotypic lymphatic endothelial lumen model found that Follistatin is secreted at high concentrations by lymphatic endothelial cells, and increased production during inflammation. Follistatin inhibits Activin A, a member of the TGF-β superfamily, and together, form a signaling pathway that has a role in regulating the innate and adaptive immune responses. While they are constitutively produced in the pituitary, gonads, and skin, both the major source of Follistatin and Activin A found in the serum and their effects on neutrophils are poorly understood. Here we report a tissue model that includes both blood and lymphatic endothelial lumens, and neutrophils and investigate neutrophil-lymphatic trafficking during infection with *P. aeruginosa*. We found that lymphatic endothelial cells are a significant source of both Follistatin and Activin A and that their expression increased in response to Pseudomonas infection. We characterized

the effects of Follistatin and Activin A on neutrophil trafficking and discovered that Activin A significantly decreased neutrophil chemotaxis which could be reversed by inhibition of Activin A with Follistatin or an anti-Activin A neutralizing antibody. Lastly, we determined that the Follistatin:Activin A ratio influences neutrophil trafficking with higher ratios increasing neutrophil chemotaxis.

3.1 Introduction

Previously, we developed a 3D microscale primary lymphatic vessel model called μLYMPH [94]. We reported that lymphatic vessels secrete high levels of follistatin which are 18-fold higher than HUVEC vessels in the same system. Treatment with IL-6 increased follistatin secretion 2-fold from lymphatic vessels. Follistatin, also known as activin-binding protein, is a glycoprotein that is expressed in nearly all human tissues [95]. Its main role in the body is the bioneutralization, or binding inhibition, of members of the TGF-β superfamily, activins in particular [96]. Activins, including the most highly produced member, Activin A, are a family of pleiotropic growth factors involved in cell proliferation, differentiation, wound healing, inflammation, apoptosis, and metabolism [97][98]. Together, follistatin and activin A form an axis whose serum concentrations have been shown to fluctuate during infection and modulate neutrophil trafficking *in vivo* [99]. Additionally, this axis has been identified as a novel pathway in lymphatic vessel maintenance and inflammation [100][101][102]. While it has yet to be determined how follistatin affects neutrophil function and phenotype, *in vitro* studies involving mouse and human neutrophils found that activin A increases their activation state and reduces chemotaxis towards N-formyl-Met-Leu-Phe (fMLP) [103]. Furthermore, a study looking at the involvement of Activin A during neonatal infections found that not only is Activin A significantly increased in the serum of septicemic neonates but that treatment of lipopolysaccharide (LPS)-activated leukocytes with Activin A significantly decreased IL-1β, IL-6, and IL-8 production and increased IL-10 production [102][104].

To investigate the effect of follistatin on lymphatic trafficking during infection, we developed an *in vitro* model of infection that contained blood and lymphatic vessels in an extracellular matrix that was infected with *P. aeruginosa*. Using this model we demonstrate that neutrophils exhibit different migratory potential to *P. aeruginosa* when in the presence of a blood vessel, lymphatic vessel, or both indicating that endothelial-lymphatic interactions alter neutrophil trafficking during infection. Furthermore, we identify co-culture effects in follistatin and activin A concentrations in our system and find that the follistatin/activin A ratio modulates neutrophil transendothelial migration during infection. Our findings demonstrate a potential role for the follistatin/activin A axis in regulating neutrophil-lymphatic trafficking during infection. Furthermore, this model highlights the importance of studying neutrophil trafficking in a physiologically relevant environment that integrates multicellular systems and recapitulates *in vivo* structures.

3.2 Materials and Methods

3.2.1 Cell Culture

HLECs (ScienCell, #2500), and HUVECs (Lonza, #C2519A) were maintained separately in standard culture flasks coated with 5µg/cm^2 fibronectin (F1141, Sigma Aldrich) in endothelial basal media-2 (EBM-2)(Lonza, #CC-3121) supplemented with the EGM-2 Bullet Kit (human EGF (hEGF), hydrocortisone, gentamicin, amphotericin-B, VEGF, hFGF-B, insulin-like growth factor-1 (R3-IGF-1, ascorbic acid, heparin, and 2% fetal bovine serum)(Lonza, #CC-3162). Both cell types were passaged with 0.25% trypsin-EDTA (Thermo Fisher, #25200056) prior to confluency and used

from passage 3-10. All cultures were kept in a humidified incubator at 37 °C with 5% CO_2.

3.2.2 *P. aeruginosa* culture

P. aeruginosa and *P. aeruginosa*-mCherry strains were used. One colony from an LB plate was grown overnight in 5 mL LB. The next day the culture was diluted 1:5 in fresh media and grown for 1.5 hours. One microliter bacterial culture was pelleted by centrifugation and resuspended in 100 mL EGM-2 MV media. The optical density (OD) was measured and diluted in EGM-2 MV media to OD_{600nm} 0.5. EGM-2 MV media contain the bacteriostatic antibiotics gentamicin/amphotericin; therefore, in iEC media, the bacteria do not replicate but are alive. The *P. aeruginosa*-mCherry strain was used to visualize bacterial diffusion, and the *P. aeruginosa* strain was used in migration experiments.

3.2.3 Human Primary Neutrophil Purification

Neutrophils were purified from whole blood using the Miltenyi Biotec MACSxpress Neutrophil Isolation Kit per the manufacturer's instructions (Miltenyi Biotec, #130-104-434) and residual red blood cells were lysed using BD Pharm Lyse (BD Biosciences, #555899). All donors were healthy and informed consent was obtained at the time of the blood draw according to the requirements of the institutional review board (IRB) per the declaration of Helsinki. Prior to loading, the purified neutrophils were stained with calcein AM at 10nM (Thermo Fisher, #C3100MP) according to the manufacturer's instructions.

3.2.4 Device Fabrication

The PDMS LumeNext devices were fabricated as previously described by Jiménez-Torres et al [69]. Briefly, LumeNext devices consist of two components: an open chamber fabricated in PDMS (Dow Corning, Sylgard 184, 10:1 curing agent ratio) from an SU-8 (MicroChem, SU8-100) master via traditional soft lithography,[105] and a PDMS rod that is form-casted from 25 gauge hypodermic needles. The rod is inserted into the central open chamber and the device is oxygen plasma bonded to a glass coverslip using a Diener Electronic Femto Plasma Surface System.

3.2.5 Device and ECM preparation

Prior to loading ECM solution and cells, devices were UV sterilized for 20 minutes. All subsequent steps were performed under sterile conditions in a biosafety hood. To enable ECM attachment, the PDMS chamber was functionalized with 1% polyethylenimine (Sigma-Aldrich, #408727) in DI water followed by 0.1% Glutaraldehyde (Sigma-Aldrich, #G6257) in DI water. Devices were then washed three times with DI water to titrate out residual glutaraldehyde. A collagen-I/fibronectin solution was prepared on ice by neutralizing high concentration rat tail collagen I (Corning, #354249) and fibronectin (Sigma-Aldrich, #F1141) to a pH of 7.2. The final collagen-I and fibronectin concentrations were 4 mg/mL and 10 μg/mL, respectively. The unpolymerized ECM was pipetted into the side ports of the device and allowed to crosslink at room temperature for 30 minutes before the devices were moved to a 37C cell incubator for an additional 30 minutes.

3.2.6 Cell Loading

Drops of cell culture media were added to the outlet ports (larger port) of each device and tweezers were used to remove the PDMS rods from the inlet ports (smaller port), resulting in a lumen filled with media. HUVECs were added to each lumen at 15,000 cells/μL using passive pumping [106]. The devices were placed in an incubator and flipped upside-down every 20 minutes for a total time of 1 hour and 20 minutes to allow the HUVECs to adhere to all sides of the lumen. The lumens were then rinsed 3 times with media to wash out nonadherent cells, and the devices were placed in the incubator overnight to allow the cells to more firmly adhere and spread out.

3.2.7 Cell-based Assays

Neutrophil migration assays were conducted using *Pseudomonas aeruginosa* grown in LB broth to an OD_{600} of 0.25 and then washed and resuspended in EGM-2 cell culture media.

To inhibit HUVEC cytokine secretion, HUVEC lumens were fabricated using the previously described methods and then treated with 5 μg/mL Brefeldin A (BioLegend, #420601) for 12 hours. The system was then washed three times and then HLECs were seeded into the adjacent collagen lumen and allowed to adhere and become confluent for 12 hours. Neutrophil migration experiments were performed immediately preceding.

Activin A blocking experiments were carried out using 100 μg/mL of either Purified Mouse IgG2b, κ Isotype Ctrl Antibody (BioLegend, #401212), Ultra-LEAF™ Purified anti-Activin A Antibody (BioLegend, # 693603), or 200 ng/mL recombinant human Follistatin (BioLegend, #776004) supplemented into the EGM-2 used for the experiment.

The Activin A/Follistatin chemotaxis experiments were conducted using 200 ng/mL recombinant human Activin A (BioLegend, #592002) or 200 ng/mL recombinant human Follistatin supplemented into the EGM-2 used in the experiment.

The Activin A doping experiments were conducted using 200 ng/mL recombinant human Activin A (BioLegend, #592002) supplemented into the EGM-2 used in the experiment.

Follistatin:Activin A ratio experiments were conducted using a combined 8 µg/mL of recombinant human Follistatin (BioLegend, #776004), and recombinant human Activin A (BioLegend, #592002) supplemented into the EGM-2 used in the experiment.

3.2.8 Cytokine Quantification

Cytokines secreted into the media for each mono- and co-culture condition was analyzed using a custom human ProcartaPlex multiplex panel for Follistatin, Fractalkine (CX3CL1), GM-CSF, IFN-γ, IL-1α, IL-6, IL8 (CXCL8), IL-10, MIP-3α (CCL20), MMP-3, MMP-9, SDF-1α (CXCL12), and TNFα. (Thermo Fisher, PPX-13), and a human Activin A Quantikine ELISA (R&D Systems, #DAC00B). Media was collected from 16 individual devices (7 µl per vessel) and pooled to generate sufficient volume for two technical replicates per experimental condition for each ELISA kit. The samples used for the ProcartaPlex multiplex panel were diluted 1:4 with the proper diluent, prepared following manufacturer instructions, and measured using the MAPGPIX system (Luminex Corp.). The samples for the Quantikine ELISA kit were diluted 1:2 in the appropriate diluent, prepared following manufacturer instructions, and measured using the PHERAstar Multimode plate reader (BMG Labtech). Cytokine concentrations were extrapolated from a standard curve for each ELISA.

3.2.9 Image Acquisition

Bright-field and fluorescent images were obtained using a Nikon TI Eclipse inverted microscope. Images were processed using Nikon Elements.

3.2.10 Image Analysis

Image analysis was done using the open-source software ImageJ. Migratory neutrophils in the collagen gel outside the empty or endothelial lumens were quantified by first z-projecting the z-stack taken of the device into a single plane. The number of cells in each stacks layer were then counted.

3.2.11 Statistical Analysis

Data were analyzed (Prism 7.0; GraphPad Software) using one-way ANOVA. Tukey's multiple comparison test with a 95% confidence interval was used when comparing different conditions.

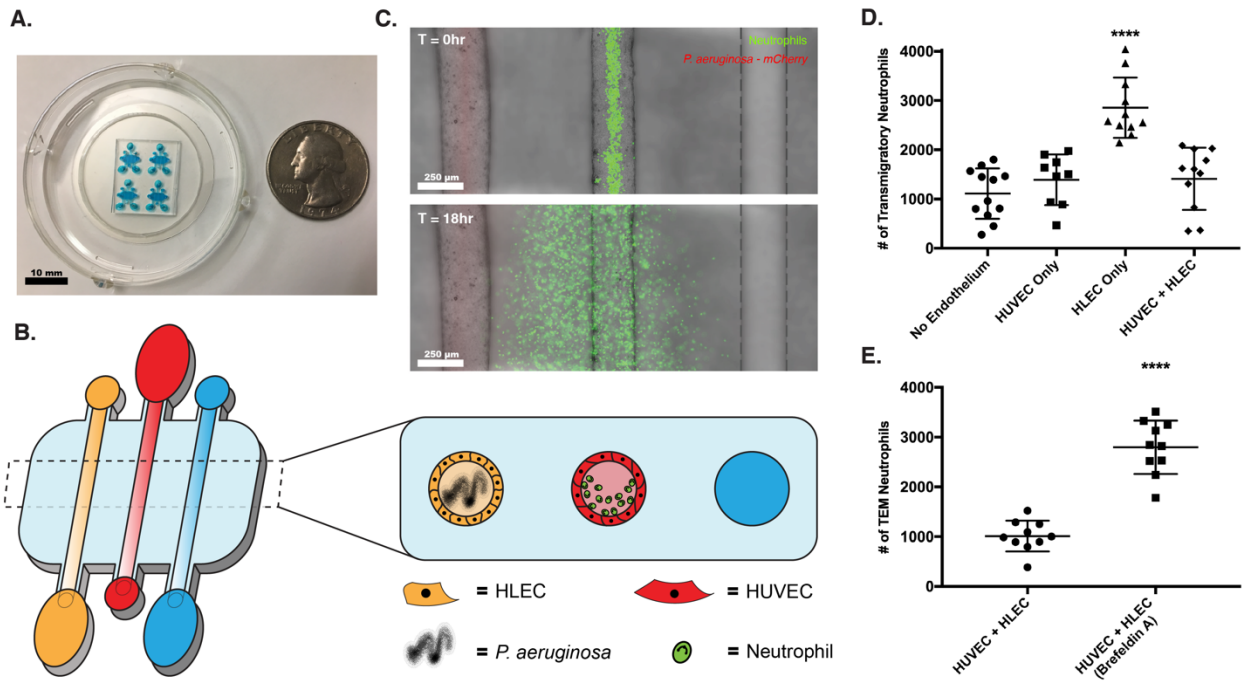

Figure 3.1: Organotypic infection model and its effects on neutrophil chemotaxis - A) Photo of the triple-lumen device used in all of our experiments filled with collagen-I and blue food coloring. US quarter for scale. B) Diagram of our organotypic infection model. The model consists of a *P. aeruginosa*-filled human lymphatic endothelial cell (HLEC) vessel on the left (yellow), a primary neutrophil-filled human umbilical vein endothelial cell (HUVEC) vessel in the middle (red), and an unlined lumen on the right (blue). C) Representative timelapse image of calcein-AM-stained neutrophil chemotaxis to *P. aeruginosa*-mCherry over 18-hours in our model. D) Quantification of neutrophil transmigration in different co-culture conditions in response to *P. aeruginosa*. * represents significance from the no endothelium control. E) Quantification of neutrophil TEM in response to *P. aeruginosa* in HUVEC + HLEC conditions, and Brefeldin A-treated HUVEC + HLEC conditions. * represents significance from the untreated HUVEC + HLEC condition. Results were consistent across donors. **** = $p < 0.0001$.

3.3 Results

3.3.1 Lymphatic endothelial vessels enhance neutrophil chemotaxis to *P. aeruginosa*

To investigate the effects endothelial and lymphatic vessels have on neutrophil trafficking, we further developed a microscale *in vitro* model based on the LumeNext platform (Figure 3.1A) [69]. Briefly, this technology allows creation of lumen structures out of a variety of synthetic and natural hydrogels which can then be seeded with endothelial cells to form a confluent monolayer vessel model. For these experiments, we used triple lumen devices consisting of an unlined (no endothelial cells) lumen filled with cell culture media to balance out interstitial flow, a HUVEC or empty lumen in the middle filled with human neutrophils, and an HLEC or empty lumen filled with *P. aeruginosa* (Figure 3.1B,C). Neutrophils that left the central lumen and entered the collagen hydrogel, transmigratory neutrophils, were quantified after 18 hours, long enough for robust neutrophil chemotaxis (Figure 3.1D). In the empty condition, no endothelial or lymphatic vessels, we observed an average of 1110 ± 511 transmigratory neutrophils in response to *P. aeruginosa*. Despite the endothelial barrier, in the HUVEC only condition, we observed slightly more migratory neutrophils with an average of 1391 ± 515. In the HLEC only condition, we observed the highest number of transmigratory neutrophils with an average of 2855 ± 612, suggesting that the lymphatic vessel is secreting additional chemokines or paracrine signals that are enhancing neutrophil transmigration. Surprisingly, when a HUVEC lumen was added to the system, we observed significantly fewer neutrophils transmigrating with an average of 1411 ± 633 neutrophils.

Bacteria and bacterial products like lipopolysaccharide (LPS) freely diffuse throughout the device, with smaller molecules diffusing across to adjacent lumens in < 1 hour [21]. While many of these compounds are chemotactic for neutrophils, they are also pro-inflammatory and are recognized by endothelial vessels, which in turn release their own pro-inflammatory cytokines [107]. Therefore, we treated a HUVEC lumen with Brefeldin A (cytokine secretion inhibitor), to study the role of endothelial vessel secreted cytokines in transmigration of neutrophils when compared with HLEC mono-culture. Following treatment, we washed any residual Brefeldin A from the device, seeded the second lumen with HLECs, and then ran the same neutrophil chemotaxis experiments in response to *P. aeruginosa* (Figure 3.1E). When cytokine secretion was not inhibited, we observed an average of 1010 ± 310 transmigratory neutrophils, consistent with previous results. When cytokine secretion was blocked from HUVECs, we saw a corresponding increase in the number of transmigratory neutrophils to 2772 ± 445, comparable to migration in the HLEC only condition. These results suggest that the reduction in the number of transmigratory neutrophils in the co-culture condition compared to the HLEC only condition was due to pro-inflammatory cytokines secreted by the HUVEC endothelium. This result also confirms that secreted factors from the lymphatics enhance neutrophil transmigration and chemotaxis.

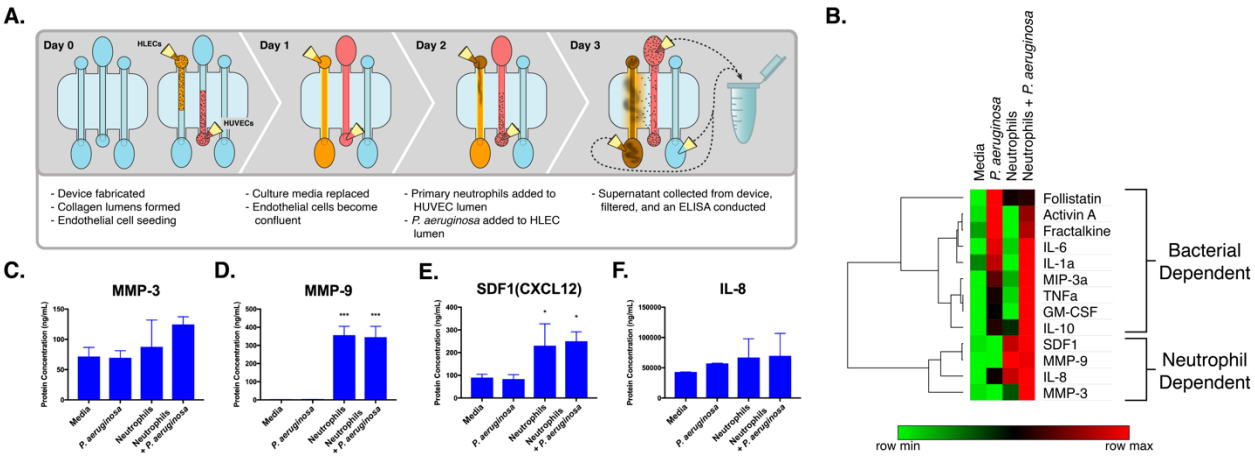

Figure 3.2: ELISA analysis of secreted factors in infection model - A) Diagram of experimental setup. B) Hierarchical cluster analysis of our ELISA data from HUVEC + HLEC condition. Analysis clustered cytokines into two groups, ones that underwent bacterial-dependent changes, and neutrophil-dependent changes. C-F) ELISA results from HUVEC + HLEC conditions depicting cytokines that underwent neutrophil-dependent changes. * represents significance from media condition. Results were consistent across donors. * = $p < 0.05$, *** = $p < 0.001$.

3.3.2 Microenvironmental conditions affect Follistatin and Activin A secretion

To better understand the secreted factors responsible for increasing neutrophil chemotaxis in our infection model, and to see how follistatin and activin A levels changed during infection, we ran an ELISA on supernatant collected after 18 hours from devices with no endothelium, HUVEC only, HLEC only, and HUVEC + HLEC lumens, filled with either media, *P. aeruginosa*, neutrophils, or neutrophils and *P. aeruginosa* (Figure 3.2A). We screened for 14 analytes which included follistatin and activin A, acute-phase inflammatory mediators, IL-1α, IL-6, and TNFα, neutrophil

chemokines, Fractalkine (CX3CL1), IL8 (CXCL8), MIP-3α (CCL20), and SDF-1α (CXCL12), neutrophil effector molecules, MMP-3, MMP-9, and other inflammation-related cytokines of interest, GM-CSF, IFN-γ, and IL-10 [108][109][110]. Using a hierarchical cluster analysis of the cytokine concentrations from the HUVEC + HLEC condition, we found that cytokines clustered into two distinct categories based on their expression patterns; cytokines that undergo neutrophil-dependent changes and bacterial-dependent changes (Figure 3.2B).

As expected, both neutrophil effector molecules, MMP-3 and MMP-9 increased when neutrophils were present in the HUVEC + HLEC condition (Figure 3.2C,D). MMP-9 is strongly correlated with neutrophil function and was measured at low levels, < 25.5 ng/mL, without neutrophils present [111]. MMP-3, on the other hand, was detected in both neutrophil-free conditions, but its levels increased with the addition of neutrophils. SDF-1α is a strong chemotactic chemokine for lymphocytes and is associated with the regulation of neutrophil mobilization from bone marrow [112][113]. Like MMP-3, SDF-1α was measured at lower levels in both neutrophil-free conditions, < 90.1 ng/mL, and increased with the addition of neutrophils to > 230.5 ng/mL in the HUVEC + HLEC conditions (Figure 3.2E). Lastly, though not significant, the expression of IL-8 increased slightly with the addition of neutrophils (Figure 3.2F). These results confirm that neutrophils are actively involved in signaling during infection and their presence in our infection model is important to proper paracrine functioning of the endothelium.

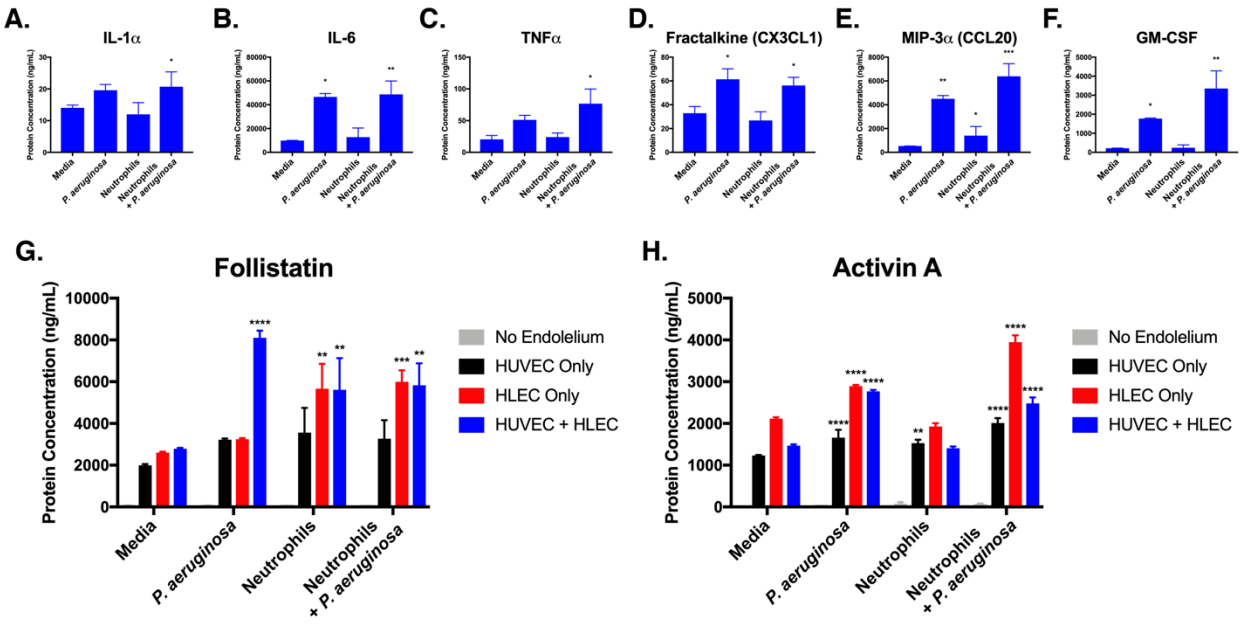

Figure 3.3: Bacterial-dependent changes in cytokine concentrations - A-F) ELISA results from HUVEC + HLEC conditions depicting cytokines that underwent bacterial-dependent changes. * represents significance from media condition. G-H) ELISA results from all co-culture conditions depicting dynamics of Follistatin G) and Activin A H) expression. * represents significance from respective media conditions. Results were consistent across donors. * = $p < 0.05$, ** = $p < 0.01$, *** = $p < 0.001$, **** = $p < 0.0001$.

Proteins that underwent bacterial-dependent changes included all of the acute inflammatory mediators, IL-1α, IL-6, and TNFα, putative neutrophil chemokines, Fractalkine (CX3CL1), and MIP-3α (CCL20), GM-CSF, IL-10, and both Follistatin and Activin A (Figure 3.3). Of the acute inflammatory mediators, IL-6 was expressed at the highest concentration, > 46,667 ng/mL, when *P. aeruginosa* was present in the HUVEC + HLEC condition (Figure 3.3B). Conversely, IL-1α was expressed at the lowest levels, ~20 ng/mL when *P. aeruginosa* were present (Figure 3.3A). Interestingly, Fractalkine and MIP-3α expression increased significantly, > 56.2 ng/mL and

>4502.2 ng/mL respectively when *P. aeruginosa* was present in the HUVEC + HLEC condition (Figure 3.3D,E) and were produced primarily by the HLEC lumen. GM-CSF expression increased with the addition of *P. aeruginosa*, 1771.2 ng/mL, however, its expression almost doubled, 3352.8 ng/mL, with the addition of *P. aeruginosa* and neutrophils while no significant GM-CSF production by the neutrophils themselves (Figure 3.3F). IL-10, an anti-inflammatory mediator, while clustered with the cytokines that underwent bacterial-dependent changes, exhibited minimally detectable levels of expression, < 3 ng/mL.

Follistatin was the highest expressed cytokine, > 5827.7 ng/mL, besides IL-6, when *P. aeruginosa* was present in the HUVEC + HLEC condition (blue) (Figure 3.3G). Though the expression of Follistatin in the HUVEC + HLEC condition followed a bacterial-dependent pattern, its expression in the HLEC only conditions (red) corresponded to a neutrophil-dependent response, suggesting important paracrine signaling between neutrophils and the lymphatic vessel in terms of Follistatin expression. Unlike Follistatin, Activin A followed a bacteria-dependent pattern for all endothelial culture conditions, HUVEC only, HLEC only, and HUVEC + HLEC (Figure 3.3H), with the highest concentrations of Activin A being produced by the HLEC only conditions, > 2892.3 ng/mL, with bacteria present. Though neutrophils have been reported as significant sources of Activin A, we were unable to detect significant quantities of Activin A in our experiments, < 76.9 ng/mL [114]**.** Together these data suggest that while Follistatin and Activin A were produced by both HUVEC and HLEC endothelial vessels, the lymphatics were a more significant source of both cytokines. Furthermore, the expression of Follistatin and Activin A changed more dynamically in the HLEC only conditions.

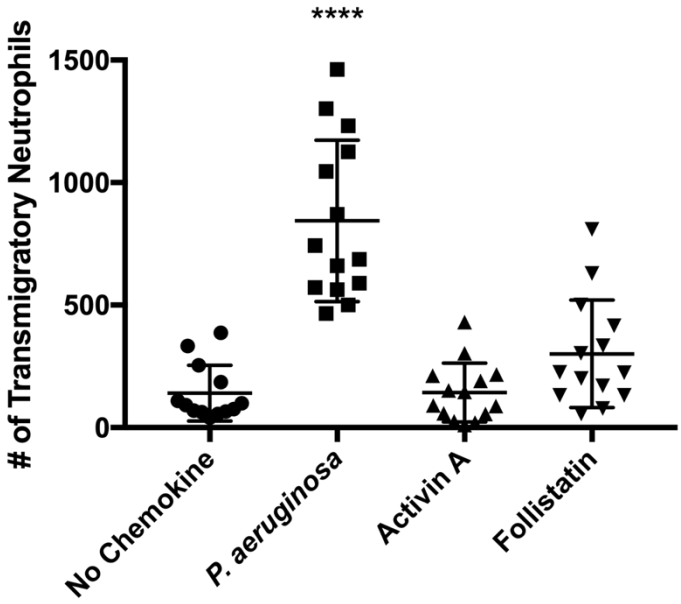

Figure 3.4 Neutrophil chemotaxis towards Activin A and Follistatin

3.3.3 Follistatin/Activin A regulate neutrophil trafficking during infection

Previous reports indicate that Activin A reduces neutrophil chemotaxis and TEM in response to N-Formyl-Met-Leu-Phe (fMLP) [103]. To investigate if Activin A can modulate neutrophil chemotaxis during infection, we compared neutrophil trafficking towards *P. aeruginosa* in the presence and absence of Activin A. We first quantified the chemoattractant capabilities of Activin A and Follistatin using an empty (no endothelial cells) triple lumen device with neutrophils in the middle and either media, *P. aeruginosa*, Activin A, or Follistatin in a side lumen. After 18 hours of migration, we found no significant differences in the number of transmigratory neutrophils between the media, Activin A, and Follistatin conditions indicating that Activin A and Follistatin possess no inherent neutrophil chemoattractant properties (Figure 3.4). Next, we used a triple lumen device consisting of three, non-vascularized, lumens where media was added to one of

the side lumens, neutrophils to the middle lumen, and *P. aeruginosa* and/or exogenous Activin A to the other side lumen and looked at neutrophil transmigration into the hydrogel after 18 hours. In the Activin A only condition, an average of 111.1 ± 89.6 neutrophils transmigrated into the hydrogel which was similar to the empty control where 181.2 ± 208.9 neutrophils were observed transmigrating (Figure 3.5A). As expected, when *P. aeruginosa* was added to the side lumen, we saw 774.6 ± 393.9 neutrophils transmigrate which was significantly more migration than the no *P. aeruginosa* conditions. When we added exogenous Activin A along with *P. aeruginosa*, however, we see a significant decrease in the number of transmigratory neutrophils, 449.1 ± 292.7. These results indicate that Activin A is not chemotactic, and reduces neutrophil migration.

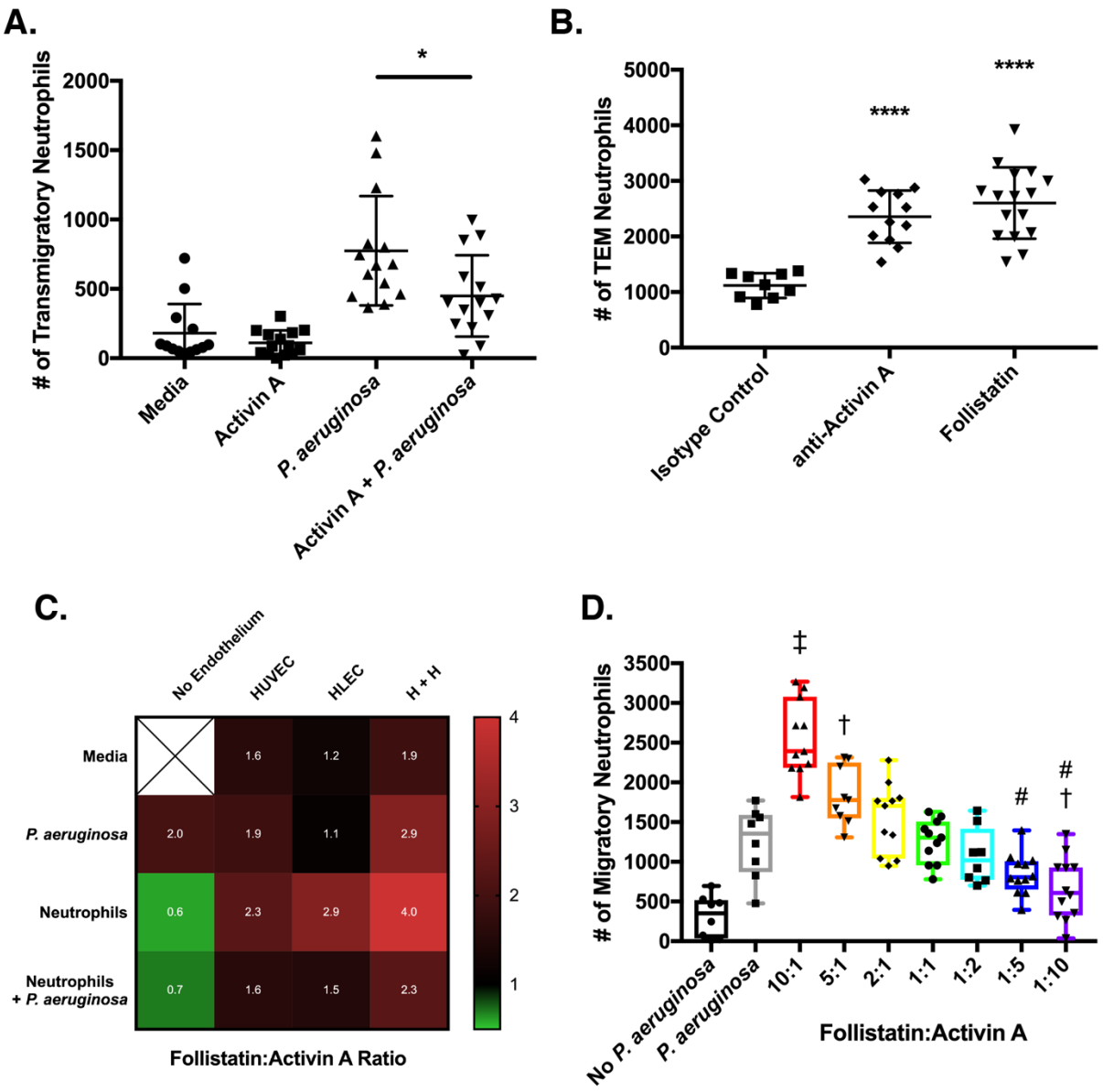

Figure 3.5: Follistatin/Activin A axis regulates neutrophil chemotaxis to *P. aeruginosa* - A) Quantification of neutrophil chemotaxis to *P. Aeruginosa* with and without exogenous Activin A added. * represents significance between conditions. B) Quantification of neutrophil TEM in HUVEC + HLEC condition with Activin A signaling blocked by either an anti-Activin A antibody, or Follistatin. * represents significance from the isotype control condition. C) Heatmap of the ratio of Follistatin:Activin A protein concentrations measured in all of the conditions. D) Quantification

of neutrophil chemotaxis to *P. Aeruginosa* with varying ratios of Follistatin:Activin A added. ‡ and † represent significance from *P. Aeruginosa* condition, # represents no significance from no *P. Aeruginosa* condition. Results were consistent across donors. * and † = $p < 0.05$, **** and ‡ = $p < 0.0001$.

To better understand how the Follistatin:Activin A axis impacts neutrophil chemotaxis during infection, we ran a series of Activin A blocking experiments. Using a triple lumen device with an empty media filled lumen, a HUVEC-lined central lumen filled with neutrophils, and an HLEC-lined lumen filled with *P. aeruginosa*, we added either anti-Activin A antibodies, isotype control antibodies, or Follistatin to the media and measured the number of TEM neutrophils after 18 hours. In the isotype control condition, we saw an average of 1118 ± 223.1 neutrophils migrate out of the endothelial lumen which was similar to the results seen in (Figure 3.5B). When Activin A was blocked either with anti-Activin A antibodies or Follistatin, we saw a significant increase in the number of TEM neutrophils, 2356 ± 472.1 and 2603 ± 642.9 respectively. These results indicate that the Follistatin:Activin A axis regulates neutrophil trafficking during infection with *P. aeruginosa.*

3.3.4 Follistatin:Activin A Ratio

Our ELISA experiments indicate that both Follistatin and Activin A are secreted at high amounts throughout our 18-hour experiments. However, when we look at the ratio of their measured concentrations, we notice that it fluctuates between 4:1 and 3:5, Follistatin:Activin A, depending on the condition (Figure 3.5C). To see what effect different Follistatin:Activin A ratios have on

neutrophil trafficking during infection, we ran a series of neutrophil migration experiments where exogenous Follistatin and Activin A, totaling 1 μg/mL of protein, was added to the system at Follistatin:Activin A ratios between 10:1 and 1:10. Using a triple lumen device consisting of all, non-endothelial lumens, with media in one of the side lumens, neutrophils in the middle lumen, and *P. aeruginosa* in the other side lumen, we quantified the number of transmigratory neutrophils after 18 hours (Figure 3.5D). At the two higher Follistatin:Activin A ratios, 10:1 and 5:1, we detected significantly more migratory neutrophils compared to the *P. aeruginosa* control (no exogenous protein). At the Follistatin:Activin A ratios between 2:1 and 1:5, we saw no significant differences in the number of migratory neutrophils compared to the *P. aeruginosa* control. However, at the lower Follistatin:Activin A ratios, 1:5 and 1:10, we saw no significant differences in the number of migratory neutrophils compared to the no *P. aeruginosa* control. These results agree with what we've previously seen and indicate that the ratio of extracellular Follistatin to Activin A can regulate neutrophil trafficking during infection.

3.4 Discussion

In this study, we developed an organotypic microfluidic model of neutrophil-lymphatic trafficking during infection with *P. aeruginosa* and investigated the effect of Follistatin and Activin A signaling on this process. One of the strengths of this model is the ability to mimic important aspects of infection including 3-dimensional lumen structures, blood and lymphatic vessels, and live bacteria [60][115]. Adding to the relevance of the model, all of the cell types used in the model were human primary in origin. With this model, we discovered both endothelial cell types,

blood and lymphatic, to be significant sources of Activin A and Follistatin in response to *P. aeruginosa* or the presence of neutrophils, though the lymphatic vessels produced substantially more of both. We also found that Activin A attenuates neutrophil chemotaxis to *P. aeruginosa*, but migration was rescued with the addition of exogenous Follistatin or anti-Activin A antibody.

Activin A and follistatin are intimately involved in human development, and are known to be expressed at high concentrations by the liver, gonads, and skin [116][117][118]. However, the identification of cell types responsive to inflammatory stimuli which release both activin A and follistatin into the circulation have remained undetermined. In this study, we found that the lymphatic endothelium is a major source of Activin A and Follistatin in response to *P. aeruginosa*. Follow-up work in mice or humans will be needed to confirm this *in vivo*.

Though we did not have the temporal resolution to identify when upregulation of Activin A or Follistatin began, we did identify that their expression is dynamic during infection with *P. aeruginosa,* which is consistent with what has been reported *in vivo* [119][120]. In our model, we were surprised to observe that both Activin A and Follistatin followed a bacterial-dependent upregulation over the 18-hour migration experiments, not just one or the other. Similar trends where both of these cytokines are concurrently upregulated have been reported in a number of conditions such as septicemia, cystic fibrosis, polycystic ovarian syndrome, rheumatoid arthritis, and chronic rhinosinusitis [119][121][122][123][124][125]. In most of these examples, the severity of the condition is directly correlated to the ratio of Follistatin:Activin A, though what effects it has on the immune system is cell and context-dependent. For example, studies have

reported that serum Activin A levels were elevated and correlated inversely with lung function and body mass index in adult cystic fibrosis patients [126]. Follistatin treatment of newborn β-ENaC mice, recognized for respiratory pathology mimicking human cystic fibrosis, decreased the airway activin A levels and distinguishing features of cystic fibrosis including airway neutrophilia, contrary to what we saw, and levels of mediators that regulate inflammation and chemotaxis. Opposite of the anti-inflammatory effects of Follistatin observed in cystic fibrosis, Follistatin blocking of autocrine Activin A signaling in human dendritic cells enhanced dendritic cell cytokine and chemokine production in response to CD40L stimulation but not TLR-4 ligation [127]. More work is clearly needed to better understand the context- and cell-dependent nature of the Follistatin/Activin axis on immune regulation.

While Follistatin and Activin A were found to be important for regulating neutrophil chemotaxis to *P. aeruginosa*, the results from our ELISA experiments as well as experiments with exogenous Activin A highlighted other import endothelial-derived cytokines. During our ELISA experiments, all of the acute inflammatory cytokines we tested, IL-1α, IL-6, and TNFα, followed a bacterial-dependent increase in expression, demonstrating that our model can recapitulate proper physiological responses to stimuli. Furthermore, these cytokines have been shown to be important for neutrophil priming, activation, lifespan/longevity [81][128][28]. Hence, the difference in overall neutrophil chemotaxis to *P. aeruginosa* without endothelial vessels, 774.6 transmigratory neutrophils **(Figure 4A)**, and with endothelial vessels, 2772 TEM neutrophils **(Figure 1E)**. Besides acute inflammatory cytokines, we also saw robust changes in protein expression for the putative neutrophil chemokines Fractalkine (CX3CL1), MIP-3α (CCL20), and

SDF-1 (CXCL12) which could have also contributed to the increased neutrophil TEM in the conditions which included lymphatic vessels. Though these cytokines were out of the scope of this paper, future work will use these as starting points for investigating neutrophil-lymphatic trafficking.

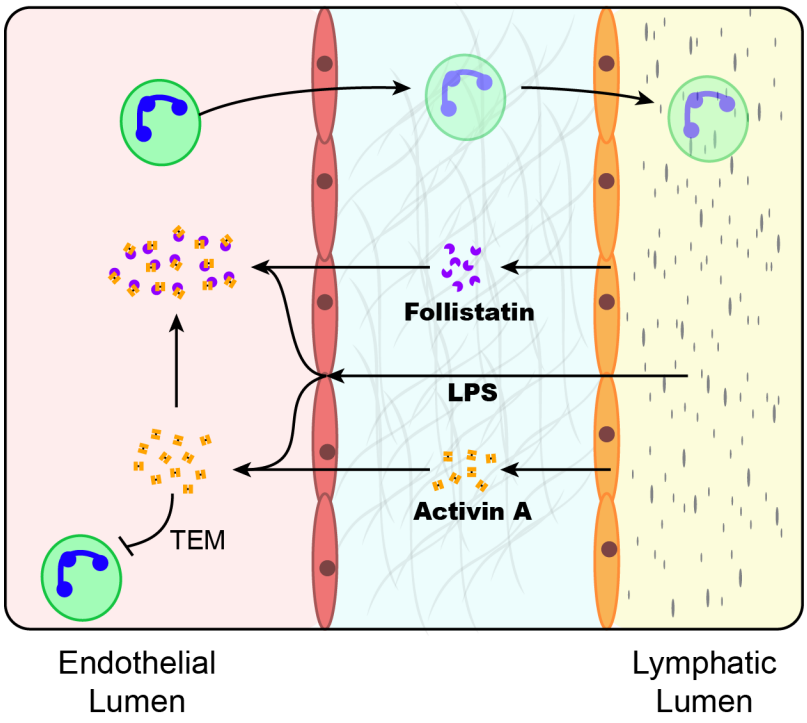

Figure 3.6: Summary of Follistatin/Activin A signaling in our infection model.

In summary, we identified the lymphatic endothelium to be a significant source of both Activin A and Follistatin. Activin A decreased neutrophil chemotaxis to *P. aeruginosa* whereas follistatin nullified this effect and allowed neutrophils to chemotax normally. Even though both cytokines were upregulated during infection with *P. aeruginosa* in our model, ultimately it was the Follistatin:Activin A ratio that modulated neutrophil chemotaxis as summarized in Figure 3.6. It

is apparent in the literature that Activin and Follistatin signaling are important to a lot of processes and conditions. As such, by better understanding this signaling mechanism, one could imagine manipulating serum or local concentrations of Activin A or Follistatin as a potential therapeutic treatment.

3.5 Acknowledgements

This work was supported in part by the State Economic Engagement & Development (SEED) Research Program, and the University of Wisconsin Carbone Cancer Center Support Grant P30 CA014520.

3.6 Continued Work – Follistatin/Activin A and Breast Cancer

Follistatin and Activin also show biological active roles in cancer. The overexpression of Activin A has been observed in several cancers including metastatic prostate cancer, lung cancer, stage 4 colorectal cancers, pancreatic cancers, and breast cancer [129][130][131][132]. Increased serum levels of Activin A has been reported in women with breast cancers and has been shown to be hyperactivated in breast cancer tumors [133][134]. This Activin A expression correlates inversely with survival and metastasis in advanced cancers. Furthermore, it has been shown that Activin A promotes breast cancer cell anchorage-independent growth, epithelial–mesenchymal transition, invasion, and angiogenesis [133]. Lastly, Activin A has been shown to induce a pro-tumorigenic phenotype in human mammary fibroblasts by facilitating tumor cell–tumor microenvironment interactions, leading to increased levels of cytokine production and cell motility [135]. Follistatin

has also been implicated in several cancers including breast cancer. Follistatin is expressed in normal breast tissue; however, its expression is decreased in breast cancer [136]. Additionally, overexpression of Follistatin *in vitro* has been found to significantly increase growth rate and reduce invasion in metastatic breast cancer cell lines. Clinically, higher follistatin levels are associated with lower-grade tumors and better survival, and conversely its expression level predicts increased metastasis and reduced overall survival [137].

While Follistatin and Activin A's role in breast cancer progression is well studied, their effects on tumor immune components are not. It is widely accepted that tumor endothelial cells are actively involved in helping the tumor escape immune surveillance. One of the mechanisms breast tumor endothelial cells (BTECs) use to accomplish this is by inhibiting leukocyte activation and excluding them from entering the tumor. Whether this pertains to neutrophils is still unknown. However, from our work with Follistatin/Activin signaling and neutrophil-lymphatic trafficking, it can be inferred that the dynamic expression of Follistatin and Activin A affects neutrophil infiltration of breast cancer tumors.

To test this hypothesis, we conducted an ELISA analysis of protein secretions from BTEC lumens and normal breast microvasculature endothelial cell (BMEC) lumens in parallel with neutrophil TEM migration experiments (Figure 3.6.1A). Using triple lumen, LumeNext devices consisting of a central endothelial vessel and two empty side lumens, along with the experimental setup outlined in Figure 3.6.1A. We found that there are significant differences in basal cytokine secretion between BMECs and BTECs (Figure 3.6.1B). Specifically, we found differences in IL-8

secretion, a potent neutrophil chemokine, and in Follistatin and Activin A secretions. In agreement with our previous results we found that both tumor and normal breast endothelial cells are a significant source of Follistatin and Activin A. Furthermore, we found that, in agreement with previous studies on Follistatin and Activin A levels in breast cancer, Activin A was significantly upregulated, and Follistatin was downregulated in BTEC vessels compared to BMEC vessels. This result indicates levels of Follistatin and Activin A are different in the tumor microenvironment compared to normal tissue.

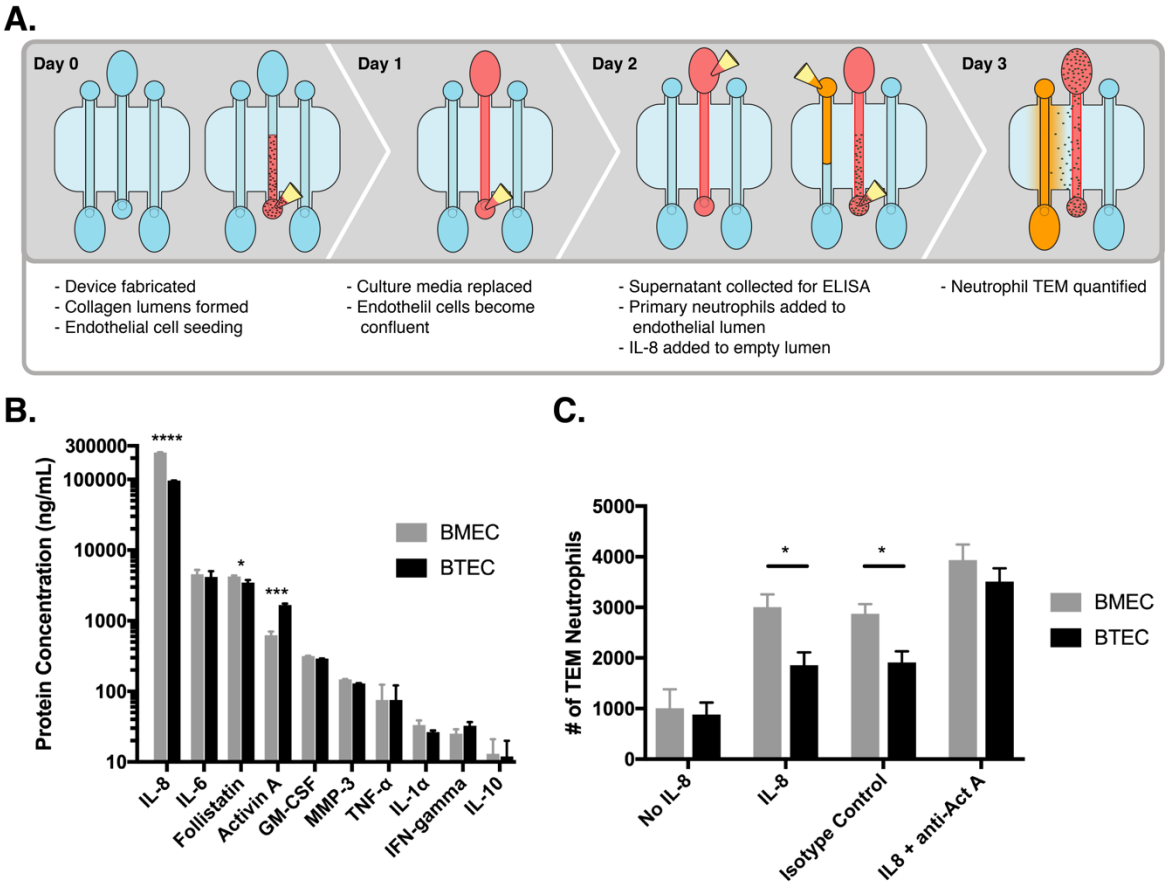

Figure 3.6.1: Activin/Follistatin axis involved in regulating neutrophil transendothelial migration (TEM) from breast tumor endothelial vessels. A) Schematic of the procedures utilized

for studying neutrophil TEM from BMEC (normal breast endothelial cells) and BTEC (breast tumor endothelial cells) lumens. B) Results from ELISA run on supernatant collected from confluent BMEC and BTEC vessels. C) Quantification of neutrophil TEM from BMEC and BTEC vessels in response to no IL-8, IL-8, IL-8 with an isotype control antibody, and IL-8 with an anti-Activin A antibody. Data was consistent across neutrophil donors. * = $p < 0.05$, *** = $p < 0.001$, **** = < 0.0001.

Next, to see if the Activin/Follistatin axis was being used by BTECs to regulate neutrophil transendothelial migration (TEM), we ran a series of neutrophil chemotaxis experiments where we used an anti-Activin A antibody to disrupt Activin/Follistatin signaling (Figure 3.6.1C). In this setting we found that there was a significant reduction in the number of TEM neutrophils out of BTEC Lumens compared to BMEC lumens in response to IL-8 indicating that indeed, BTECs exclude neutrophils from entering the tumor. However, when we blocked Activin A signaling, the number of TEM neutrophils significantly increases in both BTEC and BMEC conditions compared to the unblocked condition. Also, the relative difference in the number of TEM neutrophils between BMEC and BTEC lumens decreased suggesting that Activin A signaling is involved in escaping neutrophil surveillance in breast cancer.

In summary we found differences in expression of Follistatin and Activin A between normal and tumor associated endothelial vessels. We then correlated differences in Activin A secretion to changes in neutrophil TEM in response to an IL-8 gradient. Activin A was more highly expressed by tumor-associated lumens, and served to reduce neutrophil TEM and immune surveillance.

Furthermore, from the literature, Activin A acts to not only alter immune cell trafficking into the tumor, but it also increases epithelial-mesenchymal transitions, proliferation, motility, intravasation, and metastasis (Figure 3.6.2).

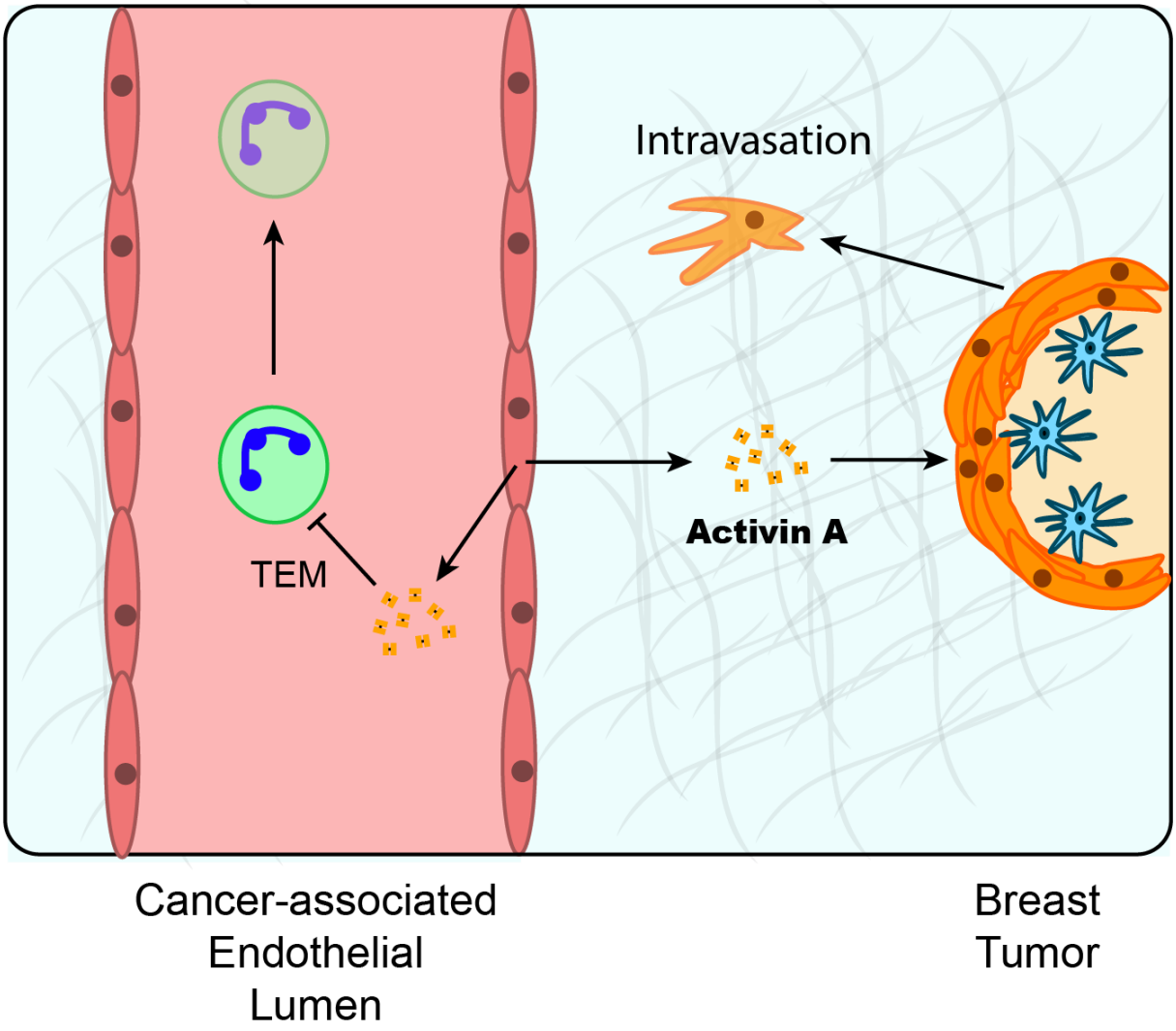

Figure 3.6.2: Diagram of our working model of Activin A signaling in breast cancer

Chapter 4:

Induced Pluripotent Stem Cells on a Chip: a Self-Contained, Accessible, Pipetteless iPSC Culturing and Differentiation Kit

This chapter has been adapted from the manuscript published in SLAS Technology in 2020 "Induced Pluripotent Stem Cells on a Chip: a Self-Contained, Accessible, Pipetteless iPSC Culturing and Differentiation Kit." **Patrick H. McMinn**, David J. Guckenberger, and David J. Beebe.

Abstract

Over the past decade, induced pluripotent stem cells (iPSCs) have become a major focus of stem cell and developmental biology research, offering researchers a clinically relevant source of cells that are amenable to genetic engineering approaches. Though stem cells are promising for both research and commercial endeavors, iPSC based assays require tedious protocols that include complex treatments, expensive reagents, and specialized equipment that limit their integration into academic curricula and cell biology research groups. Expanding on existing Kit-On-A-Lid-Assay (KOALA) technologies, we have developed a self-contained, injection-molded, pipetteless iPSC culture and differentiation platform that significantly reduces associated costs and labor of stem cell maintenance and differentiation. The KOALA "kit" offers users the full range of iPSC culture necessities, including cell cryopreservation, media exchanges, differentiation, endpoint analysis, and, a new capability, cell passaging. Using the KOALA kit, we were able to culture ~20,000 iPSCs per microchannel for at least 7 days, while maintaining stable expression of stemness markers (SSEA4, and Oct4) and normal iPSC phenotype. We also adapted protocols for differentiating iPSCs into neuroepithelial cells, cardiomyocytes, and definitive endodermal cells; a cell type from each germ layer of human development.

4.1 Introduction

iPSC microfluidic cell culture is not novel, however, current platforms still retain a level of complexity that discourages most biologists and teachers from using them. These microfluidic iPSC culture technologies require either the use of a syringe or peristaltic pumps, which cost thousands of US dollars, or consist of complex microfluidic microchannels that require specialized knowledge to fabricate and operate, or both [138]. These factors can make commercialization difficult [139][140][141][142][143][144]. The Kit-On-A-Lid-Assay (KOALA), is a technology capable of facilitating high-throughput, repeatable, low-media-volume cell culture assays, in a simple microfluidic straight channel without the use of liquid handling instruments or micropumps [145][146][147]. This platform is simple and cheap to fabricate, consisting of micromachined polystyrene (PS) microchannels, reagent-filled lids, and a cryopreservation apparatus. Once commercialized, KOALA iPSC culture and differentiation “kits”, consisting of all of the required pre-packaged cells, culture media, and reagents, could be sold to researchers and educators. Additionally, though these “kits” would be sold as a comprehensive stem cell culture systems, they would also be compatible with custom endpoints such as cell isolation and flow cytometry, drug screening, ELISA, etc.

Here we report the use of the Kit-On-A-Lid-Assay (KOALA) to develop an easy to use, self-contained iPSC culture and differentiation system. We take the first step in scaling up the production of KOALA components by using injection-molded microchannels. We also develop and characterize a passaging device that allows cells to be passaged from one KOALA microchannel to another microchannel at a user-defined split ratio.

4.2 Materials and Methods

4.2.1 Device Fabrication and Preparation

The lids, bases, and passaging adaptors were fabricated by CNC milling (PCNC 770, Tormach) with the lids having standard microscope slide dimensions (25 mm × 75 mm) (Figure 1A). Bases are comprised of three layers: an injection molded and milled post/channel polystyrene layer (Proto Labs) consisting of 12 sets of posts/channels, a pressure-sensitive adhesive layer (ARcare® 90106, Adhesives Research), and a glass slide layer. The adhesive tape, which covered the entirety of the base except for the microchannels, was cut using a Graphtec Craft Robo Pro plotter cutter. The post/channel layer consists of an inlet and an outlet post connected by a 5 mm long, 2 mm wide, and 0.8 mm deep channel. After assembly, the device is oxygen plasma treated using a Diener Electronic Femto Plasma Surface System.

Lids are milled from 2 mm polystyrene (#224-030-01, Goodfellow). Each lid contains a micro-well for each channel and a slot for absorbent pads. Each micro-well has an elliptical shape and is spaced to match the pattern of the input posts. The slot for the absorbent pad is 10 mm wide, 72 mm long, and 2 mm deep. The lids are assembled by placing two layers of cellulose fiber absorbent pad (#CFSP223000, Millipore Sigma) in the designated slot. Reagents or media are added to the wells before each use.

Cryopreservation lids consist of four components, three micro-milled polystyrene parts and a nylon membrane filter with a pore size of 0.2 µm (WHA7402009, Millipore Sigma)(Figure 1A).

Two of the polystyrene parts fit together to form a large media reservoir with 12 elliptical ports, spaced out to match the spacing of the inlet ports of the KOALA bases and a small media addition port. The nylon filter membrane is placed over the elliptical ports and the last polystyrene piece, consisting of 12 elliptical ports and a slot for an absorbent pad, is aligned on top. All three polystyrene layers are acetonitrile-bonded together to form a single device. Both bases, lids, and cryopreservation lids are UV disinfected for 30 minutes, prior to cell culture. For the cryopreservation lid, cells and cryopreservation reagent (10% DMSO) are added to the nylon filter-backed wells, a pressure-sensitive adhesive film (Scotch tape, 3M) is placed over each well, and the devices are placed in a -80 °C freezer and are frozen at a rate of 1 °C/min.

KOALA Passaging devices are milled from 4 mm polystyrene. Each passaging device contains 12 media reservoirs 3.5 mm deep with a half-ellipse shape to fit the inlet post of KOALA microchannels, 12 media transfer channels with 3.5 mm deep, half ellipse-shaped wells on each end, and a 10 mm wide, 72 mm long, and 3.5 mm deep slot containing 12, 3.5 mm tall wicking posts that align to the outlet posts of KOALA microchannels (Figure 4Ai). Devices are oxygen plasma-treated, the media reservoirs and non-functional surfaces are manually coated with a thin layer of paraffin wax to prevent liquid adsorption (#22-900-700, Thermo Fisher), and two layers of sterile absorbent pads are placed in the slot next to the wicking posts. Devices are UV disinfected for 30 minutes, prior to cell passaging, and are loaded with reagents prior to each application.

4.2.2 iPSC culture and maintenance

IMR90-4 human induced pluripotent stem cells (iPSCs)(WiCell Research Institute) were maintained in feeder-free conditions on Matrigel (#354230, BD Biosciences) in mTeSR1 (WiCell Research Institute) or TeSR-E8 media (#05990, STEMCELL Technologies) at 37 °C and 5% CO_2. All experiments were performed using iPSCs between passages 43–60. For routine iPSC maintenance, iPSCs were passaged with Versene (#15040066, Thermo Fisher) every 4–6 days. For passaging iPSCs for differentiation, iPSCs were dissociated with Versene (EDTA solution), and the number of live cells was quantified via a hemocytometer using trypan blue stain (#15250061, Thermo Fisher). iPSCs were cryopreserved in 10% DMSO in liquid nitrogen. iPSCs were then seeded with 10 µM Y27632 (ROCK inhibitor)(#1254, Tocris Bioscience) for the first 24 h to promote cell attachment. After 24 h, ROCK inhibitor was withdrawn and mTeSR1 or TeSR-E8 was added and replaced every 24 h. These iPSC culture conditions were used in both microdevices and 96-well plate, with the iPSCs in KOALA microchannels receiving 10 µL of media, and the iPSCs in the 96-well plate receiving 200 µL.

4.2.3 iPSC differentiation

IMR90-4 iPSCs were dissociated and plated overnight in mTeSR1 or TeSR-E8 medium at a density of 1.5 x 10^5 cells per square centimeter on Matrigel as described above. Neuroectoderm, cardiomyocyte and definitive endoderm differentiation protocols were adapted from published work [148][149][150]. Differentiation was verified using immunofluorescent staining, RT-qPCR and cell phenotype.

Neuroepithelial Differentiation: To generate neuroepithelial cells, cells were differentiated for 4 days in TeSR-E6 medium (#05946, STEMCELL Technologies).

Cardiomyocyte Differentiation: To generate cardiomyocytes, cells were first differentiated overnight in RPMI1640 (Thermo Fisher), B27 supplement minus insulin (#A1895601, Thermo Fisher) with 6 mM CHIR99021 (#72052, STEMCELL Technologies). The following day, the media was replaced with RPMI1640/B27 –insulin and the cells were allowed to recover for 24 h. On Day 2, RPMI1640/B27 minus insulin-containing 4 µM IWP4 (Inhibitor of Wnt 4 production)(# 5214, Tocris) was added. On Day 4, the cells were re-fed RPMI1640/B27.

Definitive Endoderm: To generate definitive endoderm, cells were differentiated for 1 day in TeSR-E6 medium containing 6 mM CHIR99021 and 100 ng/ml activin A (#338-AC, R&D Systems), followed by 3 days of activin A alone.

4.2.4 Image Acquisition and Analysis

Bright-field and fluorescent images were obtained using a Nikon Ti Eclipse inverted microscope. Images were processed using Nikon NIS-Elements. Images were analyzed using the open-source software ImageJ.

4.2.5 Viability Assay

Cells were washed with phosphate-buffered saline (PBS) and then stained for 15 minutes at 37 °C and 5% CO_2 with Calcein AM (C1340, Thermo Fisher), and Ethidium Homodimer-1 (E1169, Thermo Fisher). After 15 minutes, the cells were again washed with PBS and then imaged. Cells staining positive for ethidium homodimer were counted as dead cells whereas cells staining for only Calcein were considered living.

4.2.6 Immunofluorescence

To stain for pluripotency markers, we used the Pluripotent Stem Cell Immunocytochemistry Kit (OCT4, SSEA4) (#A25526, Thermo Fisher) with all reagents loaded into a KOALA lid. To immunostain for differentiation marker, cells were first washed with 1x phosphate-buffered saline (PBS) and were then fixed in 4% paraformaldehyde (#43368; Alfa Aesar) for 15 minutes. Following fixation, the cells were then permeabilized with 0.1% Triton X-100 (#807426; MP Biomedicals) for 30 min and then blocked with 1x PBS supplemented with 3% bovine serum albumin for 30 min. The following primary antibodies were used, Recombinant Anti-Islet 1 antibody [EP4182] (ab109517, Abcam), Anti-Cardiac Troponin T antibody [1C11] (ab8295, Abcam), Anti-PAX6 antibody (ab5790, Abcam), Anti-N Cadherin antibody (ab76057, Abcam), Anti-SOX17 antibody [OTI3B10] (ab84990, Abcam), and Recombinant Anti-FOXA2 antibody [EPR4466] (ab108422, Abcam). The following secondary antibodies were used, Alexa Fluor® 555 Donkey Anti-Rabbit (A-31572, Thermo Fisher), Alexa Fluor® 594 Donkey Anti-Rabbit (A-21207, Thermo Fisher), and Alexa Fluor® 488 Goat Anti-Mouse IgG3 (A-21151, Thermo Fisher). Fixed cells were incubated for 4 hours at 4°C with both the primary and secondary antibodies with three wash steps after each incubation.

4.2.7 RT-qPCR

Cells were lysed directly in KOALA microchannels, the cell lysate was pippetted from the devices and then their mRNA was isolated in 15 µL 10 mM Tris buffer using Dynabeads mRNA DIRECT Purification Kit (Invitrogen, #61011) per the manufacturer's instructions. Immediately following mRNA isolation, a reverse transcription reaction was run using iScript cDNA Synthesis kit (Bio-

Rad, #170-8891) and the resultant cDNA was pre-amplified with SsoAdvanced PreAmp Supermix (Bio-Rad, #172-5160) and primers from Integrated DNA Technologies (Supplementary Figure 2). Finally, qPCR reactions were run using iTaq Universal SYBR Green Supermix (Bio-Rad, #172-5121) in a Roche Lightcycler 480 II (Roche Molecular Systems) and a ΔΔCt analysis was run. *GAPDH* and *ACTB* were used for the relative expression analysis. No-template controls were run in parallel for all experiments.

4.2.8 Statistical analysis

Data were analyzed (Prism 7.0; GraphPad Software) using one-way ANOVA. Tukey's multiple comparison test with a 95% confidence interval was used when comparing different conditions.

4.3 Results

The technology consists of a KOALA base containing 12 microchannels and pairs of input/output posts (Figure 4.1A), a KOALA lid which contains 12 pre-filled wells and a slot for an absorbent pad (Figure 4.1B), and a KOALA cryopreservation lid consisting of 12 cryopreserved-cell-filled wells attached to a media reservoir, separated by a nylon filter (Figure 4.1C). The basis of this technology relies on capillary action to perfuse liquid from the KOALA lid, through the KOALA base, and into the absorbent pad of the lid, as well as liquid pinning inside the microchannel which causes a break in the liquid bridge between the base and the lid (Figure 4.1D) [145][146].

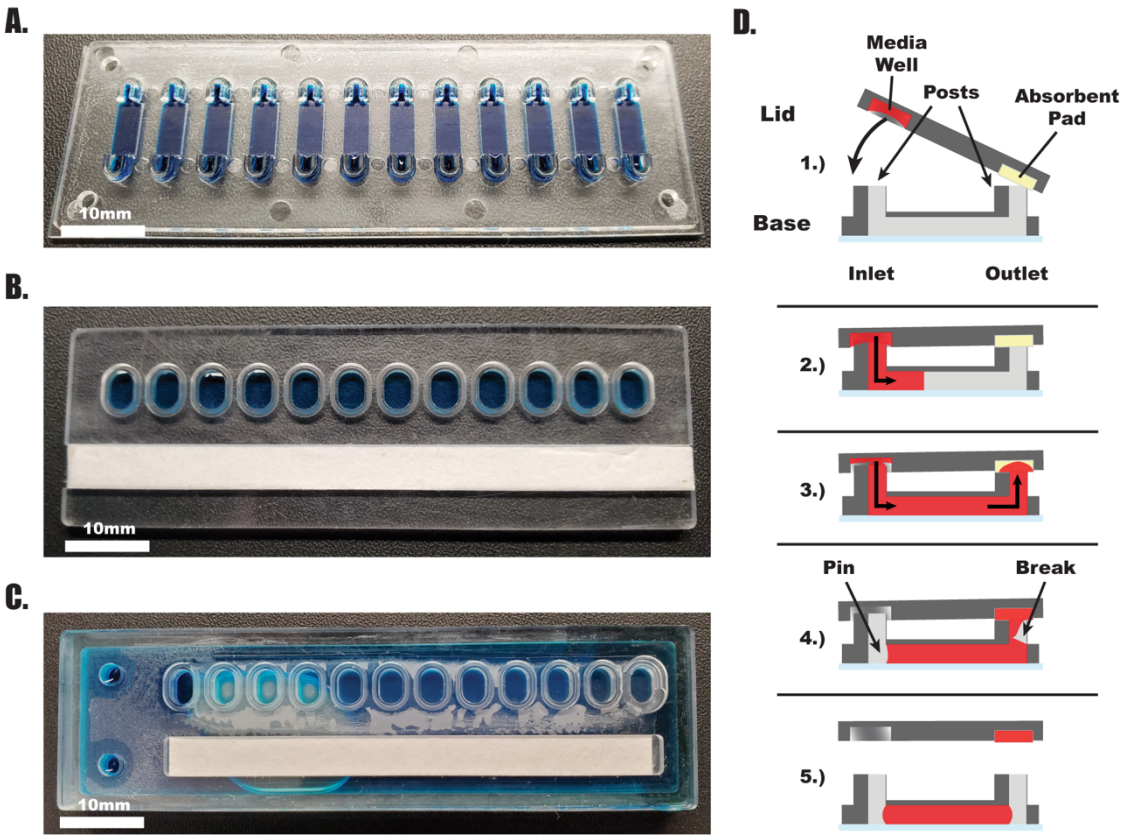

Figure 4.1: KOALA Components and Diagram – A) Koala Base B) KOALA Lid C) KOALA Cryopreservation Lid D) Diagram of how KOALA operates: 1 – KOALA Lid as placed on top of KOALA base so the media well and absorbent pad make contact with inlet and outlet posts. 2 – Media flows into microchannel from media well due to capillary action. 3 – Media continues to flow due to capillary action from absorbent pad. 4 – Once all of the media flows out of the lid, it will "pin" inside the microchannel which causes a "break" in contact between the fluid in the microchannel and the absorbent pad. 5 – The lid is removed and the new media/reagent remains in the KOALA base.

4.3.1 iPSC cell culture and cryopreservation using KOALA

Over time, stem cells cultured in less-than-optimal conditions will lose their pluripotency and self-renewal capabilities [151][152]. Fluctuations in mechanical stimuli, hypoxia, extracellular matrix composition, cell density, and small molecule signaling have all been shown to contribute to this loss [153][154][155][156]. Thus, we first sought to establish whether human iPSCs could be successfully cultured in KOALA microchannel devices.

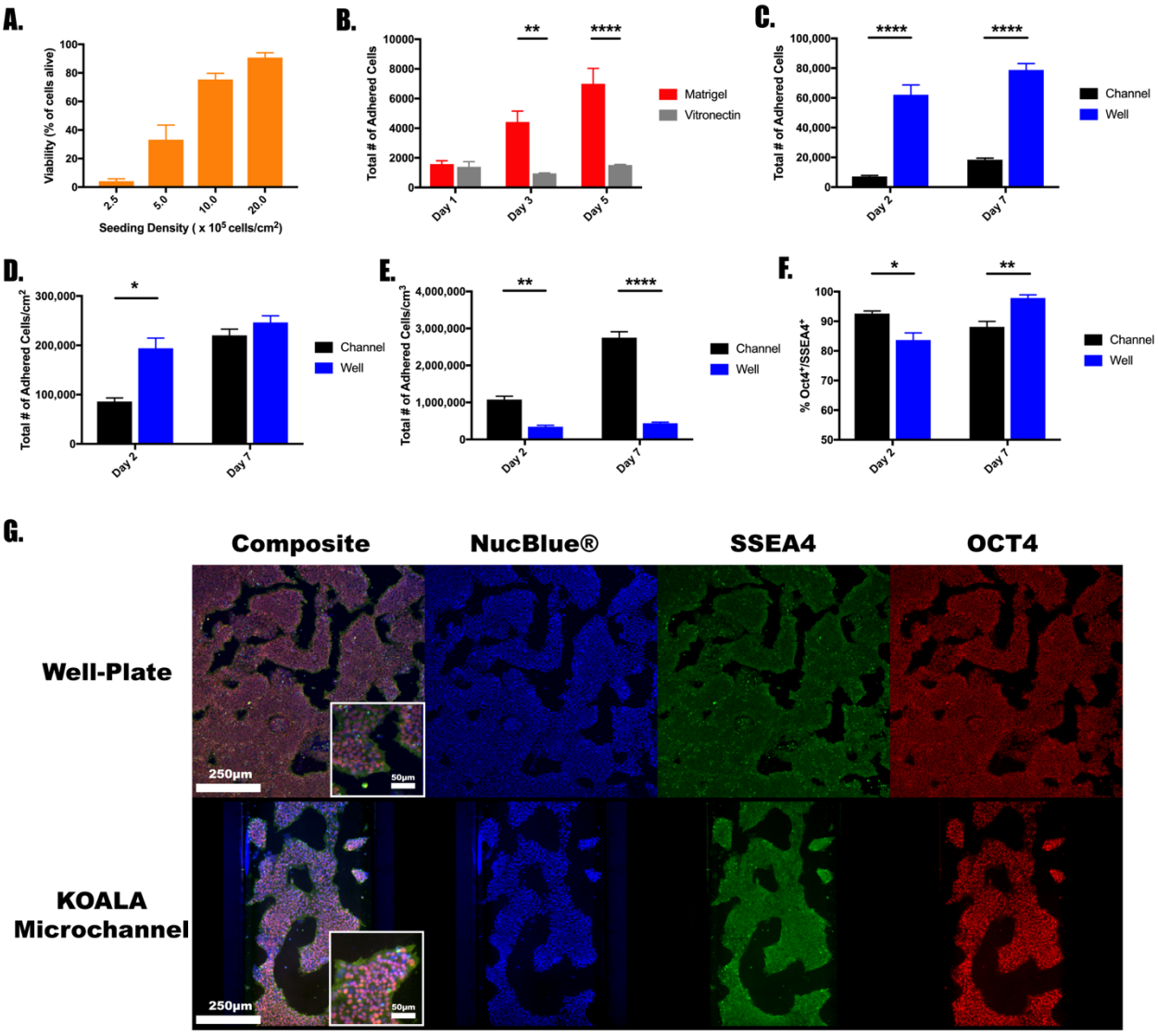

Figure 4.2: iPSC culture in KOALA vs. Well-Plate – A) Seeding densities versus viability rate in KOALA microchannels B) Total number of adhered iPSCs over time in Matrigel or Vitronectin-coated KOALA microchannels C) Total number of adhered iPSCs over time in KOALA microchannels vs. well-plates D) Total number of adhered iPSCs per culture area over time in KOALA microchannels vs. well-plates E) Total number of adhered iPSCs per culture volume over time in KOALA microchannels vs. well-plates F) Percent of *Oct4*$^+$/*SSEA4*$^+$ cells over time in KOALA microchannels vs. well-plates G) Fluorescent imaging of IMR90-4 iPSCs after two days in a well-plate (top) or KOALA microchannel (bottom) immunostained for SSEA4 (green), OCT4 (red), and a nuclear stain (blue). Graphs depict average +/- standard deviation across 12 technical and 3 biological replicates.. * = $p < 0.05$, ** = $p < 0.01$, **** = $p < 0.0001$

Stem cell culture requires optimal cell densities and extracellular matrix (ECM) composition. Using stem cell seeding densities ranging between 250,000 cells/cm^2 and 2,000,000 cells/cm^2, we added IMR90-4 iPSCs into Matrigel-coated KOALA microchannels and cultured them for two days, exchanging media twice a day. On the second day, we assessed the viability rate for each density and found that for the lower seeding densities (250,000 - 500,000 cells/cm^2) the average viability rates were less than 33.2%, suggesting these seeding densities were too low for stem cell culture in the KOALA microchannels (Figure 4.2A). The average viability rates for the higher seeding densities, 1,000,000 - 2,000,000 cells/cm^2, were 75.5%, and 90.8% respectively. Though the higher cell seeding densities correlated with better viability rates, the concentration of cells used to achieve a seeding density of 2,000,000 cells/cm^2 was already relatively high and larger

seeding densities would be impractical. Thus we used the 2,000,000 cells/cm^2 seeding density for our experiments.

Stem cell maintenance requires appropriate ECM conditions to support cellular self-renewal and to reduce spontaneous differentiation [157]. Classically, mouse embryonic fibroblasts and undefined basement membrane extracts such as Matrigel have been used for this purpose. Though Matrigel excels at facilitating stem cell culture, batch-to-batch variability has prompted researchers to turn to more defined ECM options [158]. In order to make the KOALA platform more appealing to cell biology researchers, we tested Vitronectin, a fully defined, protein substrate that has been shown to be amenable to stem cell culture [159]. To test vitronectin's performance as an ECM substrate in KOALA, we compared its performance to Matrigel and analyzed the number of IMR90-4 iPSCs over five days. After 24-hours of cell culture, there was no statistical difference between the number of adhered cells for both substrates with an average of 1581 ± 227 and 1399 ± 346 cells adhered to the Matrigel-coated and vitronectin-coated channels respectively (Figure 4.2B). However, at 72 and 120-hours, the number of stem cells adhered to the Matrigel-coated microchannel was 4418 ± 739 and 6994 ± 1045, triple and quintuple to that of the 24-hour measurement, while the number of cells adhered to the vitronectin-coated microchannels remained similar to the 24-hour measurement at 957 ± 28 and 1519 ± 36 respectively. For the vitronectin condition, we also noted a large number of cell detachment after each media change suggesting that the iPSCs might not have adhered to the vitronectin as strongly as to Matrigel, or might have died and detached from the substrate. These results indicated that vitronectin did not perform as well to the widely used Matrigel, and is not

a suitable culture substrate for iPSCs in the KOALA platform. Thus, we decided that Matrigel would be used for future experiments.

In order to evaluate whether iPSCs can be cultured using KOALA, we compared stem cell culture in KOALA to cell culture in a 96-well plate, a conventional method of culturing and differentiating stem cells. We first seeded IMR90-4 iPSCs into KOALA microchannels and a 96-well plate, then counted the number of adhered cells at day 2 and 7 (Figure 4.2C). At both timepoints, 2 and 7 days, the average number of adhered cells in the 96-well plate significantly outnumbered the number of cells adhered to the microchannels; 62084 ± 6608 and 78818 ± 4314 for the 96-well plate versus 7243 ± 606 and 18491 ± 1070 for the microchannels. Taking into account differences in surface area, we found that the average number of adhered cells per surface area was significantly higher in the 96-well plate (194014 ± 20651 cells/cm^2) compared to the microchannels (86226 ± 7219 cells/cm^2) for the day 2 timepoint but no differences remained by day 7 (246307 ± 13480 cells/cm^2 in the 96-well plates, 220134 ± 12735 cells/cm^2 in the microchannels). This result suggests that there is an equivalent cell culturing capacity between the two platforms (Figure 4.2D). One of the advantages of microfluidic cell culture platforms is their high cell number to volume ratios which enable stronger cell-cell signaling [160][161][162]. However, due to the high number of cells in a reduced volume, there is also an increased potential for nutrient depletion and cell starvation. When we look at the number of adhered cells per volume of media, we see a significant difference between the two culture platforms for both days with the cells per volume ratio for the KOALA microchannels being six times higher than for that of the 96-well plate (Figure 4.2E).

To test if the increased cell/volume ratio affected the cells' pluripotency, we immunostained IMR90-4 iPSCs in both KOALA microchannels and a 96-well plate after 2- and 7-days of culture and quantified the number of $SSEA4^+/Oct4^+$ cells, markers of pluripotency (Figure 4.2F,G). After two days of culture, the KOALA platform contained significantly more $SSEA4^+/Oct4^+$ cells compared to the 96-well plate (92.6% and 83.7%, respectively). By day 7, cells in both culture platforms reached confluency and the number of $SSEA4^+/Oct4^+$ cells in KOALA decreased to 88.2%, whereas the number of $SSEA4^+/Oct4^+$ cells in the 96-well plate increased to 97.9%. While this result indicates that prolonged cell culture in the KOALA platform could affect iPSCs' pluripotency, for shorter periods of cell culture, ≤ 7 days, a majority of iPSC's retain their pluripotent state.

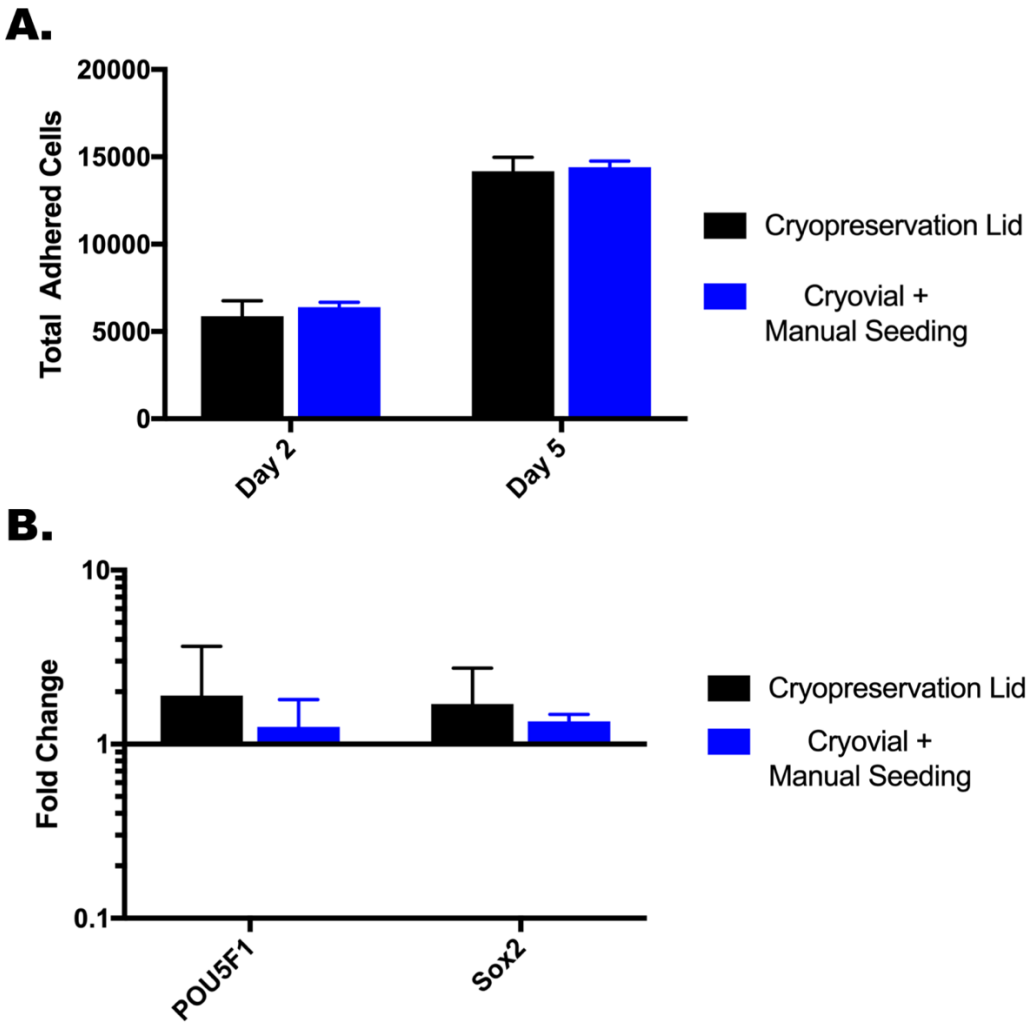

Figure 4.3: Cryopreservation lid Characterization – (A) Total adhered cells in KOALA microchannels on Day 2 and 5 after seeding using KOALA cryopreservation lid or by manual seeding with pipettman. No statistical significance was determined between the KOALA cryopreservation lid and manual seeding with pipettman. **(B)** RT-qPCR of iPSCs after 5-days of cell culture in a KOALA microchannel after seeding using KOALA cryopreservation lid or by manual seeding with pipettman. No statistical significance was determined between the KOALA cryopreservation lid and manual seeding with pipettman. Graphs depict average +/- standard deviation.

One of the main technological innovations of KOALA is the cryopreservation lid which allows cells to be frozen, thawed, and the cytotoxic cryopreservation media to be removed all within one microfluidic device. Briefly, the KOALA cryopreservation lid works similarly to a normal KOALA lid, however, there is an extra compartment attached to the back of the cryopreservation lid that is fluidically connected to the media wells by filter membrane. Cells are frozen in the wells of the cryopreservation lid, and when it is time to thaw and add them to microchannels, warm media is added to the rear compartment and the toxic cryopreservation reagents are dialyzed out. Once the cryopreservation reagents are diluted, the cells can be added to a KOALA microchannel the same a normal KOALA lid operates [145]. To test whether this device could be used to cryopreserve stem cells, we compared its performance to traditional cryopreservation methods. IMR90-4 iPSCs from the same culture were dissociated and frozen in media containing 10% DMSO in either a KOALA cryopreservation lid, 200,000 cells/well, or in a cryovial. Both samples were then thawed using previously described protocols and the cells were seeded, either with the KOALA cryopreservation lid or manually pipetted, into a Matrigel-coated KOALA microchannel [145]. Total adhered cells were then quantified and assayed for gene expression of pluripotency markers after 2- and 5-days of culture (Figure 4.3A). After both 2- and 5-days of cell culture post-thaw, there was no statistical difference in the total number of adhered cells. Additionally, there was no difference in the gene expression of *POU5F1* and *SOX2,* markers for pluripotency, for both cryopreservation methods after 5-days of culture in a KOALA microchannel after cell-seeding (Figure 4.3B). These results indicate that the KOALA cryopreservation lid performs as well as traditional iPSC cryopreservation methods in preserving viability and pluripotency.

4.3.2 Pipette-less cell passaging between microchannels

We have demonstrated that the KOALA cell culture platform is capable of maintaining iPSCs with no significant effects on the cells' pluripotency and self-renewal. We have also shown that KOALA performs comparably to traditional stem cell culture in a well-plate. However, for KOALA to be a self-contained platform, a method of passaging cells to other devices for basic cell maintenance or downstream applications is needed.

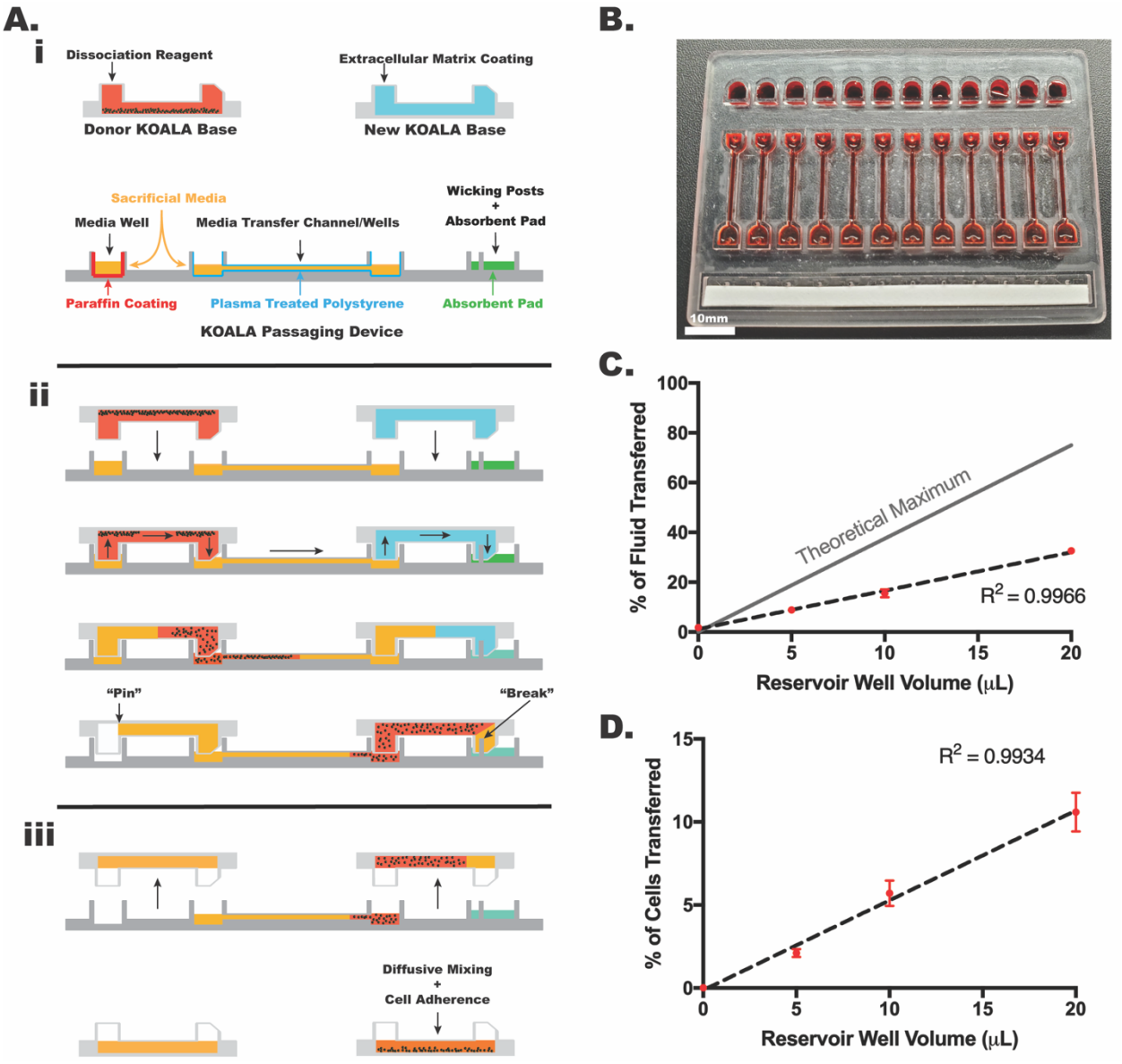

Figure 4.4: KOALA Passaging Device Characterization – A) Cartoon diagram of KOALA passaging device operation. B) Image of passaging device filled with media. C) Graph of percentage of media transferred to new KOALA microchannel as a function of media reservoir volume. Includes theoretical maximum (grey line). D) Percentage of cells transferred to new KOALA microchannel as a function of media reservoir volume. Graphs depict average +/- standard deviation.

We designed a microfluidic passaging device that allows cells to be transferred into new KOALA microchannels at a user-defined split ratio without the use of micropipettes (Figure 4.4A). The device, which is similar to a KOALA lid, consists of a micromachined polystyrene plate with 12 media reservoirs, 12 sets of transfer channels/wells, and 12 wicking posts (Figure 4.4B). The mechanism for how the device achieves unidirectional flow through both the donor KOALA base, the passaging device, and into the new KOALA base relies on differences in surface hydrophobicity/hydrophilicity, and capillary action. To prepare the passaging device, it was first oxygen-plasma treated to render the media transfer channels and wicking posts hydrophilic. Next, the media reservoirs and non-functional surfaces of the passaging device were coated with paraffin wax to make those surfaces hydrophobic. Lastly, an absorbent pad was placed next to the wicking initiation posts.

To operate the passaging device, a user-defined volume of cell-culture media is added to the media reservoirs, along with 15 µL sacrificial media to the transfer channels/wells (Figure 4.4Ai). Cell dissociation reagent is added to the donor KOALA device to detach adherent cells and ECM solution is added to the new KOALA device to coat it with the necessary ECM. Once the cells become detached, the donor KOALA device is placed upside down onto the passaging device so that the input posts of the donor KOALA device align and fit into the media reservoir wells and the output posts of the donor KOALA device fit into the wells of the transfer channels (Figure 4.4Aii). This action creates a continuous liquid interface from the media reservoirs, through the donor KOALA device, and into the transfer channels. Next the ECM-containing KOALA device is placed upside down onto the passaging device so that the input posts of the KOALA device fit

into the wells of the transfer channel, opposite to those of the donor KOALA device, and the output posts of the new KOALA device align with the wicking posts of the passaging device and fit into the output posts. Once fluidic contact is made between the transfer channels, the ECM-coated KOALA device, and to the wicking posts/absorbent pad, capillary action, driven by the absorbent pad, will induce laminar flow from the media reservoirs, through the donor KOALA device, into the transfer channels, through the new KOALA device, and into the absorbent pad. Flow of liquid will continue until all of the cell culture media in the media reservoir is transferred through the devices, after which, due to the design and dimensions of the KOALA posts, the media will "pin" in the input post of the donor KOALA device which will stop the flow of media into the ECM-coated KOALA device [145]. Once the liquid transfer is complete both KOALA devices can be separated from the passaging device (Figure 4.4Aiii). By adding more or less liquid to the media reservoirs of the passaging device initially, one can control the amount of fluid transferred from the donor device to the receiving device, and thus the split ratio. Additionally, homogenous cell seeding in the ECM-coated KOALA device can be achieved by placing the device, with the unadhered cells, immediately onto a rocker table to allow the cells to roll and adhere throughout the microchannel.

In order to confirm the function of the device, we first tested its liquid transfer capabilities using fluorescein dye. To do this, we filled donor KOALA devices with a solution of fluorescein and then used passaging devices filled with different volumes of water in the media reservoir wells to transfer the fluorescein to a new, water-filled KOALA device. By measuring fluorescein fluorescence in the water-filled KOALA device, we were able to calculate the percentage of fluid,

from the donor device, that was transferred to the new device (Figure 4.4C). We found a linear relationship between the initial media reservoir volume and the percent of liquid transferred to the new channel (R^2 = 0.9966). Additionally, the passaging device was consistent in its operation across all media reservoir volumes tested, demonstrating low standard deviations for each volume. Though the passaging device worked with high consistency, the percent of media transferred was significantly lower than the calculated theoretical maximum.

Next, we tested the passaging device with stem cells. We first seeded KOALA devices with IMR90-4 iPSCs and grew them to confluency. We then coated new KOALA microchannels with Matrigel. Using Versene and mechanical tapping of the device to detach and dissociate the iPSCs, we used the passaging device to transfer iPSCs to the Matrigel-coated channels at different volumes (Figure 4.4D). Though we achieved a similar level of consistency, low standard deviations across multiple replicates, across all of the media reservoir volumes used, the percentage of cells that were transferred to the new device did not compare directly with the results from the previous experiment. For the 20µL condition, 10.6% of the cells were transferred to the KOALA device compared to 32.6% of the fluorescein solution. As a whole, this data shows that the passaging device is capable of passaging iPSCs with high precision and consistency.

4.3.3 iPSC directed differentiation in microchannels

Stem cell differentiation is an important functionality for KOALA's broader application as a tool for stem cell research. To demonstrate this, we used directed differentiation to differentiate

IMR90-4 iPSCs into cell types from each germ layer; Neuroepithelium (ectoderm), cardiomyocytes (mesoderm), and definitive endoderm (endoderm).

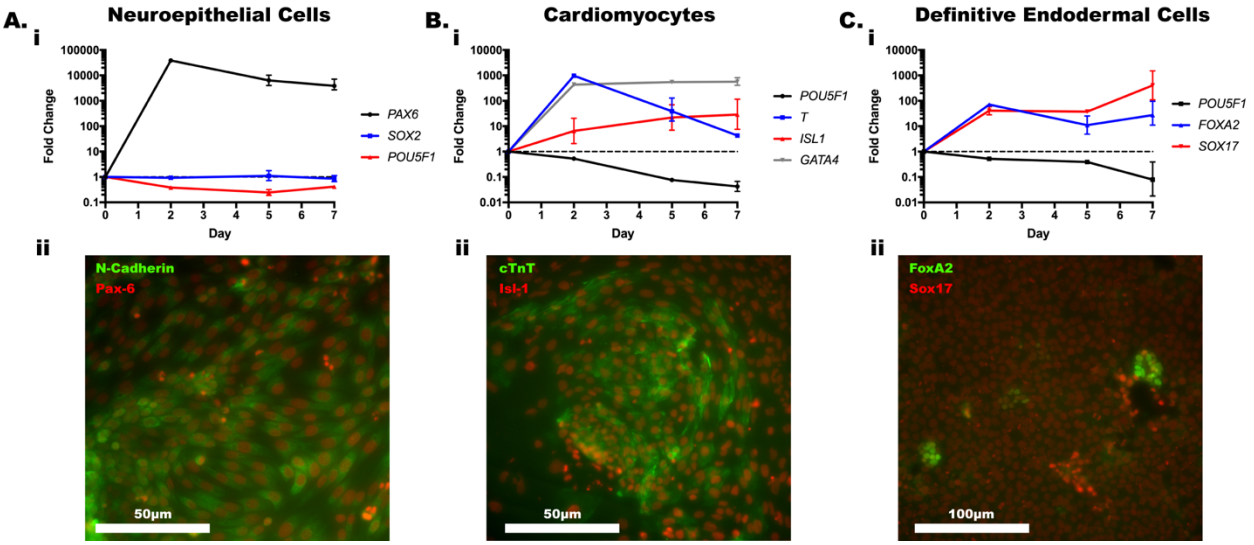

Figure 4.5: Directed Differentiation in KOALA – A) Neuroepithelial differentiation (i) RT-qPCR of 2-, 5-, and 7-day differentiated IMR90-4 iPSCs, assaying for *PAX6, SOX2,* and *POU5F1* (ii) Fluorescent image of differentiated IMR90-4 iPSCs, staining for Pax-6 (red), and N-cadherin (green). B) Cardiomyocyte differentiation (i) RT-qPCR of 2-, 5-, and 7-day differentiated IMR90-4 iPSCs, assaying for *T, ISL1, GATA4,* and *POU5F1* (ii) Fluorescent image of differentiated IMR90-4 iPSCs, staining for Isl-1 (red), and cTnT (green). C) Definitive endoderm differentiation (i) RT-qPCR of 2-, 5-, and 7-day differentiated IMR90-4 iPSCs, assaying for *FOXA2, SOX17,* and *POU5F1* (ii) Fluorescent image of differentiated IMR90-4 iPSCs, staining for SOX17 (red), and FoxA2 (green). Graphs depict average +/- standard deviation.

Neuroepithelial cells are the first precursor cells that form during the development of the nervous system [163]. Using a differentiation protocol developed by Lippmann et al. we were able to

differentiate IMR90-4 iPSCs into neuroepithelial cells after seven days of directed differentiation in KOALA [148]. IMR90-4 iPSCs were seeded into Matrigel-coated KOALA channels, allowed to adhere, and then cultured in mTeSR-E6 for seven days, according to the established protocol. Cells from KOALA channels were collected at 2-, 5-, and 7-days after the start of differentiation and the gene expression of *PAX6, SOX2* and *POU5F1* was quantified using a qPCR analysis. During neuroectoderm differentiation, gene expression of *PAX6* should increase, *SOX2* levels should remain stable, and *POU5F1* expression should decrease. After two days of differentiation, we observed a 38,838-fold increase in *PAX6*, a 0.93-fold reduction in *SOX2*, and a 0.38-fold reduction in *POU5F1* gene expression, consistent with the published protocol (Figure 4.5Ai). These gene expression levels remained consistent through seven days. Another indicator of neuroectoderm differentiation is the formation of polarized rosette structures which can be visualized by immunofluorescent staining for Pax-6 and N-cadherin [164]. After seven days of differentiation, we fixed and stained cells within KOALA microchannels for these two proteins. While we observed strong and consistent staining for both Pax6 and N-cadherin, additional markers of neuroepithelial cells, we were not able to detect robust rosettes structures (Figure 4.5Aii). However, the qPCR results and the strong Pax6 and N-cadherin staining indicate we were able to successfully differentiate iPSCs into neuroepithelial cells in the KOALA device, though further optimization will be needed to differentiate these cells down the neural lineage.

Cardiomyocytes are the muscle cells that make up cardiac muscle and are derived from the mesodermal germ layer [165]. Using a differentiation protocol developed by Lian et al. we were able to differentiate IMR90-4 iPSCs into cardiomyocytes cells after seven days of directed

differentiation in KOALA [149]. IMR90-4 iPSCs were seeded into Matrigel-coated KOALA channels, allowed to adhere, and then differentiated according to the established protocol. Cells from KOALA channels were collected at 2-, 5-, and 7-days after the start of differentiation and a qPCR analysis was run to measure gene expression of *POU5F1, T, ISL1,* and *GATA4* (Figure 4.5Bi). During cardiomyocyte differentiation, gene expression of *POU5F1* will steadily decrease, expression of *T* will initially increase significantly as the cells take on a mesoderm-like phenotype and then decrease as the cells differentiate further down the cardiomyocyte lineage, and expression of *ISL1* and *GATA4* will increase. As expected, gene expression of *POU5F1* decreased by 0.53-fold after two days of differentiation and continued to decrease further, *T* increased 975-fold by day two and then only by 4.27-fold by day seven, expression of *ISL1* steadily increased by 28.61-fold over seven days, and expression of *GATA4* increased by 434.53-fold after two days of differentiation and remained steady for the next five days. On the seventh day of differentiation, we also fixed and immunostained cells in KOALA microchannels for Isl1 and cTnT (cardiac troponin-T)(Figure 4.5Bii). We observed uniform staining for both proteins which further suggested successful cardiomyocyte differentiation. However, cardiomyocytes in 2D cell culture will begin rhythmically contracting without any external signals. While we only observed two instances of contracting cells (Supplemental Movie), combined with the qPCR and immunostaining results we conclude that we were able to successfully differentiate iPSCs into cardiomyocytes using the KOALA platform.

Lastly, the definitive endoderm gives rise to the epithelial lining of the digestive and respiratory tracts, and to the thyroid, thymus, lungs, liver, and pancreas [166][167]. Using a differentiation

protocol developed by Kunisada et al. we were able to differentiate IMR90-4 iPSCs into Definitive endodermal cells after seven days of directed differentiation in KOALA [150]. IMR90-4 iPSCs were seeded into Matrigel-coated KOALA channels, allowed to adhere, and then differentiated according to the established protocol. Cells from KOALA channels were collected at 2-, 5-, and 7-days after the start of differentiation and the expression of definitive endoderm markers *SOX17* and *FOXA2* as well as *POU5F1* was quantified using qPCR(Figure 4.5Ci). After seven days of differentiation, expression of *SOX17* and *FOXA2* increased 403.1- and 27.5-fold respectively, while *POU5F1* expression decreased 0.08-fold indicative of a definitive endoderm phenotype. We also Immunostained for Sox17 and FoxA2 and while Sox17 stained uniformly, we only found small patches of cells stained for FoxA2 (Figure 4.5Cii). According to the gene expression, *FOXA2* was less upregulated than *SOX17* and consequently, more time may have been needed for higher levels of FoxA2 protein to be translated. Also, compared to the neuroepithelial and cardiomyocyte differentiation protocols, the protocol followed here resulted in a much lower differentiation efficiency rate. Regardless, based on the high gene expression for *SOX17* and *FOXA2*, we successfully differentiated iPSCs into definitive endodermal cells using KOALA.

4.4 Discussion

iPSCs are sensitive cells whose pluripotency and self-renewal are highly influenced by slight changes in their environment. This poses technical and economic barriers for many researchers or educators who lack experience and setup. KOALA is a pipette-less, self-contained cell culture platform that can ameliorate some of the inconsistencies in stem cell culture, provide a more

customizable microenvironment, and can decrease overall costs. In this paper, we described the optimization and characterization of iPSC cell culture in the KOALA platform.

Most microfluidic cell culture devices fail to be adopted by the science community. Either their complexity or specific application or both limit their scalability and use by scientists. For example, work by Kamei et al. and Gómez-Sjöberg et al. both use intricate microfluidic designs, which include on- and off-chip valves and pumps, and small channel dimensions to culture stem cells [139][141]. While useful, their operation and fabrication require microfluidic expertise that most biology researchers and educators don't have. Even more straightforward microfluidic stem cell culture technologies like the ones used by Giobbe et al. and Liu et al. require expensive syringe/peristaltic pumps to operate, essentially making these stem cell culturing platforms an inaccessible option for most scientists. The KOALA platform contains everything a user needs to culture mammalian cells except for incubators and biosafety cabinets. The mechanism for which the KOALA technology is based off is simple to perform and requires very little expertise. Moreover, the components used for KOALA are simple in design and disposable.

In terms of cost, all of the KOALA components were fabricated using cheap materials. Besides the KOALA base, which was comprised of an injection molded PS piece, tape, and a glass slide, the rest of the KOALA components (i.e., lid, cryopreservation lid, and passaging device) were made from micromachined PS sheets. Without factoring in reagents and labor, the cost of a single KOALA kit, consisting of two KOALA bases, a cryopreservation lid, a passaging device, and 20 x KOALA lids, would be less than $10 USD. While stem cell culture reagents are generally expensive,

the lower reagent volumes used in KOALA could help reduce the cost per kit. Additionally, though the fabrication of KOALA components outlined in this paper required nontrivial amounts of labor, because of the low complexity of KOALA, we have taken steps towards commercialization and have begun to use injection molded devices. In this paper, all of the KOALA bases, which contain the microchannels, were injection-molded, a step very few microfluidic devices achieve. Once designs are finalized for the KOALA lids, cryopreservation lids, and passaging devices, we will have those components injection-molded as well, which will significantly reduce the associated labor costs.

We first optimized basic iPSC maintenance in KOALA microchannels and compared its performance to traditional well-plates, and found that there were no significant differences between the two methods in terms of cell viability, and cell density. Additionally, we noticed no microorganism contamination in either platform over 7 days. However, when comparing the number of cells expressing pluripotency markers between KOALA microchannels and well-plates, we noticed that the expression of these markers was higher after two days of culture in microchannels but then decreased by seven days, whereas the reverse was true for well-plates. The higher cell-to-fluid volume ratios at the micro-scale leads to a faster accumulation of secreted factors and could explain the higher numbers of cells expressing pluripotency markers in microchannels versus well-plates [161]. However, waste products and metabolites also accumulate faster and, when exposed to these detrimental factors for long enough, could also explain the decrease in pluripotency markers for iPSCs cultured in KOALA microchannels. By better understanding this dynamic in terms of stem cells, an improved design or protocol (e.g.

timing of media changes) could be implemented to help mitigate the detrimental effects observed here and could produce a more stable iPSC culture platform.

In this paper, we introduced a new component to KOALA that facilitates cell passaging between two devices at a user-defined split ratio. The device operates similarly to a KOALA a lid and was able to passage cells with a high level of precision between technical and biological replicates. One challenge with the device was the lower than expected cell passaging rate. When we inspected the passaging device after passaging cells, we observed clumps of cells remaining in the wells at the ends of the cell transfer channels indicating that either there is non-laminar flow through portions of these wells, or that the cells are adhering to the plasma-treated surface. Regardless of this loss of cells, the passaging device performed consistently and future use of the device will use media volumes which account for these differences. Cell passaging was the last cell culture procedure that KOALA was not able to perform. The addition of the passaging device to the KOALA platform means that all of the steps involved with iPSC culture can be carried out within the KOALA platform.

In terms of functionality, we demonstrated how KOALA can support directed differentiation of iPSCs down cell lineages from all three germ layers, neuroepithelium (ectoderm), cardiomyocytes (mesoderm), and definitive endoderm (endoderm). For all three directed differentiations, we were able to achieve robust gene expression of the proper lineage markers for each cell type. Additionally, we observed strong expression of lineage markers for all but definitive endodermal cells. However, even though we attained uniform immunostaining for the neuroepithelial and

cardiomyocyte differentiations, we failed to observe rosette-like structures or consistent spontaneous contractions; hallmarks for each cell type. This lack of phenotype could stem back from our previous point that while growth factors accumulate quicker in microdevices, so do metabolites, and these metabolites could be having a detrimental effect on the cells we were attempting to differentiate. The directed differentiation protocols used in this paper most likely didn't account for issues like this. Though they worked reasonably well in KOALA, future work will include optimization of differentiation protocols that take into account parameters that affect cell culture at the microscale.

Together this work demonstrates the utility of KOALA in stem cell research and opens up the possibility for the creation and commercialization of microfluidic stem cell differentiation kits. Compared to traditional stem cell culture, reagent volumes used in KOALA are significantly reduced, 10 µL reagent/media per microchannel versus 200 µL per well. Overall, KOALA iPSC differentiation kits could be a cheaper and easier alternative for researchers and educators to use.

Future work will focus on both improving differentiation protocols and expanding the functionality of the device. Most differentiation protocols are optimized for use in well-plates. From our results, we found that these protocols don't translate directly to microchannels, most likely due to the higher cell to volume ratio found in microfluidic devices. Additional work is needed to optimize differentiation protocols for KOALA microchannels. We have shown that KOALA is amenable to many endpoints such as most cell staining and imaging techniques, and

RNA/DNA isolation. One of the attractive applications of stem cells is their ability to be genetically altered and then differentiated down multiple cell lineages, allowing researchers to better model and study genetic diseases. Adding functionality for gene editing to KOALA could be a useful function for it to have.

4.5 Acknowledgements

This work was supported in part by the State Economic Engagement & Development (SEED) Research Program, and the University of Wisconsin Carbone Cancer Center Support Grant P30 CA014520.

Chapter 5:

Concluding Remarks and Future Work

This document focuses on the development of microscale organotypic models to interrogate co-culture effects during neutrophil trafficking, in particular neutrophil-endothelial and neutrophil-macrophage interactions during the onset and resolution phases of inflammation, neutrophil-lymphatic trafficking, as well as the development and design of a microscale iPSC culture and differentiation platform. The introduction (Chapter 1), describes the importance of understanding inflammation better and highlights areas of neutrophil biology that are understudied using human cells. This chapter also describes current issues with iPSC culture and differentiation platforms. Chapter 1 ends by suggesting that neutrophil trafficking and stem cell culture are two areas of research which could benefit from using microscale and/or organotypic *in vitro* models.

In Chapter 2, the development and characterization of a new microscale technology, termed LENS, is presented and is used to study endothelial priming of neutrophils. The focus of this chapter is to both emphasize the spatiotemporal control imparted by LENS, and to study the functional and phenotypic effects of neutrophil priming in human cells. In this chapter, it was demonstrated that neutrophil migration assays can be conducted in LENS, and that the technology could separate neutrophils based on their chemotactic ability, i.e. fast, slow, and non-migratory cells. LENS was then used to study the effects neutrophil-endothelial interactions have on neutrophil ROS production and chemotaxis to IL-8, concluding that neutrophil TEM is critical

for both functions, not just co-culture with endothelial cells. Furthermore, upregulation of genes associated with ROS production and cell adhesion were associated with neutrophil TEM.

In Chapter 3 a tissue model of infection was presented consisting of blood and lymphatic endothelia. This model was composed entirely of human primary cells and was used to investigate neutrophil trafficking to the lymphatics during *P. aeruginosa* infection. This chapter first revealed that lymphatic endothelial cells secreted factors that acted to increase neutrophil recruitment. Screening for cytokines and neutrophil chemokines, we found that Follistatin and Activin A were heavily secreted during infection and that they were primarily secreted by lymphatic endothelial cells, previously unknown. Next we showed that Activin A inhibited neutrophil chemotaxis to *P. aeruginosa* and that Follistatin neutralized Activin A's inhibition. Lastly, we demonstrated that the ratio of secreted Follistatin to Activin A significantly affected neutrophil chemotaxis in our model, suggesting a central role for Follistatin and Activin A for regulating neutrophil recruitment to the lymphatics during bacterial infection.

Lastly, in Chapter 4 the development and characterization of a human iPSC culture and differentiation platform is presented. The platform, based on the KOALA technology, is shown to be able to culture human iPSCs for at least seven days with comparable levels of pluripotency than to iPSCs cultured using a traditional well-plate. Another component to the KOALA technology, a pipetteless device for passaging cells between KOALA microchannels is described and shown to be capable of splitting iPSC at different ratios into new KOALA microchannels. In the last part of the Chapter 4, iPSCs are differentiated into neuroepithelial cells, definitive

endoderm cells, and cardiomyocytes using KOALA. This work demonstrates the utility of microscale iPSC culture platforms and opens up possibilities for expansion of KOALA's capabilities.

5.1 Neutrophil-macrophage interactions coordinate reverse migration

At the end of Chapter 2, preliminary work on modelling neutrophil RM was presented, demonstrating the heterogenous effects that macrophage polarity has on neutrophil chemotaxis in a 3D microscale model. M1 macrophages were shown to induce robust chemoattraction, whereas M2 macrophages were able stimulate neutrophils to migrate away from them. Furthermore, when an endothelium was placed distally from the neutrophils and macrophages, significantly more neutrophils migrated directionally towards the endothelium when the macrophages exhibited M2 polarity compared to an M1 state. From these results, our hypothesis that macrophage-neutrophil interactions coordinate neutrophil RM seems to hold true, however further experimentation needs to be done to confirm this. Firstly, the number of reverse migratory neutrophils increased when an endothelium was added to the system suggesting that neutrophil RM is not only dependent on neutrophil-macrophage interactions, but instead on neutrophil-macrophage-endothelial interactions. Secondly, now that we've shown our model can recapitulate neutrophil RM, future work will need to begin exploring the mechanism of how these cell-cell interactions direct RM, focusing on screening for secreted factors, and also looking at the impact juxtracrine signaling has on this process.

5.2 Evaluation of the role the Fol/Act axis plays in immune surveillance evasion in breast cancer.

At the end of Chapter 3, preliminary work on investigating Follistatin and Activin A's role in immune surveillance evasion by breast cancer was presented. We first screened for differences in secreted factors of interest between normal breast endothelial cell (BMEC) vessels and tumor associated endothelial cell (BTEC) vessels and found that IL-8, Follistatin, and Activin A were differentially expressed. We then found that, even though tumor-associated endotheliums are known to be leakier, more neutrophils migrated out of BMEC lumens compared to BTEC lumens in response to an IL-8 gradient. However, blocking Activin A signaling significantly increased the number of migratory neutrophils in both cases suggesting a possible role for the Follistatin/Activin axis in regulating leukocyte trafficking to tumors.

In the future we are considering investigating the dual nature of Activin signaling with regards to breast cancer in that it, according to our initial experiments, helps the tumor evade immune surveillance and, according to previous reports, is pro-metastatic. This could be accomplished in two parts. The first would entail completing the research into how Activin A, secreted by BTECs, influences neutrophil TEM. It would be interesting to include a tumor spheroid in this model, instead of an IL-8 gradient, to make these experiments more relevant. It would also be curious to explore how Activin signaling in this model impacts trafficking of other leukocytes, particularly NK cells and T cells. The second part would involve figuring out to what degree Activin signaling induces breast cancer metastasis.

Appendix A:

T Cell-Lymphatic Trafficking

Fluidic flow is an essential feature to human biology. Food and water flow through the digestive system, urine and reproductive materials are excreted out of the urogenital system, and mucus is whisked out of the respiratory system. However, flow is most commonly associated with the circulatory system. Blood flows throughout the body delivering nutrients, oxygen, and cells, and removes metabolites and waste from tissue. Besides transporting molecules and cells, flow within the circulatory system serves other important biological functions. First, flow is necessary for proper endothelial function and phenotype. It has been shown that endothelial cells exposed to shear stress are better aligned, have tighter cellular junctions, present different amounts of cell surface receptors on their luminal surface, and have altered secretion profiles to endothelial cells that were not exposed to fluidic shear [168][169]. Secondly, flow is necessary for proper immune cell trafficking. As immune cells are transported throughout the body they constantly come into contact with the vessel wall. Mediated by selectin-carbohydrate interactions, and integrins, leukocytes begin rolling along the apical side of the lumen and eventually firmly adhere. Fluidic shear reinforces these “catch bonds” and have been hypothesized as a means to spatiotemporally regulate leukocyte trafficking and inhibit unnecessary cell clumping and prevent arrest in low-flow areas, such as capillaries [170]. In order to properly study the importance of cell surface receptors in the circulatory system, fluidic shear must be incorporated.

T cell migration within and between peripheral tissues and the lymphatics is essential for proper functioning of the adaptive immune system [171]. The cellular and molecular mechanisms of T cell migration out of blood vessels is largely well characterized [112]. By contrast, less is known about T cell trafficking through the lymphatics. T cells leave the lymphatics via efferent vessels to return to blood circulation or through extravasation into peripheral tissue. One of the main reasons we know so little about T cell trans-lymphatic migration (TLM) is the due to the lack of microscale organotypic models of lymphatic vessels which incorporate hydrodynamic flow.

To study T cell TLM, and the surface receptors involved in orchestrating this event, we developed a lymphatic endothelial model which integrates gravity driven flow, called the FLumen platform. The micro-molded PDMS portion of the device consists of a LumeNext hydrogel chamber, a fluidic resistor in between the inlet port and the lumen chamber, and an outlet port which is only accessible from the bottom of the device (Figure A.1A). Additionally, the FLumen device has a 35 mm petri dish whose bottom surface has a thin layer of PDMS spun onto it, and a small 5 mm hole drilled into the center of it. The PDMS lumen portion is oxygen plasma bonded to the petri dish so that the outlet port of the lumen aligns with the hole in the bottom of the dish. This forms a continuous fluidic channel from the inside of the petri dish, into the inlet port, through the fluidic resistor, through the hydrogel lumen, out through the outlet port, and out through the bottom of the petri dish. To establish flow through the device, all one has to do is fabricate a hydrogel lumen, and then fill the petri dish with media (Figure A.1B,C). The length of the fluidic resistor, and the amount of media added to the petri dish control the overall flow rate (Figure

A.1D). To attain physiological flow rates and fluidic shear consistent with the lymphatics, we opted for a fluidic resistor of 35 mm in length and a fluid column height of 10 mm.

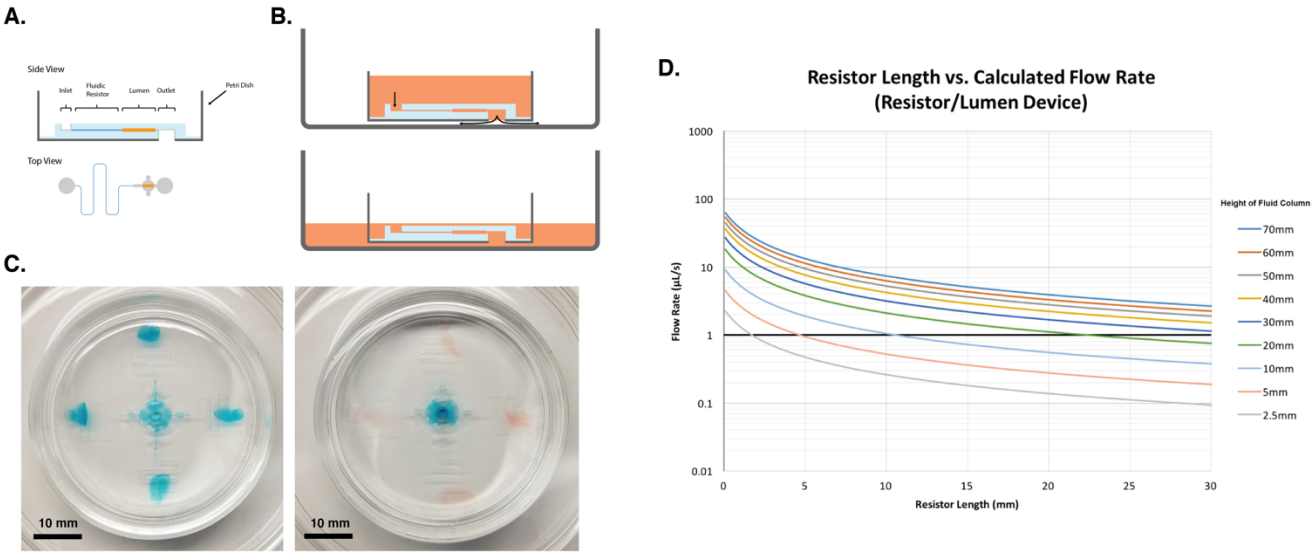

Figure A.1: Diagram of FLumen device – A) Schematic of the FLumen device. B) Side view diagraming the path of fluidic flow through the FLumen device. C) Top-down image of a FLumen device with blue, then red dyed solution flowing through the device. D) Mathematical model showing the flow rate of water through FLumen devices with different resistor lengths and pressure head heights.

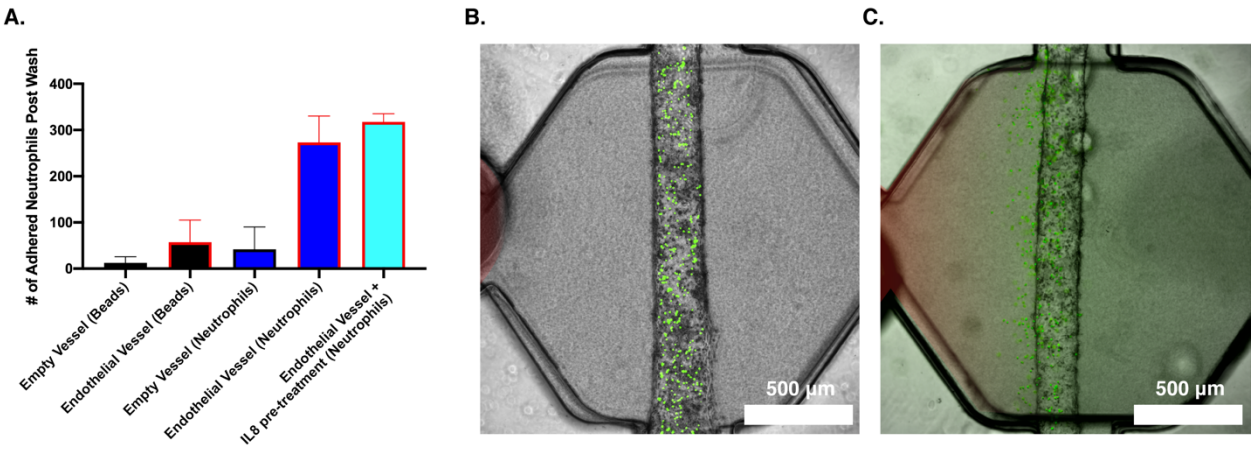

Figure A.2: Initial characterization of FLumen device with microbeads and neutrophils – A) Results of the number of microbeads or neutrophils adhered to the endothelial surface post wash. B) Image of neutrophils (green) adhered to endothelium, post wash. C) Adhered neutrophils (green) undergoing TEM in response to a perpendicular IL-8 gradient (red).

Though studying T cell-lymphatic interactions was the goal of the FLumen device, we did most of the characterization work using HUVEC lumens and either 20 µm polystyrene beads, or neutrophils (Figure A.2A). In our initial characterization of the device, we found that the flow rate was sufficient to allow neutrophils to roll and tightly adhere to the endothelial vessel, as well as wash away neutrophils that were not tightly bound (Figure A.2B). Furthermore, the device allowed for enough sensitivity for us to quantify the differences in neutrophil adhesion between an activated endothelium, and a non-activated one (Figure A.2A). Lastly, to test if we could model TEM, the next step in immune cell trafficking, we added neutrophils to a FLumen device, allowed them to tightly adhere to the endothelial lumen, washed away the non-adherent cells, removed the media from the 35 mm petri dish, stopping the flow, and then added IL-8 to one of the gel

loading ports. This established a gradient across the lumen towards which neutrophils migrated down, indicating we could model TEM, TLM (Figure A.2C).

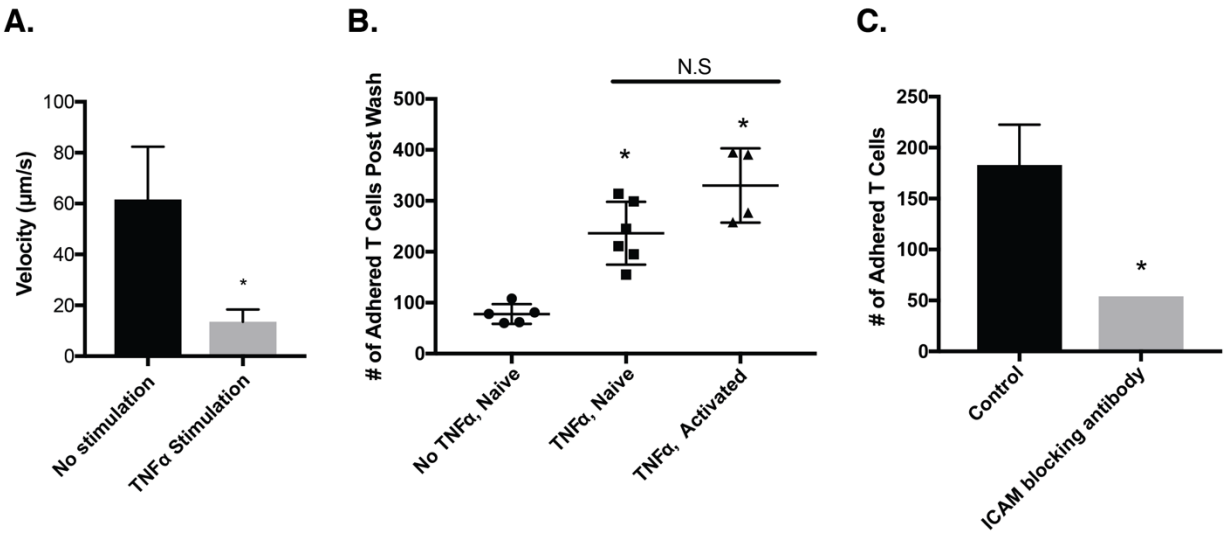

Figure A.3: T cell-lymphatic adhesion studies in FLumen device – A) Measured velocity of rolling T cells in HLEC lumens unstimulated, or stimulated with TNFα. B) Average number of adhered naïve or activated T Cells, post wash, to HLEC lumens stimulated with TNFα or unstimulated. C) Average number of adhered T Cells, post wash, to HLEC lumens stimulated with TNFα, and blocked with a control antibody or anti-ICAM antibody. * = $p < 0.05$.

Our modelling of T cell TLM in the FLumen platform began with analyzing T Cell rolling. In FLumen devices containing HLEC lumens, we perfused TNFα containing media, or just media through the lumens for 24 hours and then added calcein-AM stained T cells. We then captured T cell rolling using fluorescent microscopy and analyzed the average T cell rolling velocity for each condition. In the unstimulated vessels we observed an average rolling velocity of 62 μm/s, whereas in the

TNFα-stimulated vessel, the average rolling velocity was 14 μm/s (Figure A.3A). The significant reduction in average rolling velocity suggests there is increased presentation of adhesion molecules in the HLEC vessel after TNFα stimulation and that we can quantify the difference using FLumen. Next, we modelled the next step in T cell TLM, firm adhesion. Using unstimulated, and TNFα-stimulated HLEC vessel in FLumen devices, we flowed calcein-AM stained naïve and activated T cells through the device and then added equal washing volumes through all lumen conditions. We then quantified the number of adhered T cells using fluorescent microscopy and found significant differences in the number of firmly adhered T cells between the unstimulated and TNFα-stimulated vessels, but no significant differences in firm adhesion between the naïve and activated T cells (Figure A.3B). This results suggests that the activation state of T cells matters less to firm adhesion than the activation state of the HLEC vessel. Next, we ran ICAM blocking experiment to try to begin to determine the adhesion receptors needed for T cell adhesion during TLM. In TNFα-stimulated vessels in FLumen devices, we added either an anti-ICAM blocking antibody or an isotype control antibody and allowed the antibodies to bind for 12 hours. After incubation with the antibodies, we washed away unbound antibody and added naïve calcein-AM stained T cells to the lumens followed by a wash volume. We then quantified the number of adhered T cells using fluorescent microscopy and measured a significant reduction in firmly adhered T cells in the ICAM-blocked condition compared to the isotype control (Figure A.3C). This result implies ICAM is involved in T cell firm adhesion during T cell TLM.

During this project we developed an easy to use organotypic lumen model with gravity-driven flow called FLumen. The technology, requires no pump, is easy to add cells and reagents to, and

was shown here to be cable of studying immune cell-endothelial trafficking. The purpose of developing FLumen was to find a way to identify and study adhesion proteins located on the apical surface of lymphatic vessels involved in T cell TLM. While we were able to successfully measure the impact activation status of both the lymphatic endothelium and the T cells had on TLM, and while we were able to identify ICAM as an adhesion protein involved in T cell TLM, there are still a lot of experiments and proteins to target with experiments like the ones outlined above. Future work will first involve characterizing adhesion proteins involved in rolling adhesion and firm adhesion, and then will continue on to the study of T cell TLM and chemotaxis.

Appendix B:

High-throughput, Automated Lumen Model

The biggest limitation facing the widespread adoption of microscale organotypic models by researchers, drug companies, and hospitals is the lack of throughput. Current issues which limit the throughput of organotypic models include complicated designs which are hard to fabricate and manufacture, designs which require significant experience and time to operate, or models whose endpoints are limited. As we continue to encounter shortfalls with animal and 2D models, the need for high-throughput organotypic models increases. Here I developed a high-throughput organotypic lumen model adaptable to liquid handling robots and capable of automated hydrogel lumen fabrication, cell seeding, and media exchanges with minimal manual manipulation.

This technology, termed the high-throughput lumen (HTL) device, is composed of a milled 1536-well plate with metal rods inserted into the side of the plate (Figure B.1A,B). The milled features consist of narrow rectangle openings, machined into the sidewalls of the 1536-well plate (Figure B.1A). These rectangular openings extend from the top of the plate to 100 μm from the bottom of the well, and are milled into the well dividers which make up the plate's columns, allowing for a rod to be inserted into the side of the 1536-well plate and extend the entire length of the column of wells through the milled openings (Figure B.1B). To hold the metal rods in place during lumen fabrication, neodymian magnets are adhered to the bottom surface of the 1536-well plate (Figure B.1C). Once assembled, the HTL device can be inserted into a liquid handling robot such

as the Formulatrix Tempest, and hydrogel can be automatically added to the appropriate wells. Though there are openings connecting all the wells in a column, the dimensions of these openings are small enough to fluidically "pin" liquid within whatever well it is added to. Although, if two adjacent wells have liquid added, a fluidic connection will form between them, hence why sacrificial rows of empty wells are used to separate single lumen devices within a column, forming an air gap (Figure B.1D). After the hydrogel is added and allowed to polymerize, cell media can then be added to the two wells adjacent to the hydrogel-well, and the metal rods can be manually removed from the device with a single pulling motion, forming the hydrogel lumen structure (Figure B.1D). Cells, media, or reagents can then be added, via robot, into the lumens (Figure B.2A).

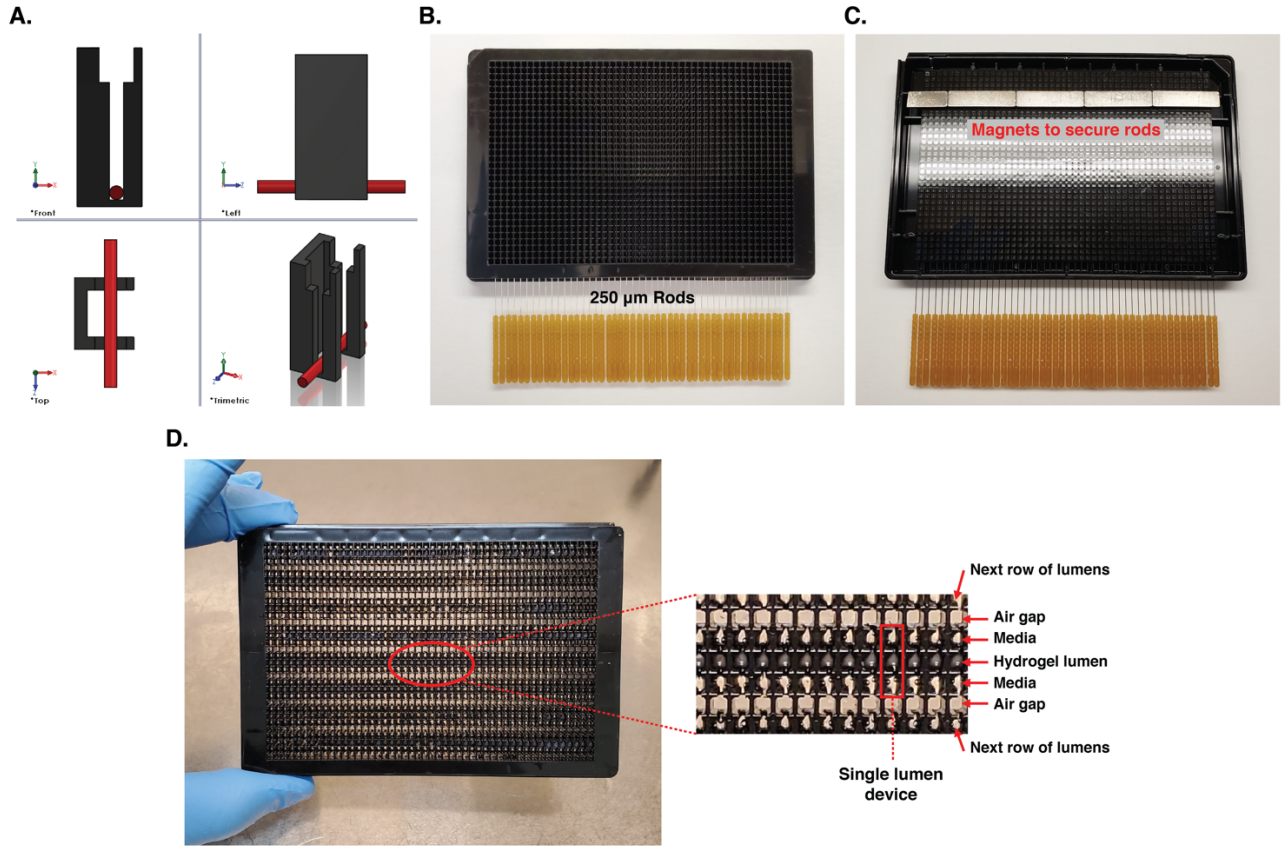

Figure B.1: HTL model diagram – A) 3D model of milled features and rod placement (red). B) Top view of 1536-well HTL plate with 250 μm rods inserted. C) Bottom view of 1536-well HTL plate with rods inserted and neodymian magnets to keep the metal rods in place during lumen fabrication. D) (Left) Top view of 1536-well HTL plate with fabricated hydrogel lumens. (Right) Magnified view of individual lumen components which consist of five wells: a single well for the hydrogel lumen, two media inlet/outlet wells on both sides of the lumen well, and two air-gap wells separating the row of lumens from the adjacent rows.

High-throughput, single lumen modules are the main focus of the HTL device; however, other lumen-based setups can be fabricated using the HTL technology. Perpendicular lumen setups are possible within the HTL device which consist of two single lumen units, perpendicular to each other on different planes in the Z-axis (Figure B.2B). Though this setup does require a larger footprint, and thus has a lower throughput than single lumen setups. Another element which can be engineered into the HTL device is a gradient generating well. This component consists of a single lumen module with an addition slot milled into the side wall of the hydrogel compartment. A lumen can be fabricated as previously described, and then reagent can be added to the side well, fluidically connecting the reagent and the hydrogel, and allowing a gradient to form across the lumen. Experiments using 10 kDa FITC-dextran were used to initially test this setup (Figure B.2C). We found that this stable produced relatively stable, short term gradients across the lumen chamber.

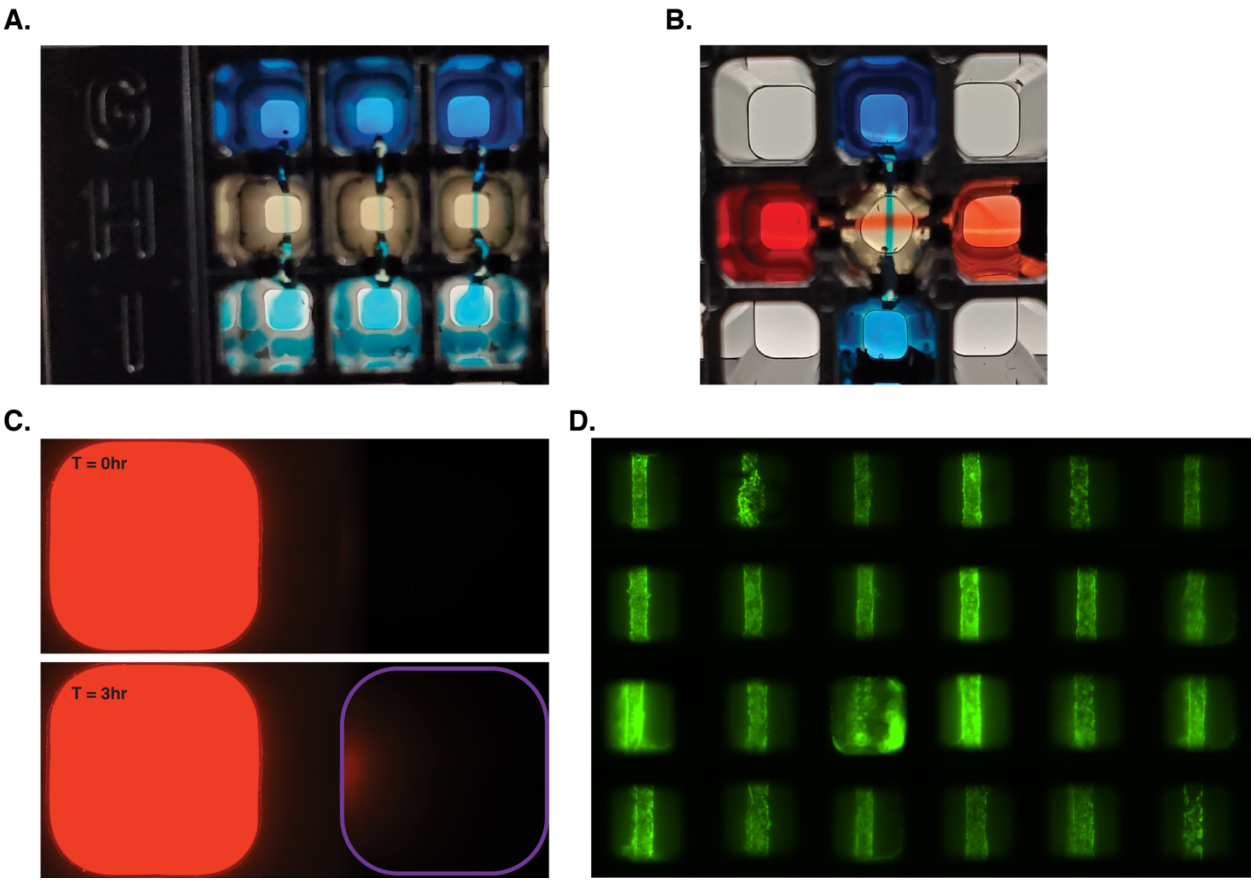

Figure B.2: HTL device capabilities – A) Close-up image of hydrogel lumens filled with a blue dye solution. B) Image of perpendicular lumens filled with either blue or red dye solutions. C) Images of 10 kDa dextran-Texas red diffusion from an adjacent well, into a hydrogel/lumen well at zero hours (top) and three hours (bottom). D) HUVEC lumens stained with calcein-AM in liquid-handling robot-fabricated collagen lumens.

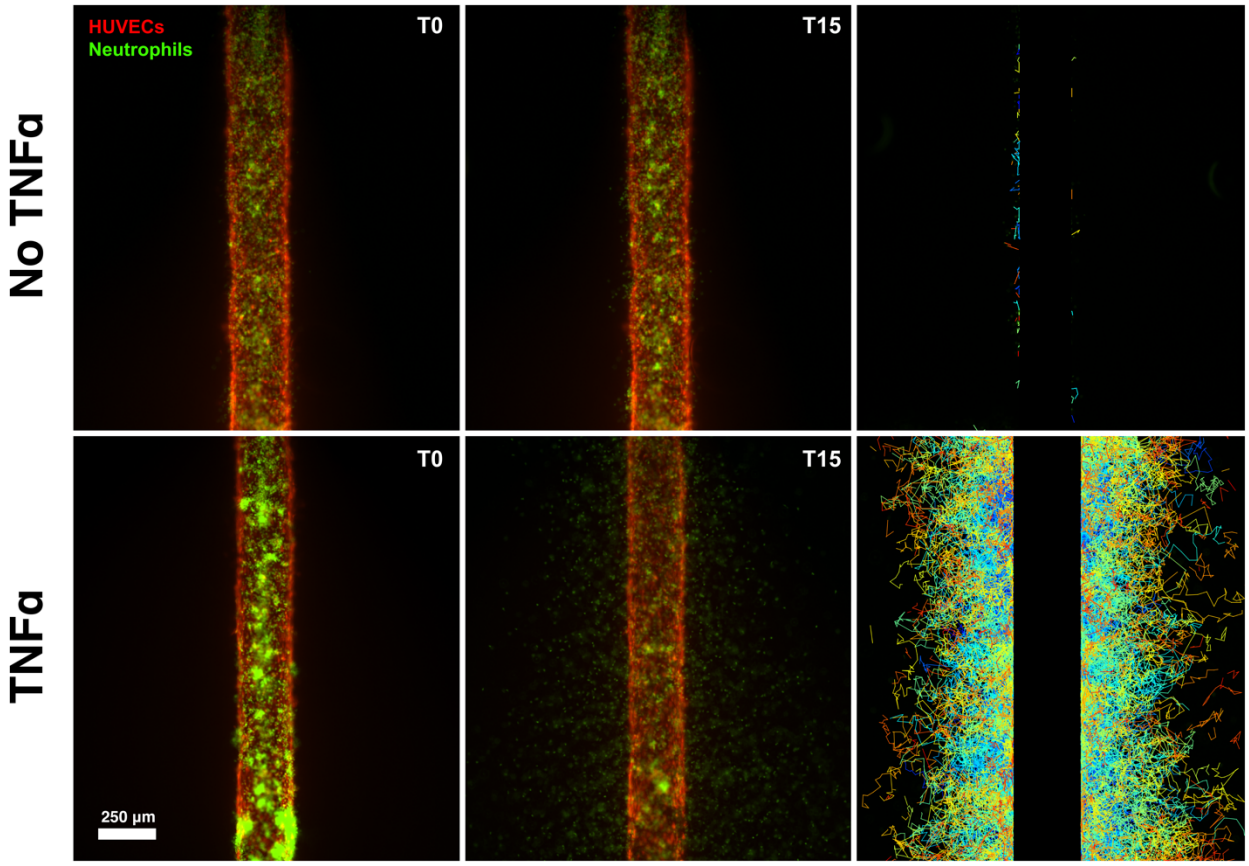

Figure B.3: Neutrophil TEM in HTL device – Neutrophil (green) TEM migration from HUVEC lumens (Red) in conditions with (bottom) or without (top) exogenous TNFα at 0-hours (Left) and 15-hours (middle). Cell migration was tracked using Trackmate (Right).

The intended purpose of the HTL device was to create a high-throughput system for making endothelial vessels for studying immune cell trafficking. In order to begin this research, we first established protocols for generating HUVEC lumens in an automated fashion. Using a Formulatrix Tempest liquid handling robot, we were able to generate HUVEC lumens with a ~92% success rate (Figure B.2D). To test if we could perform neutrophil trafficking experiments in the device, we manually added TNFα, a known neutrophil chemokine, and calcein-AM stained neutrophils

to HUVEC lumens and analyzed their TEM and migration (Figure B.3). As expected, we observed limited TEM in the no-TNFα, and robust neutrophil TEM in the TNFα condition, meaning the HTL platform is amenable to studying immune cell trafficking. We also wanted to use the HTL device to study endothelial vessel biology. One of the main characteristics we assay for when studying endothelial vessels is vessel permeability. To see if the if the HTL device could be used to measure vessel permeability we treated HUVEC vessels with TNFα, an acute phase protein, for 24 hours and then conducted a 10 kDa FITC-dextran diffusion experiment (Figure B.4). In the untreated vessels, we saw insignificant vessel permeability, whereas in the TNFα-treated vessels, we observed significant diffusion of the FITC-dextran indicating decreased barrier function, which was to be expected. This result indicates we are able to use the HTL device to study aspects of endothelial vessel biology.

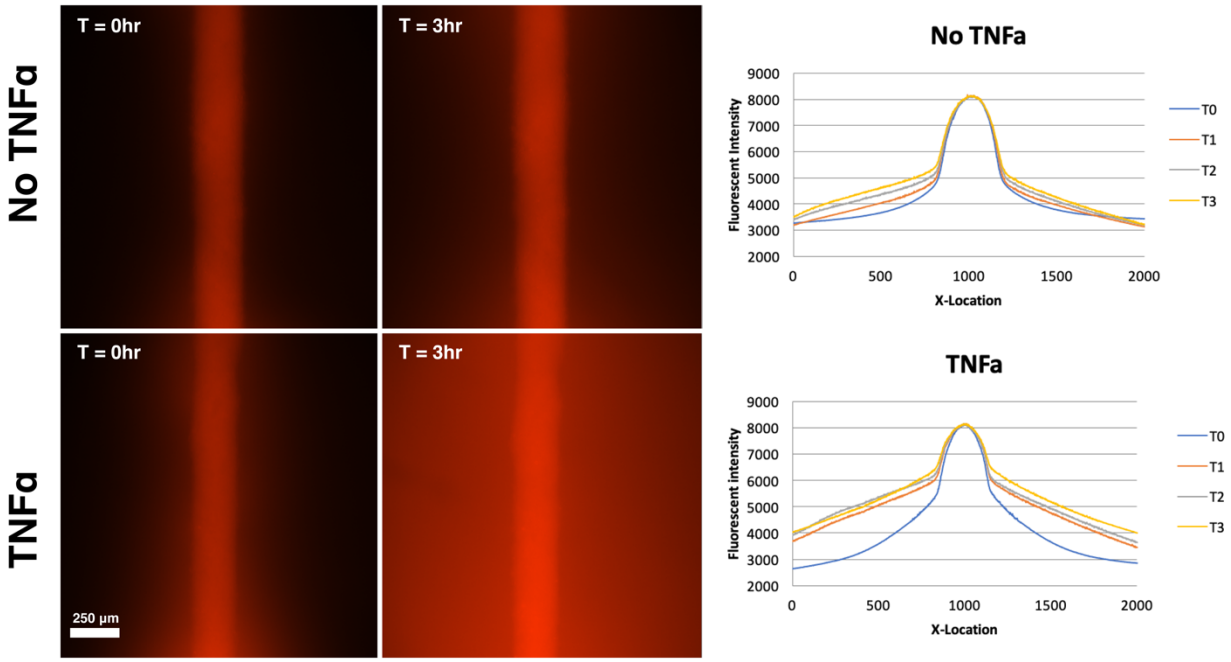

Figure B.4: Assaying vessel permeability in HTL device – 10 kDa dextran diffusion (red) from HUVEC lumens in conditions with (bottom) or without (top) exogenous TNFα at 0-hours (Left)

and 15-hours (middle). Average fluorescent intensity was measured as a function of position on the x-axis. (Right)

Neutrophil trafficking and vessel barrier function are just two of the potential applications for the HTL device. While one could use the HTL device to conduct a multitude of different assays for both of these subjects, the high-throughput and automated nature with which one can fabricate epithelial lumens opens up the possibility to conduct large drug screens in a physiologically relevant way. Either for drug discovery of personalized medicine, the HTL device is an exciting advance for high-throughput organotypic models.

Appendix C:

Tumor Slice Model and NK Cell Exhaustion

This chapter has been adapted from the manuscript published in Lab on a Chip in 2019 “Tumor-on a chip: a microfluidic model to study cell response to environmental gradienst.” Jose M. Ayuso, Maria Virumbrales-Munoz, **Patrick H. McMinn**, Shujah Rehman, Ismael Gomez, Mohammad R. Karim, Regan Trusttchel, Kari B. Wisinski, David J. Beebe, and Melissa C. Skala.

And the paper submitted to Nature Biomedical Engineering in 2020 “Microfluidic tumor on a chip model to evaluate the role of environmental pressure on NK cell exhaustion.” Jose M Ayuso, Shujah Rehman, Maria Virumbrales-Munoz, Patrick H McMinn, Peter Geiger, Cate Fitzgerald, Tiffany Heaster, Melissa C Skala, and David J Beebe

Solid tumors are highly heterogenous and plastic systems [172][173][174]. As solid tumors grow, the accelerated tumor metabolism, combined with an insufficient blood supply to support this uncontrolled metabolism, lead to nutrient exhaustion in the tumor microenvironment [175][176][177]. Simultaneously, cellular waste products accumulate in the innermost regions of the tumor. In this context, one of the main waste products is lactic acid, which also causes a pH drop at the core of the tumor [178][179]. Taken together, this evidence illustrates how tumor cells generate an extremely harsh microenvironment characterized by gradients of nutrient exhaustion, waste product accumulation, and pH across the solid tumor mass [180][181]. Thus, tumor cells located nearby blood vessels have enough nutrients to keep growing, forming a proliferative outer perimeter. Conversely, those cells located in the innermost region die of nutrient starvation, generating a necrotic core in the center of the tumor [182]. However, those cells located between the proliferative rim and the necrotic core play a critical role in tumor development. In this intermediate layer, tumor cells grow in an environment characterized by

moderate starvation, hypoxia and acidic pH.9 Interestingly, there are still some nutrients present, as well as metabolic intermediates, that were not consumed by the proliferative cells at the outer perimeter. Under these circumstances, tumor cells in the intermediate layer adapt their metabolic program to survive within the surrounding harsh microenvironment [183]. Cancer cells decrease or even completely stop their proliferation rate to minimize nutrient consumption, leading to a population of quiescent tumor cells. These quiescent cells activate alternative metabolic pathways and different survival responses (e.g., apoptosis resistance, starvation-induced DNA protection) [184][185][186][187]. Quiescent tumor cells can negatively influence patient outcome because they evade most chemotherapy agents (e.g., doxorubicin, paclitaxel, cisplatin), which only target proliferating cells, usually located at the rim of the tumor. In order to find effective therapies capable of targeting these heterogeneous cell populations in the solid tumor, in vitro models need to recapitulate the metabolic heterogeneity of the solid tumor microenvironment. Additionally, in order to analyze the effects different therapies have on different regions of the solid tumor, being able to selectively retrieve cells from different locations of a spheroid (e.g., proliferating periphery vs. quiescent layer) for downstream analysis is necessary.

Solid tumors also generate a suppressive environment that imposes an overwhelming burden on the immune system [188][189]. Nutrient depletion, waste product accumulation, hypoxia, and pH acidification severely compromise the capacity of effector immune cells such as T and NK cells to destroy cancer cells [190][191][192]. However, the specific molecular mechanisms driving immune suppression, as well as the capacity of immune cells to adapt to the suppressive

environment, are not completely understood. Therefore, here we developed a microfluidic tumor slice model that mimics the nutrient starvation and pH gradients, while allowing for selective retrieval of the cells for downstream analysis. We then used this *in vitro* tumor-on-a-chip platform to evaluate how NK cells respond to the tumor-induced suppressive environment.

During tumor development, cancer cell metabolism generates a complex microenvironment characterized by nutrient starvation, waste product accumulation and pH gradients. The combination of these environmental factors lead to the formation of different phenotypes across the tumor mass (Figure C.1A). A microfluidic tumor-on-a-chip model was fabricated to mimic this environment. The microdevice comprised a rectangular microchamber with a PDMS rod in one of the sides to generate a lumen perfused with culture medium (Figure C.1A,B). HCT-116 colon cancer cells were mixed with the collagen solution and injected into the microchamber through the hydrogel loading port. After collagen polymerization, the PDMS rod was removed, generating a lumen to perfuse culture medium. Given the large dimensions of the chamber (15 mm L × 10 mm W), two series of parallel small ports were included on the upper half of the microdevice on both sides of the lumen (Figure C.1A-C). In the absence of these ports and culture medium flow, nutrient diffusion from the hydrogel loading ports did not suffice to maintain the cells alive, leading to cell death across all the chamber. Diffusion ports ensured that nutrients diffused homogenously across the chamber, keeping those cells next to the lumen alive (Figure C.1C,D). Additionally, this approach avoided the use of external pumps to flow culture medium through the lumen, making the design more accessible to potential users.

Due to the dimensions of the device, and the rates of diffusion from the lumen being fixed, the easiest option to control the sizes of the proliferative, quiescent, and necrotic regions within the device was to evaluated the cell density required to stress the cells while keeping most of them alive. When cultured at 15 million cells per ml, HCT-116 cells generated a large necrotic region in the middle of the chamber with a well-defined live-dead transition zone (Figure C.1E). This result confirmed that a necrotic region could be generated in the microdevice. However, the necrotic region occupied a large area of the microdevice (>50%), limiting the area to ex- tract viable cells. Thus, the cell density was reduced by half in order to decrease cell mortality and increase the area of the chamber with live cells. When cultured at 7.5 million cells per ml, the necrotic region generated was smaller (<25%) and it almost disappeared at 5 million cells per ml, generating only a minor necrosis (<5%) (Figure C.1F).

One of the primary reasons for making the microchamber so large, comparatively, was to allow the user to separate the two halves of the PDMS microdevice, exposing the hydrogel, and be able to use a biopsy punch to retrieve cells after experiments for downstream analysis (Figure C.1G). We needed to ensure that the proliferative, quiescent, and necrotic regions were large enough to allow for a sufficient number of cells to be captured for qPCR analysis. The dimensions were also chosen to give the user room for error when acquiring samples.

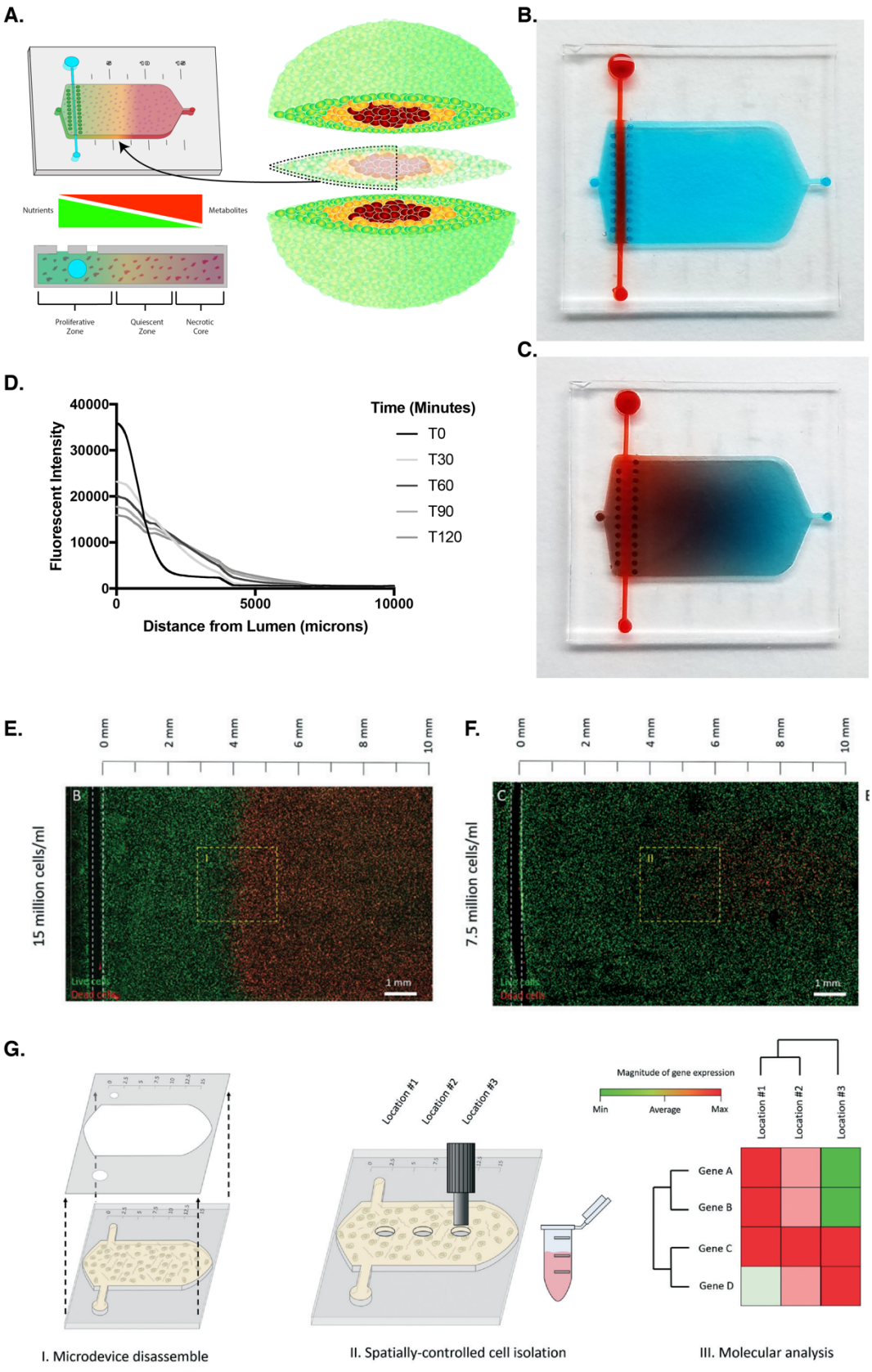
A.
Nutrients
Metabolites
Proliferative Zone
Quiescent Zone
Necrotic Core
B.
C.
D.
Fluorescent Intensity
40000
30000
20000
10000
0
0
5000
10000
Distance from Lumen (microns)
Time (Minutes)
T0
T30
T60
T90
T120
E.
0 mm
2 mm
4 mm
6 mm
8 mm
10 mm
15 million cells/ml
1 mm
F.
7.5 million cells/ml
1 mm
G.
Location #1
Location #2
Location #3
Magnitude of gene expression
Min
Average
Max
Gene A
Gene B
Gene C
Gene D
I. Microdevice disassemble
II. Spatially-controlled cell isolation
III. Molecular analysis

Figure C.1: Microdevice design and operation - A) Schematic representation of the different tumor phenotypes generated in a solid tumor due to nutrient starvation. B) Picture of the microdevice filled with a blue-colored 4mg/mL collagen-I gel and red-colored water in the lumen. C) Picture of the microdevice after 24 hours, showing diffusion of red-dyed water from the lumen. D) Quantification of 10 kDa FITC-dextran diffusion through device over two hours. E) HCT-116 at 15 million cells per ml. After 24 hours cell viability was evaluated staining viable and dead cells in green (calcein-AM) and red (propidium Iodide) respectively. The confocal image showed the formation of a large necrotic region with a dense necrotic area in the middle of the chamber. White dashed line indicates the lumen position. F) HCT-116 cells at 7.5 million cells per ml. The results showed the generation of a smaller necrotic region. G) Scheme illustrating the protocol to retrieve the cells from the device. Both halves are disassembled, exposing the collagen hydrogel and then hydrogel punches are isolated using a biopsy puncher.

Solid tumors generate a harsh microenvironment where environmental factors such as nutrient depletion, acidic pH, or waste product accumulation might affect the immune response (Figure C.2A). To study how the tumor microenvironment affects NK cell response and exhaustion, we used the tumor-on-a-chip microfluidic model consisting of a central microchamber seeded with breast cancer cells (i.e., MCF7) with/without NK cells (i.e., NK-92) embedded in a collagen hydrogel. After collagen polymerization, a PDMS rod located in the chamber flank was removed to generate a lumen through the collagen hydrogel. Then, the lumen was lined with endothelial cells (i.e. HUVECs) and perfused with culture media to generate a blood vessel surrogate that nourished the cells.

With this setup, we evaluated how NK cells respond to the tumor-induced suppressive environment. The results demonstrated that the suppressive environment created by the tumor gradually eroded NK cell cytotoxic capacity, leading to compromised NK cell surveillance and tumor tolerance (data not shown). Next, we studied whether NK cells, after removing them from the tumor-on-a-chip platform, would return to their naïve phenotype. In this context, NK cells exposed to the tumor-on-a-chip exhibited limited capacity to recover from this environmental pressure and markers of immune exhaustion persisted. These exposed NK cells also showed decreased migration and cytotoxic capacity, highlighting the impact, and potentially long-lasting effects of the tumor microenvironment on immune cells (data not shown).

To evaluate the potential of the platform to study tumor immunotherapy, we used NK-92 cells, which are known for retaining killing capacity both *in vitro* and *in vivo and* have been extensively tested in clinical trials. NK-92 cells were perfused through the blood vessel surrogate to evaluate their migration through the collagen hydrogel (Figure C.2C,D). NK-92 cells penetrated through the collagen hydrogel and after 3 days, NK-92 cells were observed in the distal area interacting with MCF7 cells (Figure C.2E-G). However, NK cell density across the chamber was not homogenous, generating a gradient of NK cell density with most of the NK-92 cells concentrated in the proximal area and rapidly decreasing below 50% density at 2 mm (Figure C.2H).

In summary, we developed and characterized a tumor slice model that was able to recapitulate the complex nutrient, waste product, and pH gradients observed within solid tumors. With the correct density of tumor cells, we observed the formation of proliferative, quiescent and necrotic

regions within the device. Cells isolated from these different regions produced significantly different transcriptional profiles (data not shown) indicating the presence of a spectrum of phenotypically different tumor cells within the same solid tumor. We then used this model to study NK cell behavior within solid tumors and identified exhausted NK cell populations which did not recover after removal from the tumor. We also tested the efficacy of NK-92 cells as immunotherapy agent and found that while the NK-92 cells displayed poor TEM, their tumor-killing ability was robust (data not shown). Future work with the tumor-slice device will continue to explore and study immunotherapies towards solid tumors.

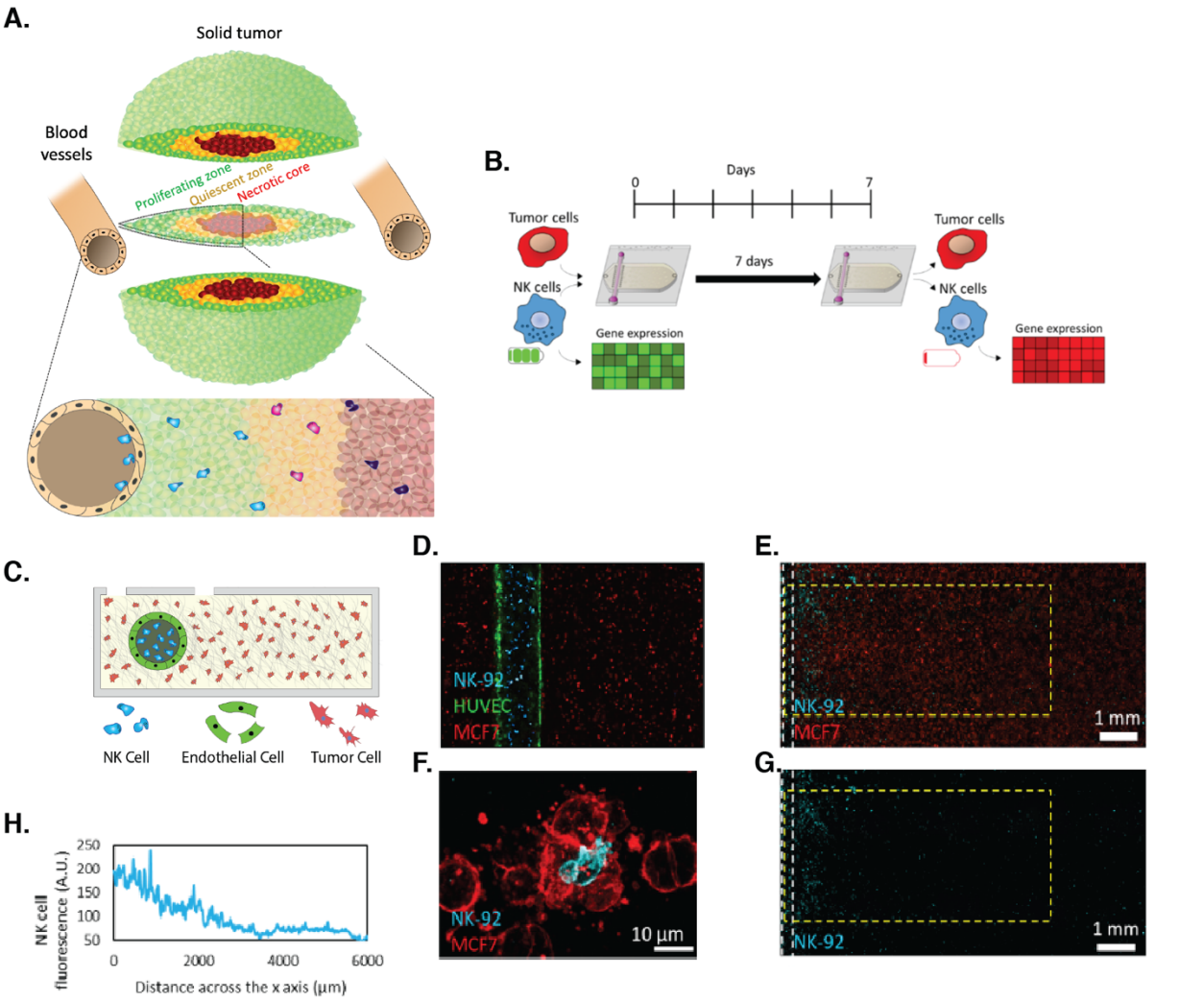

Figure C.2: Tumor-on-a-chip. A) Schematic representation of the different tumor phenotypes generated in a solid tumor due to nutrient starvation. B) Schematic representation of an experiment measuring immune exhaustion. NK cells and MCF7 cells were cocultured in a 1:3 ratio (0.5 million cells/ 1 ml: 1.5 million cells/ 1 ml) for 7 days. After 7 days, the NK cells were isolated and gene expression and other characteristics were measured. C) Scheme of the tumor slice microdevice showing the central microchamber with endothelial cells surrounding the lumen, NK cells embedded in the lumen, and tumor cells embedded in the central collagen chamber. D) Confocal image showing the dispersal of cells in the tumor-on-chip device. MCF7's (in red) are

embedded in the collagen gel, while NK-92 cells (in blue) and HUVEC cells (in green) are embedded in the lumen. E) This confocal image shows NK-92 cells (in blue) migrating across the chamber and MCF7 cells (in red). F) Confocal image representing a NK-92 engaging with an MCF7. G) This confocal image highlights the profusement of NK cells out of the lumen and into the chamber. H) Quantification of NK92 migration across the x-axis measured by NK cell fluorescence.

References

(1) Medzhitov, R. Origin and Physiological Roles of Inflammation. *Nature* **2008**, *454* (7203), 428–435. https://doi.org/10.1038/nature07201.

(2) Rankin, J. A. Biological Mediators of Acute Inflammation. *AACN Adv. Crit. Care* **2004**, *15* (1), 3–17.

(3) Landskron, G.; De La Fuente, M.; Thuwajit, P.; Thuwajit, C.; Hermoso, M. A. Chronic Inflammation and Cytokines in the Tumor Microenvironment. *J. Immunol. Res.* **2014**, *2014*. https://doi.org/10.1155/2014/149185.

(4) Leonard, B. E. Inflammation, Depression and Dementia: Are They Connected? *Neurochem. Res.* **2007**, *32* (10), 1749–1756. https://doi.org/10.1007/s11064-007-9385-y.

(5) Hunter, P. The Inflammation Theory of Disease. the Growing Realization That Chronic Inflammation Is Crucial in Many Diseases Opens New Avenues for Treatment. *EMBO Rep.* **2012**, *13* (11), 968–970. https://doi.org/10.1038/embor.2012.142.

(6) Organization, T. world H. *The World Health Report 1998. Life in the 21st Century: A Vision for All.*; 1998.

(7) Organization, T. world H. *The World Health Report 2002: Reducing Risks, Promoting Healthy Life*; 2002.

(8) Birnbaum, H.; Pike, C.; Kaufman, R.; Maynchenko, M.; Kidolezi, Y.; Cifaldi, M. Societal Cost of Rheumatoid Arthritis Patients in the US. *Curr. Med. Res. Opin.* **2010**, *26* (1), 77–90. https://doi.org/10.1185/03007990903422307.

(9) El-Gabalawy, H.; Guenther, L. C.; Bernstein, C. N. Epidemiology of Immune-Mediated Inflammatory Diseases: Incidence, Prevalence, Natural History, and Comorbidities. *J. Rheumatol.* **2010**, *37* (SUPPL. 85), 2–10. https://doi.org/10.3899/jrheum.091461.

(10) Marshall, J. S.; Warrington, R.; Watson, W.; Kim, H. L. An Introduction to Immunology and Immunopathology. *Allergy Asthma. Clin. Immunol.* **2018**, *14* (Suppl 2), 49. https://doi.org/10.1186/s13223-018-0278-1.

(11) Zak, D. E.; Aderem, A. Systems Biology of Innate Immunity. *Immunol. Rev.* **2009**, *227* (1), 264–282. https://doi.org/10.1111/j.1600-065X.2008.00721.x.

(12) Liu, J.; Cao, X. Cellular and Molecular Regulation of Innate Inflammatory Responses. *Cell. Mol. Immunol.* **2016**, *13* (6), 711–721. https://doi.org/10.1038/cmi.2016.58.

(13) Kobayashi, S. D.; DeLeo, F. R. Role of Neutrophils in Innate Immunity: A Systems Biology-Level Approach. *WIREs Syst. Biol. Med.* **2009**, *1* (3), 309–333.

https://doi.org/10.1002/wsbm.32.

(14) Caielli, S.; Banchereau, J.; Pascual, V. Neutrophils Come of Age in Chronic Inflammation. *Curr. Opin. Immunol.* **2012**, *24* (6), 671–677. https://doi.org/https://doi.org/10.1016/j.coi.2012.09.008.

(15) Silvestre-Roig, C.; Hidalgo, A.; Soehnlein, O. Neutrophil Heterogeneity: Implications for Homeostasis and Pathogenesis. *Blood* **2016**, *127* (18), 2173–2181. https://doi.org/10.1182/blood-2016-01-688887.

(16) Deniset, J. F.; Kubes, P. Neutrophil Heterogeneity: Bona Fide Subsets or Polarization States? *J. Leukoc. Biol.* **2018**, *103* (5), 829–838. https://doi.org/10.1002/JLB.3RI0917-361R.

(17) Eruslanov, E. B. Phenotype and Function of Tumor-Associated Neutrophils and Their Subsets in Early-Stage Human Lung Cancer. *Cancer Immunol. Immunother.* **2017**, *66* (8), 997–1006. https://doi.org/10.1007/s00262-017-1976-0.

(18) Denny, M. F.; Yalavarthi, S.; Zhao, W.; Thacker, S. G.; Anderson, M.; Sandy, A. R.; McCune, W. J.; Kaplan, M. J. A Distinct Subset of Proinflammatory Neutrophils Isolated from Patients with Systemic Lupus Erythematosus Induces Vascular Damage and Synthesizes Type I IFNs. *J. Immunol.* **2010**, *184* (6), 3284–3297. https://doi.org/10.4049/jimmunol.0902199.

(19) Pillay, J.; Den Braber, I.; Vrisekoop, N.; Kwast, L. M.; De Boer, R. J.; Borghans, J. A. M.; Tesselaar, K.; Koenderman, L. In Vivo Labeling with 2H2O Reveals a Human Neutrophil Lifespan of 5.4 Days. *Blood* **2010**, *116* (4), 625–627. https://doi.org/10.1182/blood-2010-01-259028.

(20) Tak, T.; Tesselaar, K.; Pillay, J.; Borghans, J. A. M.; Koenderman, L. What's Your Age Again? Determination of Human Neutrophil Half-Lives Revisited. *J. Leukoc. Biol.* **2013**, *94* (4), 595–601. https://doi.org/10.1189/jlb.1112571.

(21) Hind, L. E.; Ingram, P. N.; Beebe, D. J.; Huttenlocher, A. Interaction with an Endothelial Lumen Increases Neutrophil Lifetime and Motility in Response to P. Aeruginosa. *Blood* **2018**, *132* (17), blood-2018-05-848465. https://doi.org/10.1182/blood-2018-05-848465.

(22) Zhang, X.; Kluger, Y.; Nakayama, Y.; Poddar, R.; Whitney, C.; Detora, A.; Weissman, S. M.; Newburger, P. E. Gene Expression in Mature Neutrophils : Early Responses to Inflammatory Stimuli Abstract : Neutrophils Provide an Essential de- Play a Major Role in Tissue Damage during Inflam-. *J. Leukoc. Biol.* **2004**, *75* (2), 358–372. https://doi.org/10.1189/jlb.0903412.1.

(23) Subrahmanyam, Y. V. B. K.; Yamaga, S.; Prashar, Y.; Lee, H. H.; Hoe, N. P.; Kluger, Y.; Gerstein, M.; Goguen, J. D.; Newburger, P. E.; Weissman, S. M. RNA Expression Patterns Change Dramatically in Human Neutrophils Exposed to Bacteria. *Blood* **2001**, *97* (8),

2457–2468. https://doi.org/10.1182/blood.V97.8.2457.

(24) Kolaczkowska, E.; Kubes, P. Neutrophil Recruitment and Function in Health and Inflammation. *Nat. Rev. Immunol.* **2013**, *13* (3), 159–175. https://doi.org/10.1038/nri3399.

(25) Filippi, M. D. Neutrophil Transendothelial Migration: Updates and New Perspectives. *Blood* **2019**, *133* (20), 2149–2158. https://doi.org/10.1182/blood-2018-12-844605.

(26) Khire, T. S.; Salminen, A. T.; Swamy, H.; Lucas, K. S.; McCloskey, M. C.; Ajalik, R. E.; Chung, H. H.; Gaborski, T. R.; Waugh, R. E.; Glading, A. J.; McGrath, J. L. Microvascular Mimetics for the Study of Leukocyte–Endothelial Interactions. *Cell. Mol. Bioeng.* **2020**, *13* (2), 125–139. https://doi.org/10.1007/s12195-020-00611-6.

(27) Maas, S. L.; Soehnlein, O.; Viola, J. R. Organ-Specific Mechanisms of Transendothelial Neutrophil Migration in the Lung, Liver, Kidney, and Aorta. *Front. Immunol.* **2018**, *9* (NOV), 1–24. https://doi.org/10.3389/fimmu.2018.02739.

(28) Miralda, I.; Uriarte, S. M.; McLeish, K. R. Multiple Phenotypic Changes Define Neutrophil Priming. *Front. Cell. Infect. Microbiol.* **2017**, *7* (May), 1–13. https://doi.org/10.3389/fcimb.2017.00217.

(29) Harvie, E. A.; Huttenlocher, A. Neutrophils in Host Defense: New Insights from Zebrafish. *J. Leukoc. Biol.* **2015**, *98* (4), 523–537. https://doi.org/10.1189/jlb.4MR1114-524R.

(30) Tao, L.; Reese, T. A. Making Mouse Models That Reflect Human Immune Responses. *Trends Immunol.* **2017**, *38* (3), 181–193. https://doi.org/10.1016/j.it.2016.12.007.

(31) Mestas, J.; Hughes, C. C. W. Of Mice and Not Men: Differences between Mouse and Human Immunology. *J. Immunol.* **2004**, *172* (5), 2731–2738. https://doi.org/10.4049/jimmunol.172.5.2731.

(32) Rigby, D. A.; Ferguson, D. J. P.; Johnson, L. A.; Jackson, D. G. Neutrophils Rapidly Transit Inflamed Lymphatic Vessel Endothelium via Integrin-Dependent Proteolysis and Lipoxin-Induced Junctional Retraction. *J. Leukoc. Biol.* **2015**, *98* (6), 897–912. https://doi.org/10.1189/jlb.1hi0415-149r.

(33) Hampton, H. R.; Bailey, J.; Tomura, M.; Brink, R.; Chtanova, T. Microbe-Dependent Lymphatic Migration of Neutrophils Modulates Lymphocyte Proliferation in Lymph Nodes. *Nat. Commun.* **2015**, *6* (May), 1–11. https://doi.org/10.1038/ncomms8139.

(34) Hampton, H. R.; Chtanova, T. The Lymph Node Neutrophil. *Semin. Immunol.* **2016**, *28* (2), 129–136. https://doi.org/10.1016/j.smim.2016.03.008.

(35) Pittman, K.; Kubes, P. Damage-Associated Molecular Patterns Control Neutrophil Recruitment. *J. Innate Immun.* **2013**, *5* (4), 315–323. https://doi.org/10.1159/000347132.

(36) Prince, L. R.; Whyte, M. K.; Sabroe, I.; Parker, L. C. The Role of TLRs in Neutrophil Activation. *Curr. Opin. Pharmacol.* **2011**, *11* (4), 397–403. https://doi.org/10.1016/j.coph.2011.06.007.

(37) Dürr, M. C.; Kristian, S. A.; Otto, M.; Matteoli, G.; Margolis, P. S.; Trias, J.; van Kessel, K. P.; van Strijp, J. A.; Bohn, E.; Landmann, R.; Peschel, A. Neutrophil Chemotaxis by Pathogen-Associated Molecular Patterns - Formylated Peptides Are Crucial but Not the Sole Neutrophil Attractants Produced by Staphylococcus Aureus. *Cell. Microbiol.* **2006**, *8* (2), 207–217. https://doi.org/10.1111/j.1462-5822.2005.00610.x.

(38) Griffith, J. W.; Sokol, C. L.; Luster, A. D. Chemokines and Chemokine Receptors: Positioning Cells for Host Defense and Immunity. *Annu. Rev. Immunol.* **2014**, *32* (1), 659–702. https://doi.org/10.1146/annurev-immunol-032713-120145.

(39) Gauthier, J. F.; Fortin, A.; Bergeron, Y.; Dumas, M. C.; Champagne, M. E.; Bergeron, M. G. Differential Contribution of Bacterial N-Formyl-Methionyl-Leucyl- Phenylalanine and Host-Derived CXC Chemokines to Neutrophil Infiltration into Pulmonary Alveoli during Murine Pneumococcal Pneumonia. *Infect. Immun.* **2007**, *75* (11), 5361–5367. https://doi.org/10.1128/IAI.02008-06.

(40) Tecchio, C.; Micheletti, A.; Cassatella, M. A. Neutrophil-Derived Cytokines: Facts beyond Expression. *Front. Immunol.* **2014**, *5* (OCT), 1–7. https://doi.org/10.3389/fimmu.2014.00508.

(41) Phillipson, M.; Kubes, P. The Neutrophil in Vascular Inflammation. *Nat. Med.* **2011**, *17* (11), 1381–1390. https://doi.org/10.1038/nm.2514.

(42) Nahrendorf, M.; Swirski, F. K. Neutrophil-Macrophage Communication in Inflammation and Atherosclerosis. *Science (80-.).* **2015**, *349* (6245), 237–238. https://doi.org/10.1126/science.aac7801.

(43) Prame Kumar, K.; Nicholls, A. J.; Wong, C. H. Y. Partners in Crime: Neutrophils and Monocytes/Macrophages in Inflammation and Disease. *Cell Tissue Res.* **2018**, *371* (3), 551–565. https://doi.org/10.1007/s00441-017-2753-2.

(44) Silva, M. T. When Two Is Better than One: Macrophages and Neutrophils Work in Concert in Innate Immunity as Complementary and Cooperative Partners of a Myeloid Phagocyte System. *J. Leukoc. Biol.* **2010**, *87* (1), 93–106. https://doi.org/10.1189/jlb.0809549.

(45) Wang, J.; Hossain, M.; Thanabalasuriar, A.; Gunzer, M.; Meininger, C.; Kubes, P. Visualizing the Function and Fate of Neutrophils in Sterile Injury and Repair Jing. *Science (80-.).* **2017**, *116* (October), 111–116.

(46) Powell, D.; Tauzin, S.; Hind, L. E.; Deng, Q.; Beebe, D. J.; Huttenlocher, A. Chemokine Signaling and the Regulation of Bidirectional Leukocyte Migration in Interstitial Tissues. *Cell Rep.* **2017**, *19* (8), 1572–1585. https://doi.org/10.1016/j.celrep.2017.04.078.

(47) Buckley, C. D.; Ross, E. A.; McGettrick, H. M.; Osborne, C. E.; Haworth, O.; Schmutz, C.; Stone, P. C. W.; Salmon, M.; Matharu, N. M.; Vohra, R. K.; Nash, G. B.; Rainger, G. E. Identification of a Phenotypically and Functionally Distinct Population of Long-Lived Neutrophils in a Model of Reverse Endothelial Migration. *J. Leukoc. Biol.* **2006**, *79* (2), 303–311. https://doi.org/10.1189/jlb.0905496.

(48) Hamza, B.; Irimia, D. Whole Blood Human Neutrophil Trafficking in a Microfluidic Model of Infection and Inflammation. *Lab Chip* **2015**, *15* (12), 2625–2633. https://doi.org/10.1039/C5LC00245A.

(49) Loynes, C. A.; Lee, J. A.; Robertson, A. L.; Steel, M. J. G.; Ellett, F.; Feng, Y.; Levy, B. D.; Whyte, M. K. B.; Renshaw, S. A. PGE2 Production at Sites of Tissue Injury Promotes an Anti-Inflammatory Neutrophil Phenotype and Determines the Outcome of Inflammation Resolution in Vivo. *Sci. Adv.* **2018**, *4* (9). https://doi.org/10.1126/sciadv.aar8320.

(50) De Oliveira, S.; Rosowski, E. E.; Huttenlocher, A. Neutrophil Migration in Infection and Wound Repair: Going Forward in Reverse. *Nat. Rev. Immunol.* **2016**, *16* (6), 378–391. https://doi.org/10.1038/nri.2016.49.

(51) An, W. F.; Tolliday, N. Cell-Based Assays for High-Throughput Screening. *Mol. Biotechnol.* **2010**, *45* (2), 180–186. https://doi.org/10.1007/s12033-010-9251-z.

(52) Brouwer, M.; Zhou, H.; Nadif Kasri, N. Choices for Induction of Pluripotency: Recent Developments in Human Induced Pluripotent Stem Cell Reprogramming Strategies. *Stem Cell Rev. Reports* **2016**, *12* (1), 54–72. https://doi.org/10.1007/s12015-015-9622-8.

(53) Bowey-Dellinger, K.; Dixon, L.; Ackerman, K.; Vigueira, C.; Suh, Y. K.; Lyda, T.; Sapp, K.; Grider, M.; Crater, D.; Russell, T.; Elias, M.; Coffield, V. M.; Segarra, V. A. Introducing Mammalian Cell Culture and Cell Viability Techniques in the Undergraduate Biology Laboratory †. *J. Microbiol. Biol. Educ.* **2017**, *18* (2). https://doi.org/10.1128/jmbe.v18i2.1264.

(54) Evans Anderson, H. J. CRISPR in the Undergraduate Classroom: A CURE. *FASEB J.* **2017**, *31* (1_supplement), 589.6-589.6. https://doi.org/10.1096/fasebj.31.1_supplement.589.6.

(55) Robinton, D. A.; Daley, G. Q. The Promise of Induced Pluripotent Stem Cells in Research and Therapy. *Nature* **2012**, *481* (7381), 295–305. https://doi.org/10.1038/nature10761.

(56) Ashton, R. S.; Keung, A. J.; Peltier, J.; Schaffer, D. V. Progress and Prospects for Stem Cell Engineering. *Annu. Rev. Chem. Biomol. Eng.* **2011**, *2* (1), 479–502. https://doi.org/10.1146/annurev-chembioeng-061010-114105.

(57) Lee, G. Y.; Kenny, P. A.; Lee, E. H.; Bissell, M. J. Three-Dimensional Culture Models of Normal and Malignant Breast Epithelial Cells. *Nat. Methods* **2007**, *4* (4), 359–365. https://doi.org/10.1038/nmeth1015.

(58) Kenny, P. A.; Lee, G. Y.; Myers, C. A.; Neve, R. M.; Semeiks, J. R.; Spellman, P. T.; Lorenz, K.; Lee, E. H.; Barcellos-Hoff, M. H.; Petersen, O. W.; Gray, J. W.; Bissell, M. J. The Morphologies of Breast Cancer Cell Lines in Three-Dimensional Assays Correlate with Their Profiles of Gene Expression. *Mol. Oncol.* **2007**, *1* (1), 84–96. https://doi.org/10.1016/j.molonc.2007.02.004.

(59) Elliott, N. T.; Yuan, F. A Review of Three-Dimensional in Vitro Tissue Models for Drug Discovery and Transport Studies. *J. Pharm. Sci.* **2011**, *100* (1), 59–74. https://doi.org/10.1002/jps.22257.

(60) Bischel, L. L.; Sung, K. E.; Jiménez-Torres, J. A.; Mader, B.; Keely, P. J.; Beebe, D. J. The Importance of Being a Lumen. *FASEB J.* **2014**, *28* (11), 4583–4590. https://doi.org/10.1096/fj.13-243733.

(61) Khademhosseini, A.; Du, Y.; Rajalingam, B.; Vacanti, J. P.; Langer, R. S. Microscale Technologies for Tissue Engineering. *Adv. Tissue Eng.* **2008**, *103* (8), 349–369. https://doi.org/10.1142/9781848161832_0017.

(62) Young, E. W. K.; Beebe, D. J. Fundamentals of Microfluidic Cell Culture in Controlled Microenvironments. *Chem. Soc. Rev.* **2010**, *39* (3), 1036–1048. https://doi.org/10.1039/b909900j.

(63) Sung, K. E.; Beebe, D. J. Microfluidic 3D Models of Cancer. *Adv. Drug Deliv. Rev.* **2014**, *79*, 68–78. https://doi.org/10.1016/j.addr.2014.07.002.

(64) Bryant, D. M.; Mostov, K. E. From Cells to Organs: Building Polarized Tissue. *Nat. Rev. Mol. Cell Biol.* **2008**, *9* (11), 887–901. https://doi.org/10.1038/nrm2523.

(65) Moussavi-Harami, S. F.; Mladinich, K. M.; Sackmann, E. K.; Shelef, M. A.; Starnes, T. W.; Guckenberger, D. J.; Huttenlocher, A.; Beebe, D. J. Microfluidic Device for Simultaneous Analysis of Neutrophil Extracellular Traps and Production of Reactive Oxygen Species. *Integr. Biol.* **2016**, *8* (2), 243–252. https://doi.org/10.1039/C5IB00225G.

(66) Kusuma, S.; Shen, Y.-I.; Hanjaya-Putra, D.; Mali, P.; Cheng, L.; Gerecht, S. Self-Organized Vascular Networks from Human Pluripotent Stem Cells in a Synthetic Matrix. *Proc. Natl. Acad. Sci.* **2013**, *110* (31), 12601–12606. https://doi.org/10.1073/pnas.1306562110.

(67) Zhu, W.; Qu, X.; Zhu, J.; Ma, X.; Patel, S.; Liu, J.; Wang, P.; Lai, C. S. E.; Gou, M.; Xu, Y.; Zhang, K.; Chen, S. Direct 3D Bioprinting of Prevascularized Tissue Constructs with Complex Microarchitecture. *Biomaterials* **2017**, *124*, 106–115. https://doi.org/10.1016/j.biomaterials.2017.01.042.

(68) Tsvirkun, D.; Grichine, A.; Duperray, A.; Misbah, C.; Bureau, L. Microvasculature on a Chip: Study of the Endothelial Surface Layer and the Flow Structure of Red Blood Cells. *Sci. Rep.* **2017**, *7* (October 2016), 1–11. https://doi.org/10.1038/srep45036.

(69) Jiménez-Torres, J. A.; Peery, S. L.; Sung, K. E.; Beebe, D. J. LumeNEXT: A Practical Method to Pattern Luminal Structures in ECM Gels. *Adv. Healthc. Mater.* **2016**, *5* (2), 198–204. https://doi.org/10.1002/adhm.201500608.

(70) Ingram, P. N.; Hind, L. E.; Jiminez-Torres, J. A.; Huttenlocher, A.; Beebe, D. J. An Accessible Organotypic Microvessel Model Using IPSC-Derived Endothelium. *Adv. Healthc. Mater.* **2018**, *7* (2), 1–10. https://doi.org/10.1002/adhm.201700497.

(71) Yu, J.; Berthier, E.; Craig, A.; de Groot, T. E.; Sparks., S.; Ingram, P.; Jarrard, D.; Huang, W.; Beebe, D.; Theberge, A. B. Reconfigurable Open Microfluidics Illuminates the Role of Sequence and Timing in Cancer Inflammation Signaling. *Nat. Biomed. Eng.* **2019**.

(72) Deniset, J. F.; Kubes, P. Neutrophil Heterogeneity: Bona Fide Subsets or Polarization States? *J. Leukoc. Biol.* **2018**, No. January, 1–10. https://doi.org/10.1002/JLB.3RI0917-361R.

(73) Scapini, P.; Cassatella, M. Social Networking of Human Neutrophils within the Immune System \n. *Blood* **2014**, *124* (First Edition Paper), 710–720. https://doi.org/10.1182/blood-2014-03-453217.The.

(74) Xia, Y.; Whitesides, G. M. Soft Lithography. *Angew. Chemie Int. Ed.* **1998**, *37* (5), 550–575. https://doi.org/doi:10.1002/(SICI)1521-3773(19980316)37:5<550::AID-ANIE550>3.0.CO;2-G.

(75) Guckenberger, D. J.; de Groot, T.; Wan, A. M.-D.; Beebe, D.; Young, E. Micromilling: A Method for Ultra-Rapid Prototyping of Plastic Microfluidic Devices. *Lab Chip* **2015**, *15* (11), 2364–2378. https://doi.org/10.1039/C5LC00234F.

(76) Gribbon, P.; Hardingham, T. E. Macromolecular Diffusion of Biological Polymers Measured by Confocal Fluorescence Recovery after Photobleaching. *Biophys. J.* **1998**, *75* (2), 1032–1039. https://doi.org/10.1016/S0006-3495(98)77592-7.

(77) Hettiaratchi, M. H.; Schudel, A.; Rouse, T.; García, A. J.; Thomas, S. N.; Guldberg, R. E.; McDevitt, T. C. A Rapid Method for Determining Protein Diffusion through Hydrogels for Regenerative Medicine Applications. *APL Bioeng.* **2018**, *2* (2), 026110. https://doi.org/10.1063/1.4999925.

(78) Charras, G.; Sahai, E. Physical Influences of the Extracellular Environment on Cell Migration. *Nat. Rev. Mol. Cell Biol.* **2014**, *15* (12), 813–824. https://doi.org/10.1038/nrm3897.

(79) Tanino, Y.; Coombe, D. R.; Gill, S. E.; Kett, W. C.; Kajikawa, O.; Proudfoot, A. E. I.; Wells, T. N. C.; Parks, W. C.; Wight, T. N.; Martin, T. R.; Frevert, C. W. Kinetics of Chemokine–Glycosaminoglycan Interactions Control Neutrophil Migration into the Airspaces of the Lungs. *J. Immunol.* **2010**, *184* (5), 2677–2685. https://doi.org/10.4049/jimmunol.0903274.

(80) Pichert, A.; Schlorke, D.; Franz, S.; Arnhold, J. Functional Aspects of the Interaction between Interleukin-8 and Sulfated Glycosaminoglycans. *Biomatter* **2012**, *2* (3), 142–148. https://doi.org/10.4161/biom.21316.

(81) Yao, Y.; Matsushima, H.; Ohtola, J. A.; Geng, S.; Lu, R.; Takashima, A. Neutrophil Priming Occurs in a Sequential Manner and Can Be Visualized in Living Animals by Monitoring IL-1β Promoter Activation. *J. Immunol.* **2014**, *194* (3), 1211–1224. https://doi.org/10.4049/jimmunol.1402018.

(82) Lakschevitz, F. S.; Visser, M. B.; Sun, C.; Glogauer, M. Neutrophil Transcriptional Profile Changes during Transit from Bone Marrow to Sites of Inflammation. *Cell. Mol. Immunol.* **2015**, *12* (1), 53–65. https://doi.org/10.1038/cmi.2014.37.

(83) Jiang, K.; Sun, X.; Chen, Y.; Shen, Y.; Jarvis, J. N. RNA Sequencing from Human Neutrophils Reveals Distinct Transcriptional Differences Associated with Chronic Inflammatory States. *BMC Med. Genomics* **2015**, *8* (1), 1–13. https://doi.org/10.1186/s12920-015-0128-7.

(84) Ecker, S.; Chen, L.; Pancaldi, V.; Bagger, F. O.; Fernández, J. M.; Carrillo de Santa Pau, E.; Juan, D.; Mann, A. L.; Watt, S.; Casale, F. P.; Sidiropoulos, N.; Rapin, N.; Merkel, A.; Stunnenberg, H. G.; Stegle, O.; Frontini, M.; Downes, K.; Kuijpers, T. W.; Kuijpers, T. W.; Rico, D.; Valencia, A.; Beck, S.; Soranzo, N.; Paul, D. S.; Albers, C. A.; Amstislavskiy, V.; Ashford, S.; Bomba, L.; Bujold, D.; Burden, F.; Busche, S.; Caron, M.; Chen, S. H.; Cheung, W. A.; Clarke, L.; Colgiu, I.; Datta, A.; Delaneau, O.; Elding, H.; Farrow, S.; Garrido-Martín, D.; Ge, B.; Guigo, R.; Iotchkova, V.; Kundu, K.; Kwan, T.; Lambourne, J. J.; Lowy, E.; Mead, D.; Pourfarzad, F.; Redensek, A.; Rehnstrom, K.; Rendon, A.; Richardson, D.; Risch, T.; Rowlston, S.; Shao, X.; Simon, M. M.; Sultan, M.; Walter, K.; Wilder, S. P.; Yan, Y.; Antonarakis, S. E.; Bourque, G.; Dermitzakis, E. T.; Flicek, P.; Lehrach, H.; Martens, J. H. A.; Yaspo, M. L.; Ouwehand, W. H. Genome-Wide Analysis of Differential Transcriptional and Epigenetic Variability across Human Immune Cell Types. *Genome Biol.* **2017**, *18* (1), 1–17. https://doi.org/10.1186/s13059-017-1156-8.

(85) Galli, S. J.; Borregaard, N.; Wynn, T. A. Phenotypic and Functional Plasticity of Cells of Innate Immunity: Macrophages, Mast Cells and Neutrophils. *Nat. Immunol.* **2011**, *12* (11), 1035–1044. https://doi.org/10.1038/ni.2109.

(86) Drost, E. M.; MacNee, W. Potential Role of IL-8, Platelet-Activating Factor and TNF-α in the Sequestration of Neutrophils in the Lung: Effects on Neutrophil Deformability, Adhesion Receptor Expression, and Chemotaxis. *Eur. J. Immunol.* **2002**, *32* (2), 393–403. https://doi.org/10.1002/1521-4141(200202)32:2<393::AID-IMMU393>3.0.CO;2-5.

(87) FAN, J.; MALIK, A. B. Toll-like Receptor-4 (TLR4) Signaling Augments Chemokine- Induced Neutrophil Migration by Modulating Cell Surface Expression of Chemokine Receptors. *Nat. Med.* **2003**, *9* (3), 315–321. https://doi.org/10.1038/nm.

(88) Fortunati, E.; Kazemier, K. M.; Grutters, J. C.; Koenderman, L.; Van Den Bosch, V. J. M. M.

Human Neutrophils Switch to an Activated Phenotype after Homing to the Lung Irrespective of Inflammatory Disease. *Clin. Exp. Immunol.* **2009**, *155* (3), 559–566. https://doi.org/10.1111/j.1365-2249.2008.03791.x.

(89) Dangerfield, J.; Larbi, K. Y.; Huang, M.-T.; Dewar, A.; Nourshargh, S. PECAM-1 (CD31) Homophilic Interaction Up-Regulates $\alpha_6\beta_1$ on Transmigrated Neutrophils In Vivo and Plays a Functional Role in the Ability of α_6 Integrins to Mediate Leukocyte Migration through the Perivascular Basement M. *J. Exp. Med.* **2002**, *196* (9), 1201–1212. https://doi.org/10.1084/jem.20020324.

(90) Woodfin, A.; Voisin, M. B.; Imhof, B. A.; Dejana, E.; Engelhardt, B.; Nourshargh, S. Endothelial Cell Activation Leads to Neutrophil Transmigration as Supported by the Sequential Roles of ICAM-2, JAM-A, and PECAM-1. *Blood* **2009**, *113* (24), 6246–6257. https://doi.org/10.1182/blood-2008-11-188375.

(91) Ferrante, C. J.; Leibovich, S. J. Regulation of Macrophage Polarization and Wound Healing. *Adv. Wound Care* **2012**, *1* (1), 10–16. https://doi.org/10.1089/wound.2011.0307.

(92) Parisi, L.; Gini, E.; Baci, D.; Tremolati, M.; Fanuli, M.; Bassani, B.; Farronato, G.; Bruno, A.; Mortara, L. Macrophage Polarization in Chronic Inflammatory Diseases: Killers or Builders? *J. Immunol. Res.* **2018**, *2018*. https://doi.org/10.1155/2018/8917804.

(93) Sica, A.; Mantovani, A. Plasticity and Polarization. *J. Clin. Invest.* **2012**, *122* (3), 787–795. https://doi.org/10.1172/JCI59643DS1.

(94) Gong, M. M.; Lugo-Cintron, K. M.; White, B. R.; Kerr, S. C.; Harari, P. M.; Beebe, D. J. Human Organotypic Lymphatic Vessel Model Elucidates Microenvironment-Dependent Signaling and Barrier Function. *Biomaterials* **2019**, *214* (November 2018), 119225. https://doi.org/10.1016/j.biomaterials.2019.119225.

(95) Phillips, D. J.; de Kretser, D. M. Follistatin: A Multifunctional Regulatory Protein. *Front. Neuroendocrinol.* **1998**, *19* (4), 287–322. https://doi.org/https://doi.org/10.1006/frne.1998.0169.

(96) DePaolo, L. V; Bicsak, T. A.; Erickson, G. F.; Shimasaki, S.; Ling, N. Follistatin and Activin: A Potential Intrinsic Regulatory System within Diverse Tissues. *Proc. Soc. Exp. Biol. Med.* **1991**, *198* (1), 500–512. https://doi.org/10.3181/00379727-198-43286A.

(97) Mather, J. P.; Moore, A.; Li, R.-H. Activins, Inhibins, and Follistatins: Further Thoughts on a Growing Family of Regulators. *Proc. Soc. Exp. Biol. Med.* **1997**, *215* (3), 209–222. https://doi.org/10.3181/00379727-215-44130.

(98) Jones, K. L.; Kretser, D. M. D.; Patella, S.; Phillips, D. J. Activin A and Follistatin in Systemic Inflammation. *Mol. Cell. Endocrinol.* **2004**, *225* (1–2), 119–125. https://doi.org/10.1016/j.mce.2004.07.010.

(99) Wu, H.; Chen, Y.; Winnall, W. R.; Phillips, D. J.; Hedger, M. P. Acute Regulation of Activin A and Its Binding Protein, Follistatin, in Serum and Tissues Following Lipopolysaccharide Treatment of Adult Male Mice. *Am. J. Physiol. - Regul. Integr. Comp. Physiol.* **2012**, *303* (6), 665–675. https://doi.org/10.1152/ajpregu.00478.2011.

(100) Kozian, D. H.; Ziche, M.; Augustin, H. G. The Activin-Binding Protein Follistatin Regulates Autocrine Endothelial Cell Activity and Induces Angiogenesis. *Lab. Invest.* **1997**, *76* (2), 267–276.

(101) Heinz, M.; Niederleithner, H. L.; Puujalka, E.; Soler-Cardona, A.; Grusch, M.; Pehamberger, H.; Loewe, R.; Petzelbauer, P. Activin A Is Anti-Lymphangiogenic in a Melanoma Mouse Model. *J. Invest. Dermatol.* **2015**, *135* (1), 212–221. https://doi.org/10.1038/jid.2014.328.

(102) Jones, K. L.; Mansell, A.; Patella, S.; Scott, B. J.; Hedger, M. P.; De Kretser, D. M.; Phillips, D. J. Activin A Is a Critical Component of the Inflammatory Response, and Its Binding Protein, Follistatin, Reduces Mortality in Endotoxemia. *Proc. Natl. Acad. Sci. U. S. A.* **2007**, *104* (41), 16239–16244. https://doi.org/10.1073/pnas.0705971104.

(103) Tian, G.; Deng, J.; Liu, Z.; Cui, X.; Wu, J.; Xie, D.; Yang, K.; Lin, F.; Santos, S.; Feng, W. The Effects of Activin A on the Migration of Human Breast Cancer Cells and Neutrophils and Their Migratory Interaction. *Exp. Cell Res.* **2017**, *357* (1), 107–115. https://doi.org/10.1016/j.yexcr.2017.05.003.

(104) Jones, K. L.; de Kretser, D. M.; Clarke, I. J.; Scheerlinck, J. P. Y.; Phillips, D. J. Characterisation of the Rapid Release of Activin A Following Acute Lipopolysaccharide Challenge in the Ewe. *J. Endocrinol.* **2004**, *182* (1), 69–80. https://doi.org/10.1677/joe.0.1820069.

(105) Whitesides, G. M.; Ostuni, E.; Jiang, X.; Ingber, D. E. S Oft L Ithography in B Iology. *Annu. Rev. Biomed. Eng.* **2001**, *3*, 335–373. https://doi.org/10.1146/annurev.bioeng.3.1.335.

(106) Walker, G. M.; Beebe, D. J. A Passive Pumping Method for Microfluidic Devices. *Lab Chip* **2002**, *2* (3), 131–134. https://doi.org/10.1039/B204381E.

(107) Dayang, E. Z.; Plantinga, J.; Ter Ellen, B.; Van Meurs, M.; Molema, G.; Moser, J. Identification of LPS-Activated Endothelial Subpopulations with Distinct Inflammatory Phenotypes and Regulatory Signaling Mechanisms. *Front. Immunol.* **2019**, *10* (MAY), 1–12. https://doi.org/10.3389/fimmu.2019.01169.

(108) McDonald, B.; Kubes, P. Chemokines: Sirens of Neutrophil Recruitment-but Is It Just One Song? *Immunity* **2010**, *33* (2), 148–149. https://doi.org/10.1016/j.immuni.2010.08.006.

(109) Scapini, P.; Lapinet-Vera, J. A.; Gasperini, S.; Calzetti, F.; Bazzoni, F.; Cassatella, M. A. The Neutrophil as a Cellular Source of Chemokines. *Immunol. Rev.* **2000**, *177* (1), 195–203. https://doi.org/10.1034/j.1600-065X.2000.17706.x.

(110) Tessier, P. A.; Naccache, P. H.; Clark-Lewis, I.; Gladue, R. P.; Neote, K. S.; McColl, S. R. Chemokine Networks in Vivo: Involvement of C-X-C and C-C Chemokines in Neutrophil Extravasation in Vivo in Response to TNF-Alpha. *J. Immunol.* **1997**, *159* (7), 3595 LP – 3602.

(111) Ardi, V. C.; Kupriyanova, T. A.; Deryugina, E. I.; Quigley, J. P. Human Neutrophils Uniquely Release TIMP-Free MMP-9 to Provide a Potent Catalytic Stimulator of Angiogenesis. *Proc. Natl. Acad. Sci. U. S. A.* **2007**, *104* (51), 20262–20267. https://doi.org/10.1073/pnas.0706438104.

(112) Miyasaka, M.; Tanaka, T. Lymphocyte Trafficking across High Endothelial Venules: Dogmas and Enigmas. *Nat. Rev. Immunol.* **2004**, *4* (5), 360–370. https://doi.org/10.1038/nri1354.

(113) von Vietinghoff, S.; Ley, K. Homeostatic Regulation of Blood Neutrophil Counts. *J. Immunol.* **2008**, *181* (8), 5183–5188. https://doi.org/10.4049/jimmunol.181.8.5183.

(114) Chen, Y.; Wu, H.; Winnall, W. R.; Loveland, K. L.; Makanji, Y.; Phillips, D. J.; Smith, J. A.; Hedger, M. P. Tumour Necrosis Factor-α Stimulates Human Neutrophils to Release Preformed Activin A. *Immunol. Cell Biol.* **2011**, *89* (8), 889–896. https://doi.org/10.1038/icb.2011.12.

(115) Moreland, J. G.; Bailey, G.; Nauseef, W. M.; Weiss, J. P. Organism-Specific Neutrophil-Endothelial Cell Interactions in Response to Escherichia Coli , Streptococcus Pneumoniae , and Staphylococcus Aureus . *J. Immunol.* **2004**, *172* (1), 426–432. https://doi.org/10.4049/jimmunol.172.1.426.

(116) Roberts, V. J. Tissue-Specific Expression of Inhibin/Activin Subunit and Follistatin MRNAs in Mid- to Late-Gestational Age Human Fetal Testis and Epididymis. *Endocrine* **1997**, *6* (1), 85–90. https://doi.org/10.1007/BF02738807.

(117) Winnall, W. R.; Wu, H.; Sarraj, M. A.; Rogers, P. A. W.; de Kretser, D. M.; Girling, J. E.; Hedger, M. P. Expression Patterns of Activin, Inhibin and Follistatin Variants in the Adult Male Mouse Reproductive Tract Suggest Important Roles in the Epididymis and Vas Deferens. *Reprod. Fertil. Dev.* **2013**, *25* (3), 570–580.

(118) Tuuri, T.; Erämaa, M.; Hildén, K.; Ritvos, O. The Tissue Distribution of Activin Beta A- and Beta B-Subunit and Follistatin Messenger Ribonucleic Acids Suggests Multiple Sites of Action for the Activin-Follistatin System during Human Development. *J. Clin. Endocrinol. Metab.* **1994**, *78* (6), 1521–1524. https://doi.org/10.1210/jcem.78.6.8200957.

(119) Yang, Y.; Zhang, N.; Van Crombruggen, K.; Lan, F.; Hu, G.; Hong, S.; Bachert, C. Differential Expression and Release of Activin a and Follistatin in Chronic Rhinosinusitis with and without Nasal Polyps. *PLoS One* **2015**, *10* (6), 1–14. https://doi.org/10.1371/journal.pone.0128564.

(120) Petrakou, E.; Fotopoulos, S.; Anagnostakou, M.; Anatolitou, F.; Samitas, K.; Semitekolou, M.; Xanthou, G.; Xanthou, M. Activin-A Exerts a Crucial Anti-Inflammatory Role in Neonatal Infections. *Pediatr. Res.* **2013**, *74* (6), 675–681. https://doi.org/10.1038/pr.2013.159.

(121) DIller, M.; Frommer, K.; Dankbar, B.; Tarner, I.; Hülser, M. L.; Tsiklauri, L.; Hasseli, R.; Sauerbier, M.; Pap, T.; Rehart, S.; Müller-Ladner, U.; Neumann, E. The Activin-Follistatin Anti-Inflammatory Cycle Is Deregulated in Synovial Fibroblasts. *Arthritis Res. Ther.* **2019**, *21* (1), 1–11. https://doi.org/10.1186/s13075-019-1926-7.

(122) Eldar-Geva, T.; Spitz, I. M.; Groome, N. P.; Margalioth, E. J.; Homburg, R. Follistatin and Activin A Serum Concentrations in Obese and Non-Obese Patients with Polycystic Ovary Syndrome. *Hum. Reprod.* **2001**, *16* (12), 2552–2556. https://doi.org/10.1093/humrep/16.12.2552.

(123) Lin, S. De; Kawakami, T.; Ushio, A.; Sato, A.; Sato, S. I.; Iwai, M.; Endo, R.; Takikawa, Y.; Suzuki, K. Ratio of Circulating Follistatin and Activin A Reflects the Severity of Acute Liver Injury and Prognosis in Patients with Acute Liver Failure. *J. Gastroenterol. Hepatol.* **2006**, *21* (2), 374–380. https://doi.org/10.1111/j.1440-1746.2005.04036.x.

(124) Fumagalli, M.; Musso, T.; Vermi, W.; Scutera, S.; Daniele, R.; Alotto, D.; Cambieri, I.; Ostorero, A.; Gentili, F.; Caposio, P.; Zucca, M.; Sozzani, S.; Stella, M.; Castagnoli, C. Imbalance between Activin A and Follistatin Drives Postburn Hypertrophic Scar Formation in Human Skin. *Exp. Dermatol.* **2007**, *16* (7), 600–610. https://doi.org/10.1111/j.1600-0625.2007.00571.x.

(125) Michel, U.; Shintani, Y.; Nau, R. Serum Follistatin Concentrations Are Increased in Patients with Septicaemia. *Clin. Endocrinol. (Oxf).* **1998**, *48* (4), 413–417. https://doi.org/10.1046/j.1365-2265.1998.00484.x.

(126) Hardy, C. L.; King, S. J.; Mifsud, N. A.; Hedger, M. P.; Phillips, D. J.; Mackay, F.; De Kretser, D. M.; Wilson, J. W.; Rolland, J. M.; O'Hehir, R. E. The Activin A Antagonist Follistatin Inhibits Cystic Fibrosis-like Lung Inflammation and Pathology. *Immunol. Cell Biol.* **2015**, *93* (6), 567–574. https://doi.org/10.1038/icb.2015.7.

(127) Robson, N. C.; Phillips, D. J.; McAlpine, T.; Shin, A.; Svobodova, S.; Toy, T.; Pillay, V.; Kirkpatrick, N.; Zanker, D.; Wilson, K.; Helling, I.; Wei, H.; Chen, W.; Cebon, J.; Maraskovsky, E. Activin-A: A Novel Dendritic Cell Derived Cytokine That Potently Attenuates CD40 Ligand Specific Cytokine and Chemokine Production. *Blood* **2008**, *111* (5), 2733–2743. https://doi.org/10.1182/blood-2007-03-080994.

(128) Montecucco, F.; Steffens, S.; Burger, F.; Da Costa, A.; Bianchi, G.; Bertolotto, M.; Mach, F.; Dallegri, F.; Ottonello, L. Tumor Necrosis Factor-Alpha (TNF-α) Induces Integrin CD11b/CD18 (Mac-1) up-Regulation and Migration to the CC Chemokine CCL3 (MIP-1α) on Human Neutrophils through Defined Signalling Pathways. *Cell. Signal.* **2008**, *20* (3),

557–568. https://doi.org/10.1016/j.cellsig.2007.11.008.

(129) Kang, H. Y.; Huang, H. Y.; Hsieh, C. Y.; Li, C. F.; Shyr, C. R.; Tsai, M. Y.; Chang, C.; Chuang, Y. C.; Huang, K. E. Activin A Enhances Prostate Cancer Cell Migration through Activation of Androgen Receptor and Is Overexpressed in Metastatic Prostate Cancer. *J. Bone Miner. Res.* **2009**, *24* (7), 1180–1193. https://doi.org/10.1359/jbmr.090219.

(130) Wildi, S.; Kleeff, J.; Maruyama, H.; Maurer, C. A.; Büchler, M. W.; Korc, M. Overexpression of Activin A in Stage IV Colorectal Cancer. *Gut* **2001**, *49* (3), 409–417. https://doi.org/10.1136/gut.49.3.409.

(131) Deli, A.; Kreidl, E.; Santifaller, S.; Trotter, B.; Seir, K.; Berger, W.; Schulte-Hermann, R.; Rodgarkia-Dara, C.; Grusch, M. Activins and Activin Antagonists in Hepatocellular Carcinoma. *World J. Gastroenterol.* **2008**, *14* (11), 1699–1709. https://doi.org/10.3748/wjg.14.1699.

(132) Seder, C. W.; Hnrtojo, W.; Lin, L.; Silvers, A. L.; Wang, Z.; Thomas, D. G.; Giordano, T. J.; Chen, G.; Chang, A. C.; Orringer, M. B.; Beer, D. G. Upregulated INHBA Expression May Promote Cell Proliferation and Is Associated with Poor Survival IN Lung Adenocarcinoma1 Www.Neoplasia.Com. *Neoplasia* **2009**, *11* (4), 388–396. https://doi.org/10.1593/neo.81582.

(133) Bashir, M.; Damineni, S.; Mukherjee, G.; Kondaiah, P. Activin-a Signaling Promotes Epithelial–Mesenchymal Transition, Invasion, and Metastatic Growth of Breast Cancer. *npj Breast Cancer* **2015**, *1* (May), 1–13. https://doi.org/10.1038/npjbcancer.2015.7.

(134) Reis, F. M.; Luisi, S.; Carneiro, M. M.; Cobellis, L.; Federico, M.; Camargos, A. F.; Petraglia, F. Activin, Inhibin and the Human Breast. *Mol. Cell. Endocrinol.* **2004**, *225* (1–2), 77–82. https://doi.org/10.1016/j.mce.2004.02.016.

(135) Fordyce, C. A.; Patten, K. T.; Fessenden, T. B.; DeFilippis, R. A.; Hwang, E. S.; Zhao, J.; Tlsty, T. D. Cell-Extrinsic Consequences of Epithelial Stress: Activation of Protumorigenic Tissue Phenotypes. *Breast Cancer Res.* **2012**, *14* (6). https://doi.org/10.1186/bcr3368.

(136) Zabkiewicz, C.; Resaul, J.; Hargest, R.; Jiang, W. G.; Ye, L. Increased Expression of Follistatin in Breast Cancer Reduces Invasiveness and Clinically Correlates with Better Survival. *Cancer Genomics and Proteomics* **2017**, *14* (4), 241–251. https://doi.org/10.21873/cgp.20035.

(137) Seachrist, D. D.; Sizemore, S. T.; Johnson, E.; Abdul-Karim, F. W.; Weber Bonk, K. L.; Keri, R. A. Follistatin Is a Metastasis Suppressor in a Mouse Model of HER2-Positive Breast Cancer. *Breast Cancer Res.* **2017**, *19* (1), 1–10. https://doi.org/10.1186/s13058-017-0857-y.

(138) Volpatti, L. R.; Yetisen, A. K. Commercialization of Microfluidic Devices. *Trends Biotechnol.* **2014**, *32* (7), 347–350. https://doi.org/10.1016/j.tibtech.2014.04.010.

(139) Kamei, K.-I.; Guo, S.; Yu, Z. T. F.; Takahashi, H.; Gschweng, E.; Suh, C.; Wang, X.; Tang, J.; McLaughlin, J.; Witte, O. N.; Lee, K.-B.; Tseng, H.-R. An Integrated Microfluidic Culture Device for Quantitative Analysis of Human Embryonic Stem Cells. *Lab Chip* **2009**, *9* (4), 555–563. https://doi.org/10.1039/b809105f.

(140) Giobbe, G. G.; Michielin, F.; Luni, C.; Giulitti, S.; Martewicz, S.; Dupont, S.; Floreani, A.; Elvassore, N. Functional Differentiation of Human Pluripotent Stem Cells on a Chip. *Nat. Methods* **2015**, *12* (March 2014), 1–7. https://doi.org/10.1038/nmeth.3411.

(141) Gómez-Sjöberg, R.; Leyrat, A. A.; Pirone, D. M.; Chen, C. S.; Quake, S. R. Versatile, Fully Automated, Microfluidic Cell Culture System. *Anal Chem* **2007**, *79* (22), 8557–8563. https://doi.org/10.1021/ac071311w.

(142) Liu, L.; Luo, C.; Ni, X.; Wang, L.; Yamauchi, K.; Nomura, S. M.; Nakatsuji, N.; Chen, Y. A Micro-Channel-Well System for Culture and Differentiation of Embryonic Stem Cells on Different Types of Substrate. *Biomed. Microdevices* **2010**, *12* (3), 505–511. https://doi.org/10.1007/s10544-010-9407-4.

(143) Stettenz, F. Von; Mark, D.; Haeberle, S.; Zengerlez, R. From Microfluidic Application to Nanofluidic Phenomena Issue Reviewing the Latest Advances in Microfluidic and Nanofluidic. *Chem. Soc. Rev.* **2010**, *39*, 1153–1182. https://doi.org/10.1039/b820557b.

(144) Sackmann, E. K.; Fulton, A. L.; Beebe, D. J. The Present and Future Role of Microfluidics in Biomedical Research. *Nature* **2014**, *507* (7491), 181–189.

(145) Berthier, E.; Guckenberger, D. J.; Cavnar, P.; Huttenlocher, A.; Keller, N. P.; Beebe, D. J. Kit-on-a-Lid-Assays for Accessible Self-Contained Cell Assays. *Lab Chip* **2013**, *13* (3), 424–431. https://doi.org/10.1039/c2lc41019b.

(146) Guckenberger, D. J.; Berthier, E.; Beebe, D. J. High-Density Self-Contained Microfluidic KOALA Kits for Use by Everyone. **2015**. https://doi.org/10.1177/2211068214560609.

(147) Guckenberger, D. J.; De Groot, T. E.; Wan, A. M. D.; Beebe, D. J.; Young, E. W. K. Micromilling: A Method for Ultra-Rapid Prototyping of Plastic Microfluidic Devices. *Lab Chip* **2015**, *15* (11), 2364–2378. https://doi.org/10.1039/c5lc00234f.

(148) Lippmann, E. S.; Estevez-Silva, M. C.; Ashton, R. S. Defined Human Pluripotent Stem Cell Culture Enables Highly Efficient Neuroepithelium Derivation without Small Molecule Inhibitors. *Stem Cells* **2014**, *32* (4), 1032–1042. https://doi.org/10.1002/stem.1622.

(149) Lian, X.; Hsiao, C.; Wilson, G.; Zhu, K.; Hazeltine, L. B.; Azarin, S. M.; Raval, K. K.; Zhang, J.; Kamp, T. J.; Palecek, S. P. PNAS Plus: Robust Cardiomyocyte Differentiation from Human Pluripotent Stem Cells via Temporal Modulation of Canonical Wnt Signaling. *Proc. Natl. Acad. Sci.* **2012**, *109* (27), E1848–E1857. https://doi.org/10.1073/pnas.1200250109.

(150) Kunisada, Y.; Tsubooka-Yamazoe, N.; Shoji, M.; Hosoya, M. Small Molecules Induce

Efficient Differentiation into Insulin-Producing Cells from Human Induced Pluripotent Stem Cells. *Stem Cell Res.* **2012**, *8* (2), 274–284. https://doi.org/10.1016/j.scr.2011.10.002.

(151) Villa-Diaz, L. G.; Ross, A. M.; Lahann, J.; Krebsbach, P. H. Concise Review: The Evolution of Human Pluripotent Stem Cell Culture: From Feeder Cells to Synthetic Coatings. *Stem Cells* **2013**, *31* (1), 1–7. https://doi.org/10.1002/stem.1260.

(152) Chen, K. G.; Mallon, B. S.; Mckay, R. D. G.; Robey, P. G. Protocol Review Human Pluripotent Stem Cell Culture : Considerations for Maintenance , Expansion , and Therapeutics. *Stem Cell* **2014**, *14* (1), 13–26. https://doi.org/10.1016/j.stem.2013.12.005.

(153) Justice, B. A.; Badr, N. A.; Felder, R. A. 3D Cell Culture Opens New Dimensions in Cell-Based Assays. *Drug Discov. Today* **2009**, *14* (1–2), 102–107. https://doi.org/10.1016/j.drudis.2008.11.006.

(154) Ireland, R. G.; Simmons, C. A. Human Pluripotent Stem Cell Mechanobiology: Manipulating the Biophysical Microenvironment for Regenerative Medicine and Tissue Engineering Applications. *Stem Cells* **2015**, *33* (11), 3187–3196. https://doi.org/10.1002/stem.2105.

(155) Mathieu, J.; Zhang, Z.; Nelson, A.; Lamba, D. A.; Reh, T. A.; Ware, C.; Ruohola-Baker, H. Hypoxia Induces Re-Entry of Committed Cells into Pluripotency. *Stem Cells* **2013**, *31* (9), 1737–1748. https://doi.org/10.1002/stem.1446.

(156) Liang, G.; Zhang, Y. Embryonic Stem Cell and Induced Pluripotent Stem Cell: An Epigenetic Perspective. *Cell Res.* **2013**, *23* (1), 49–69. https://doi.org/10.1038/cr.2012.175.

(157) Watt, F. M.; Huck, W. T. S. Role of the Extracellular Matrix in Regulating Stem Cell Fate. *Nat. Rev. Mol. Cell Biol.* **2013**, *14* (8), 467–473. https://doi.org/10.1038/nrm3620.

(158) Van Der Sanden, B.; Dhobb, M.; Berger, F.; Wion, D. Optimizing Stem Cell Culture. *J. Cell. Biochem.* **2010**, *111* (4), 801–807. https://doi.org/10.1002/jcb.22847.

(159) Rowland, T. J.; Miller, L. M.; Blaschke, A. J.; Doss, E. L.; Bonham, A. J.; Hikita, S. T.; Johnson, L. V; Clegg, D. O. Roles of Integrins in Human Induced Pluripotent Stem Cell Growth on Matrigel and Vitronectin. *Stem Cells Dev.* **2009**, *19* (8), 1231–1240. https://doi.org/10.1089/scd.2009.0328.

(160) Yu, H.; Meyvantsson, I.; Shkel, I. A.; Beebe, D. J. Diffusion Dependent Cell Behavior in Microenvironments. *Lab Chip* **2005**, *5* (10), 1089–1095. https://doi.org/10.1039/b504403k.

(161) Domenech, M.; Yu, H.; Warrick, J.; Badders, N. M.; Meyvantsson, I.; Alexander, C. M.; Beebe, D. J. Cellular Observations Enabled by Microculture: Paracrine Signaling and

Population Demographics. *Integr. Biol.* **2009**, *1* (3), 267–274. https://doi.org/10.1039/b823059e.

(162) Yu, H.; Alexander, C. M.; Beebe, D. J. Understanding Microchannel Culture: Parameters Involved in Soluble Factor Signaling. *Lab Chip* **2007**, *7* (6), 726–730. https://doi.org/10.1039/b618793e.

(163) Doetsch, F. A Niche for Adult Neural Stem Cells. *Curr. Opin. Genet. Dev.* **2003**, *13* (5), 543–550. https://doi.org/10.1016/j.gde.2003.08.012.

(164) Eiraku, M.; Watanabe, K.; Matsuo-Takasaki, M.; Kawada, M.; Yonemura, S.; Matsumura, M.; Wataya, T.; Nishiyama, A.; Muguruma, K.; Sasai, Y. Self-Organized Formation of Polarized Cortical Tissues from ESCs and Its Active Manipulation by Extrinsic Signals. *Cell Stem Cell* **2008**, *3* (5), 519–532. https://doi.org/10.1016/j.stem.2008.09.002.

(165) Zhou, B.; Ma, Q.; Rajagopal, S.; Wu, S. M.; Domian, I.; Rivera-Feliciano, J.; Jiang, D.; Von Gise, A.; Ikeda, S.; Chien, K. R.; Pu, W. T. Epicardial Progenitors Contribute to the Cardiomyocyte Lineage in the Developing Heart. *Nature* **2008**, *454* (7200), 109–113. https://doi.org/10.1038/nature07060.

(166) Kubo, A.; Shinozaki, K.; Shannon, J. M.; Kouskoff, V.; Kennedy, M.; Woo, S.; Fehling, H. J.; Keller, G. Development of Definitive Endoderm from Embryonic Stem Cells in Culture. *Development* **2004**, *131* (7), 1651–1662. https://doi.org/10.1242/dev.01044.

(167) Takeuchi, H.; Nakatsuji, N.; Suemori, H. Endodermal Differentiation of Human Pluripotent Stem Cells to Insulin-Producing Cells in 3D Culture. *Sci. Rep.* **2014**, *4*, 1–9. https://doi.org/10.1038/srep04488.

(168) Dewey Jr., C. F.; Bussolari, S. R.; Gimbrone Jr., M. A.; Davies, P. F. The Dynamic Response of Vascular Endothelial Cells to Fluid Shear Stress. *J. Biomech. Eng.* **1981**, *103* (3), 177–185. https://doi.org/10.1115/1.3138276.

(169) Li, Y.-S. J.; Haga, J. H.; Chien, S. Molecular Basis of the Effects of Shear Stress on Vascular Endothelial Cells. *J. Biomech.* **2005**, *38* (10), 1949–1971. https://doi.org/https://doi.org/10.1016/j.jbiomech.2004.09.030.

(170) Huse, M. Mechanical Forces in the Immune System. *Nat. Rev. Immunol.* **2017**, *17* (11), 679–690. https://doi.org/10.1038/nri.2017.74.

(171) Hunter, M. C.; Teijeira, A.; Halin, C. T Cell Trafficking through Lymphatic Vessels. *Front. Immunol.* **2016**, *7* (DEC). https://doi.org/10.3389/fimmu.2016.00613.

(172) Junttila, M. R.; De Sauvage, F. J. Influence of Tumour Micro-Environment Heterogeneity on Therapeutic Response. *Nature* **2013**, *501* (7467), 346–354. https://doi.org/10.1038/nature12626.

(173) Runa, F.; Hamalian, S.; Meade, K.; Shisgal, P.; Gray, P. C.; Kelber, J. A. Tumor Microenvironment Heterogeneity: Challenges and Opportunities. *Curr. Mol. Biol. reports* **2017**, *3* (4), 218–229. https://doi.org/10.1007/s40610-017-0073-7.

(174) Yuan, Y. Spatial Heterogeneity in the Tumor Microenvironment. *Cold Spring Harb. Perspect. Med.* **2016**, *6* (8). https://doi.org/10.1101/cshperspect.a026583.

(175) García-Jiménez, C.; Goding, C. R. Starvation and Pseudo-Starvation as Drivers of Cancer Metastasis through Translation Reprogramming. *Cell Metab.* **2019**, *29* (2), 254–267. https://doi.org/10.1016/j.cmet.2018.11.018.

(176) DeBerardinis, R. J.; Chandel, N. S. Fundamentals of Cancer Metabolism. *Sci. Adv.* **2016**, *2* (5), e1600200–e1600200. https://doi.org/10.1126/sciadv.1600200.

(177) Gouirand, V.; Guillaumond, F.; Vasseur, S. Influence of the Tumor Microenvironment on Cancer Cells Metabolic Reprogramming. *Front. Oncol.* **2018**, *8* (APR), 1–6. https://doi.org/10.3389/fonc.2018.00117.

(178) Romero-Garcia, S.; Moreno-Altamirano, M. M. B.; Prado-Garcia, H.; Sánchez-García, F. J. Lactate Contribution to the Tumor Microenvironment: Mechanisms, Effects on Immune Cells and Therapeutic Relevance. *Front. Immunol.* **2016**, *7* (FEB). https://doi.org/10.3389/fimmu.2016.00052.

(179) Hirschhaeuser, F.; Sattler, U. G. A.; Mueller-Klieser, W. Lactate: A Metabolic Key Player in Cancer. *Cancer Res.* **2011**, *71* (22), 6921–6925. https://doi.org/10.1158/0008-5472.CAN-11-1457.

(180) Zhang, X.; de Milito, A.; Olofsson, M. H.; Gullbo, J.; D'Arcy, P.; Linder, S. Targeting Mitochondrial Function to Treat Quiescent Tumor Cells in Solid Tumors. *Int. J. Mol. Sci.* **2015**, *16* (11), 27313–27326. https://doi.org/10.3390/ijms161126020.

(181) Goldsmith, J.; Levine, B.; Debnath, J. Chapter Two - Autophagy and Cancer Metabolism. In *Conceptual Background and Bioenergetic/Mitochondrial Aspects of Oncometabolism*; Galluzzi, L., Kroemer, G. B. T.-M. in E., Eds.; Academic Press, 2014; Vol. 542, pp 25–57. https://doi.org/https://doi.org/10.1016/B978-0-12-416618-9.00002-9.

(182) Nunes, A. S.; Barros, A. S.; Costa, E. C.; Moreira, A. F.; Correia, I. J. 3D Tumor Spheroids as in Vitro Models to Mimic in Vivo Human Solid Tumors Resistance to Therapeutic Drugs. *Biotechnol. Bioeng.* **2019**, *116* (1), 206–226. https://doi.org/10.1002/bit.26845.

(183) Sun, L.; Suo, C.; Li, S.; Zhang, H.; Gao, P. Metabolic Reprogramming for Cancer Cells and Their Microenvironment: Beyond the Warburg Effect. *Biochim. Biophys. Acta - Rev. Cancer* **2018**, *1870* (1), 51–66. https://doi.org/https://doi.org/10.1016/j.bbcan.2018.06.005.

(184) Robertson-Tessi, M.; Gillies, R. J.; Gatenby, R. A.; Anderson, A. R. A. Impact of Metabolic

Heterogeneity on Tumor Growth, Invasion, and Treatment Outcomes. *Cancer Res.* **2015**, *75* (8), 1567–1579. https://doi.org/10.1158/0008-5472.CAN-14-1428.

(185) Gentric, G.; Mieulet, V.; Mechta-Grigoriou, F. Heterogeneity in Cancer Metabolism: New Concepts in an Old Field. *Antioxid. Redox Signal.* **2016**, *26* (9), 462–485. https://doi.org/10.1089/ars.2016.6750.

(186) Lamb, R.; Ozsvari, B.; Bonuccelli, G.; Smith, D. L.; Pestell, R. G.; Martinez-Outschoorn, U. E.; Clarke, R. B.; Sotgia, F.; Lisanti, M. P. Dissecting Tumor Metabolic Heterogeneity: Telomerase and Large Cell Size Metabolically Define a Sub-Population of Stem-like, Mitochondrial-Rich, Cancer Cells. *Oncotarget* **2015**, *6* (26), 21892–21905. https://doi.org/10.18632/oncotarget.5260.

(187) Nakajima, E. C.; Laymon, C.; Oborski, M.; Hou, W.; Wang, L.; Grandis, J. R.; Ferris, R. L.; Mountz, J. M.; Van Houten, B. Quantifying Metabolic Heterogeneity in Head and Neck Tumors in Real Time: 2-DG Uptake Is Highest in Hypoxic Tumor Regions. *PLoS One* **2014**, *9* (8), e102452.

(188) Shiao, S. L.; Ganesan, A. P.; Rugo, H. S.; Coussens, L. M. Immune Microenvironments in Solid Tumors: New Targets for Therapy. *Genes Dev.* **2011**, *25* (24), 2559–2572. https://doi.org/10.1101/gad.169029.111.

(189) Gonzalez, H.; Hagerling, C.; Werb, Z. Roles of the Immune System in Cancer: From Tumor Initiation to Metastatic Progression. *Genes Dev.* **2018**, *32* (19–20), 1267–1284. https://doi.org/10.1101/gad.314617.118.

(190) Terrén, I.; Orrantia, A.; Vitallé, J.; Zenarruzabeitia, O.; Borrego, F. NK Cell Metabolism and Tumor Microenvironment. *Front. Immunol.* **2019**, *10*, 2278. https://doi.org/10.3389/fimmu.2019.02278.

(191) Larsen, S. K.; Gao, Y.; Basse, P. H. NK Cells in the Tumor Microenvironment. *Crit. Rev. Oncog.* **2014**, *19* (1–2), 91–105. https://doi.org/10.1615/critrevoncog.2014011142.

(192) Poggi, A.; Zocchi, M. R. Mechanisms of Tumor Escape: Role of Tumor Microenvironment in Inducing Apoptosis of Cytolytic Effector Cells. *Arch. Immunol. Ther. Exp. (Warsz).* **2006**, *54* (5), 323–333. https://doi.org/10.1007/s00005-006-0038-7.